The Pennsylvania State University

The Graduate School

Department of Biomedical Engineering

CHARACTERIZATION OF EARLY MEMBRANE ADHESION ACTIVITY WITH A DRIFT-CORRECTED OPTICAL TRAP

A Thesis in

Bioengineering

by

George J. Moroney

Submitted in Partial Fulfillment

of the Requirements

for the Degree of

Master of Science

May 2015

The thesis of George J. Moroney was reviewed and approved* by the following:

Peter J. Butler
Professor of Bioengineering
Thesis Advisor

William O. Hancock
Professor of Bioengineering
Head of Bioengineering Graduate Program

Keefe B. Manning
Associate Professor of Bioengineering

*Signatures are on file in the Graduate School

ABSTRACT

Vascular endothelial cells have been shown to sense the pressure and shear stress imparted by blood flow and to convert these mechanical stimuli into intracellular and extracellular chemical products such as prostacyclin and nitric oxide. Such products alter cardiovascular function by their ability to adjust vascular dilation and inhibit platelet aggregation and clotting. A leading hypothesis for mechanotransduction suggests that forces alter the interaction of integrin-based adhesions to extracellular matrix molecules. Such interactions are expected to be on the time scale of cardiac pulsatility (1-2 Hz). Thus, a greater understanding of the precise magnitude and temporal characteristics of cell adhesion would be instrumental in understanding the fundamental mechanisms of mechanotransduction. Whereas the cell interacts with its environment via the assembly of membrane proteins to form focal adhesions, studies on the early dynamics of force production by optical trapping would lead to a fundamental understanding of mechanotransduction by vascular endothelium. This thesis describes the development, testing, and optimization of protocols and instrumentation for the characterization of integrin-based adhesion to extracellular matrix proteins.

Optical trapping allows for application of forces to single molecules and molecular clusters of similar magnitude (~2 pN) to the external forces that these molecules experience *in vivo.* More importantly for this study, the optical trap is able to detect the exact time that a force is applied to the cell. In order to monitor the activity of adhesion events, a continuous focus drift mechanism with a 100 nanometer-scale sensitivity was developed. This technique measures the changes in distance between the objective and cover slip by measuring the intensity of the light from the epi pathway of the microscope that reflects off of the cover slip.

The early adhesion dynamics of the cells were studies using both a variance-based and time-to-adhesion-based assay using fibronectin-functionalized beads in contact with the membrane of human aortic endothelial cells. Preliminary results suggest that decreasing membrane fluidity with benzyl alcohol decreases time to adhesion, suggesting that a principle mechanism of force transduction depends on lateral transport of integrins to the adhesion site.

TABLE OF CONTENTS

LIST OF FIGURES

LIST OF TABLES

ACKNOWLEDGEMENTS

I would like to extend thanks to my advisor, Peter Butler, for his guidance and support throughout my time at Penn State. From serving as my Honors Advisor as an undergraduate to mentoring me as my PI as a graduate student, Dr. Butler has been a huge factor in furthering my bioengineering education over the past few years. His integrity and dedication both as a researcher and a person have taught me to never be satisfied with “just good enough.” I would also like to thank my lab mate, Seoyoung Son, for helping me out incredibly with bead functionalization and cell culture protocols, in addition to being a great friend and colleague. I would like to thank my committee members, Dr. Peter Butler, Dr. William Hancock, and Dr. Keefe Manning, for taking the time to review and critique my work. Finally, I would like to thank the entire staff of the Biomedical Engineering Department, especially Carol, Doretta, Gene, and Gary, for their support and generosity.

This thesis is dedicated to my sister Sheila, who always cheers me up with corny jokes, who never misses an opportunity to make fun of me for “calibrating my laser,” and who will definitely think it’s weird that I’m dedicating my thesis to her.

Chapter 1

INTRODUCTION

1.1 Endothelium

Endothelial cells form tight and gap junctions with each other to form the endothelium, which lines the inside of blood vessels and is known to induce vasodilation and release anticoagulants in response to hemodynamic forces [1]. Thus the endothelium, in addition to acting as a semi-permeable barrier for blood, regulates the delivery of blood to the tissues. On a subcellular level, endothelial cells interact with the extracellular matrix on their abluminal side via integrin-based complexes termed focal adhesions. It is believed that dynamic interaction of integrins with specific extracellular matrix proteins is responsible for endothelial cell sensitivity to fluid forces. Shear forces have been applied to the surface of endothelial cells, triggering chemical pathways that are dependent upon the specific interactions between membrane integrins and extracellular matrix proteins such as fibronectin, vitronectin, collagen I, laminan, and fibrinogen [2]. Additionally, it has been shown that upon activation, transmembrane integrins produced prostaglandin, which is known to cause vasodilation [3]. Thus, shear-induced changes in integrin interaction with extracellular matrix proteins are at the heart of endothelial cell sensing. Reacting to these changes in shear forces in the cardiovascular system is an essential process for cardiovascular health.

1.2 Mechanotransduction

Mechanotransduction is the process by which forces are converted to biological signals. The three important ingredients of this process are the magnitude and temporal characteristics of force application, the mechanical properties of the cells and molecular constituents that transduce force, and the biomolecular signaling cascades the lead to the observed phenotypic modulation, such as changes in nitric oxide or prostacyclin. While the overall mechanical strength of a cell is largely regulated by its cytoskeleton, it is now recognized that the dynamic clustering of membrane-bound molecules such as integrins can influence signaling. Such clustering is regulated by the membrane viscosity, and its natural bending fluctuations. Thus, membrane molecular dynamics and mechanics are as important to mechanotransduction research as cytoskeleton-regulated cellular mechanics.

Mechanical studies of the membrane provides insight to what types of forces are exerted on the cell and what types of forces a cell exerts on its surroundings, often keyed by the transient dynamics of plasma membrane "molecular switches" such as Ras proteins [4]. Mechanotransduction is defined as a cellular response to a mechanical stimulus. It has been shown that mechanical force can be enough to induce a focal adhesion on the cell membrane. Mechanotransduction is utilized in many parts of the body, from detecting deformations in hair cells to facilitate hearing and balance [5], to measuring shear stress from blood flow on endothelial cells [6]. It has been traditionally believed that mechanotransduction pathways in endothelial cells are separate from other signal transduction pathways. However, mechanotransduction pathways can in fact combine with traditional ligand/receptor pathways to more rapidly initiate nuclear signaling than do diffusion mediated signaling pathways [7], [8].

1.3 Focal Adhesions

Focal adhesions bind to extracellular matrix proteins and directly trigger downstream signal transduction pathways. The initiation of a focal adhesion is one of the first steps of mechanotransduction. Focal adhesions are large collections of transmembrane and structural proteins that connect the extracellular matrix to the cytoskeleton. Transmembrane and intracellular proteins regulate the mechanics and the dynamics of these focal adhesion contact points. The binding of integrins with extracellular matrix proteins causes a downstream response, with the intracellular protein talin binding to the subcellular portion of the integrin [9]. These integrin-talin complexes phosphorylate focal adhesion kinase (FAK) and adhere to the actin cytoskeleton of the cell.

Within a focal adhesion, represented in Figure 1, specific integrins are immobilized by cytoskeletal proteins, and inside-out signaling from actin to fibronectin occurs only through specific integrins. For example, in a focal adhesion, β_3 integrins are immobilized, enriched and stationary, while β_1 are not as enriched [10]. There are many proteins that work to disrupt the actin-integrin-fibronectin complex, but once it has been formed the integrin is immobilized [10]. Though the integrin is immobilized, it is constantly switching back and forth between active and inactive states within a focal adhesion [11]. It has also been shown that the dynamic interaction between integrins and extracellular matrix ligands is critical in relaying signals caused by shear stress in intracellular mechanotransduction pathways [12].

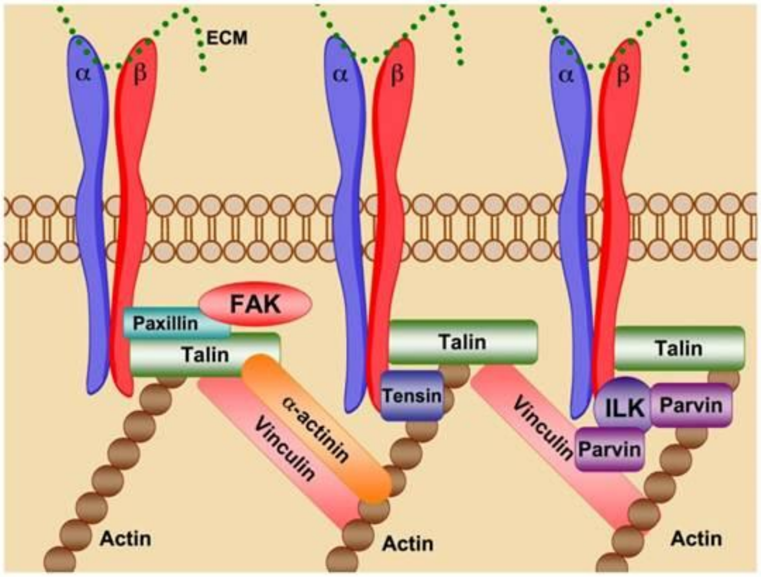

Figure 1: Composition of transmembrane integrins. The extracellular tails bind directly to ECM molecules while the cytoplasmic tail is connected to the actin cytoskeleton by a number of intracellular proteins and kinases. [13]

While focal adhesions have been characterized in detail, less is known about nascent focal adhesions and focal adhesion induction. When a substrate comes into contact with a cell membrane, the dynamics of focal adhesion formation relies first on integrin diffusion through the membrane. Certain proteins such as vinculin and FAK have been found to anchor integrins to the cytoskeleton, immobilizing individual proteins without affecting the overall diffusion properties of integrin in a lipid membrane [14]. The study described in this thesis involves the effect of membrane viscosity and mechanics on the mobility of integrins and the subsequent induction of focal adhesions.

1.4 Membrane Properties

Several membrane properties are vital to focal adhesion formation. First, a focal adhesion requires membrane curvature. Integrins have been found to undergo conformational changes when activated. At a focal adhesion, integrins will elongate, causing membrane bending [15]. Second, the integrins must diffuse through the membrane to the substrate location, where the focal adhesion will form. Lipid bilayers are in fact very fluid and proteins diffuse laterally across a membrane via Brownian motion [16].

Both the head group and the tail group chemistry of the cell membrane lipids affect the membrane fluidity. Hydrogen bonding in the lipid heads, Van Der Waals forces in the tail domains, and height of the lipid can all cause a decrease in the diffusion coefficient through decreased molecular motion [17]. Integrins typically undergo fast free diffusion in a normal cell membrane. However, as they move closer to a focal adhesion it has been observed that the diffusion mechanism switches to slow diffusion [11]. Additionally, compounds such as cholesterol, benzyl alcohol, and vitamin E have been shown to affect both membrane rigidity [18] and diffusion of transmembrane proteins throughout the membrane [19].

1.5 Integrin Affinity and Avidity

Integrins are key factors in focal adhesion formation due to the fact that they are intrinsically dynamic. Interactions between integrins and extracellular matrix proteins are extremely variable; integrin bonds have been shown to bind strongly and resiliently to extracellular matrix (ECM) proteins in stretching tissue or immune cells [20] but in spreading endothelial cells, integrins rapidly bind to and dissociate from ECM proteins, creating a series of weak, transient binding forces [21]. In these cases of fast focal adhesion formation, the avidity of the integrin-fibronectin (an ECM protein) bonds depend greatly on the recruitment of integrins throughout the membrane to the site of adhesion and the affinity of integrins to those ECM proteins. The affinity of an integrin to bind to fibronectin can depend on a number of factors, such as force applied, cation concentrations [22], and availability of ligands [23].

1.6 Force Spectroscopy

There are many force spectroscopy techniques used to study mechanotransduction or single molecule forces. Atomic force microscopy (AFM) [24]–[26], magnetic tweezers [27], and microneedle nanoelectrodes [28] have all been effective methods for understanding how cells sense force and how they react to these forces. For this experiment, a simple, repeatable method was needed. In addition, the tool used to induce a focal adhesion needed to be the same size as a focal adhesion, while exerting a physiologically relevant force. In this case, an optical trap was used.

1.7 Optical Trap

Optical trapping is a technique that allows for precise and repeatable measurements on cells and small molecules. This technology uses the momentum of laser light to trap a small bead in the x, y, and z directions. Since the laser is Gaussian in strength, the highest momentum is applied at the center of the laser beam, as shown in Figure 2. Therefore, when a bead is moved out of the center, a resulting restoring force pulls the bead back towards the center. Similarly, forces in the z-direction work to trap the bead just above the focal point of the laser. The equilibrium point for the bead rests above the actual focal point of the laser due to the scattering forces created by the reflection of light off of the surface of the bead. This reflected light causes a resultant force in the direction of propagation, similar to the process of spraying a beach ball with a hose.

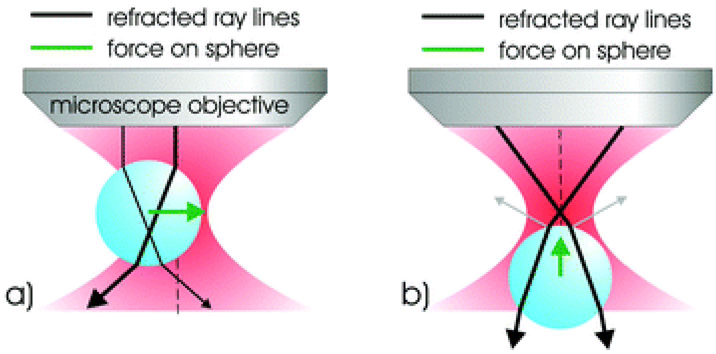

Figure 2: Schematic of an optical trap. The bead is trapped in the a) the x- and y-direction, as well as b) in the z-direction. [29]

Optical traps (also called optical tweezers) are able to generate pN-scale forces, making them ideal for studying cell membrane mechanical properties. Previously, an optical trap has been used to study binding properties of integrin with cytoskeletal actin filaments. It was found that areas rich in actin required much more force to deform than areas of depleted actin, which proves the importance of the cytoskeleton as the cell's mechanical backbone [30].

An optical trap is used to create a shear force tangent to the cell membrane. The trapped bead, which is functionalized with an extracellular matrix protein such as fibronectin, acts as a stress generator when it binds to the integrins. This stress transduction is proven by the accumulation of cytoskeletal talin proteins in the area of shear stress and focal adhesion [31].

1.8 Optical Trap Calibration/Measurement Techniques

This optical trap setup uses a single laser beam and a quadrant photodiode to detect the exact displacement of a bead. Like a spring, a laser has a spring constant that characterizes the trapping force on a bead.

Various methods have been used to calibrate an optical trap setup in order to find the spring constant of the laser. First, the equipartition theorem quantifies the thermal motion of the bead in order to measure the stiffness of a trap. The average kinetic energy, $\langle H \rangle$ of a particle undergoing random Brownian motion is given as

$$\langle H \rangle = \frac{1}{2} k_B T \tag{1-1}$$

where k_B is Boltzmann's constant and T is the temperature in Kelvin [32]. Assuming that the only motion of the trapped bead is due to thermal motion, the potential energy of the optical trap can be equated to the kinetic energy of the bead, given as

$$E = \frac{1}{2} k \langle x^2 \rangle$$

(1-2)

where $\langle x^2 \rangle$ is the time-averaged square of the bead displacement and k is the spring constant of the trap. Therefore, the spring constant of the optical trap can be calculated, given in Equation 1-3.

$$k = \frac{k_B T}{\langle x^2 \rangle}$$

(1-3)

Another method that employs the Brownian motion of the bead to calculate the spring constant of the optical trap is the power spectrum method. The power spectrum of an optically trapped particle can be described as the Fourier transform of the Brownian motion of the bead [33], described by the Lorentzian in Equation 1-4

$$S(f) = \frac{k_B T}{2\gamma\pi^2 (f_c^2 + f^2)}$$

(1-4)

where γ is the drag coefficient, f is the sampling frequency, and f_c is the corner frequency fit to the curve, defined as the frequency at which the energy of the system begins to attenuate. By fitting a corner frequency, the spring constant can be calculated through the relation described in Equation 1-5.

$$k = 2\pi\, \gamma f_c$$

(1-5)

Although this method has proven to be precise and accurate [34], the method requires a laser of higher power than the laser used in the variance-based bead-cell assay in this thesis.

The method of calibration in this study was the drag force method, which involved a sinusoidal motion that was applied to a trapped bead. Using a modified version of Stokes Law detailed in Equation 1-6 to account for distance from the coverslip, a relationship is developed between voltage recorded by the photodiode and force applied. Then, the spring constant can be calculated with known distance. This force is defined as

$$F = \frac{6\pi\mu r v}{1 - \frac{9}{16}\left(\frac{r}{h}\right) + \frac{1}{8}\left(\frac{r}{h}\right)^3 - \frac{45}{256}\left(\frac{r}{h}\right)^4 - \frac{1}{16}\left(\frac{r}{h}\right)^5} \tag{1-6}$$

where r is the radius of the bead, v is the velocity of the bead, μ is the viscosity of the liquid, and h is the distance from the cover slip.

With a known optical trap spring constant, experimental forces can be calculated using distance measurements. Optical traps are able to exert forces on the scale of pN, which are physiologically significant [6]: molecular motors, hydrogen bonds, and covalent bonds have been found to be on the order of pN.

1.9 Microscope Focus Drift

In many instances of differential interference microscopy, the microscope is sharply focused in order to precisely measure the nanoscale phenomenon being studied. While advanced microscopes are able to effectively create these images, the quality of such highly magnified images are sensitive to slight changes in focus. Focus drift is the inability of the microscope to sustain the desired focal plane, which results in the deterioration of the focused image over time [27]. In cases where the process being studied exists on the timescale of minutes, hours or days, focus drift can be a significant problem. Focus drift can especially become a problem when using an objective with high magnification and high numerical aperture, which causes the axial focus depth to be extremely narrow. These issues can exist for a variety of reasons. First, focus drift could be caused by mechanical instability. With objectives loaded, the nosepiece of a microscope can weigh up to 5 pounds, which applies a strain on the focus knob mechanism [36]. If the gravitational force that causes this strain is greater than the maximum force capability of the focus mechanism, the nosepiece can physically lower over time, causing focus drift [37]. Additionally, the immersion media can play a role in focus drift. High numerical apertures are often used under oil or water immersion, but over time the chemical breakdown and viscosity changes of the oil can affect the focal plane, and water evaporates.

Finally, the most common source of focus drift is a change in temperature, or thermal drift. In experiments involving live cells, it has been shown that cells survive best at 37 °C. Objective heaters or culture dish heaters can be used to maintain that temperature, but if the temperature is not steady, fluctuations in temperature can cause fluctuations in shape of the glass slide [38]. This effectively changes the distance between the front lens of the objective and the cover slip, which causes a loss of focus. Temperature changes can also affect the viscosity and refractive index of the immersion media, causing the effects detailed earlier.

1.10 Drift Correction Methods

A number of solutions have been found to compensate and correct for focus drift. These drift correction approaches are not to be confused with automated microscopy or autofocus techniques – drift correction algorithms do not use image stacks to initially find the plane of optimal focus. Instead, drift correction methods aim to lock the microscope in a predetermined focal plane. Control of focus drift requires hardware to control spacing between the objective and cover slip: either a motorized stage or objective [39]. Many strategies have been employed to dynamically correct for focus drift, but most fit into two categories: hardware structures and software algorithms. Most hardware solutions employ light emitting diode (LED) light to measure the distance between the cover slip and the front focal plane of the objective. In these techniques, a near-infrared LED is reflected off of the upper edge of the cover slip (the edge that is in contact with the media solution), as shown in Figure 3. The reflected beam is then projected onto a photodiode, which transduces the light signal into a voltage that can be read by a data acquisition device. This signal is then processed by a computer that in turn compensates for an error by moving either the stage or objective. These systems have been able to achieve focal precisions of up to 1/3 of the focal depth of the objective [40].

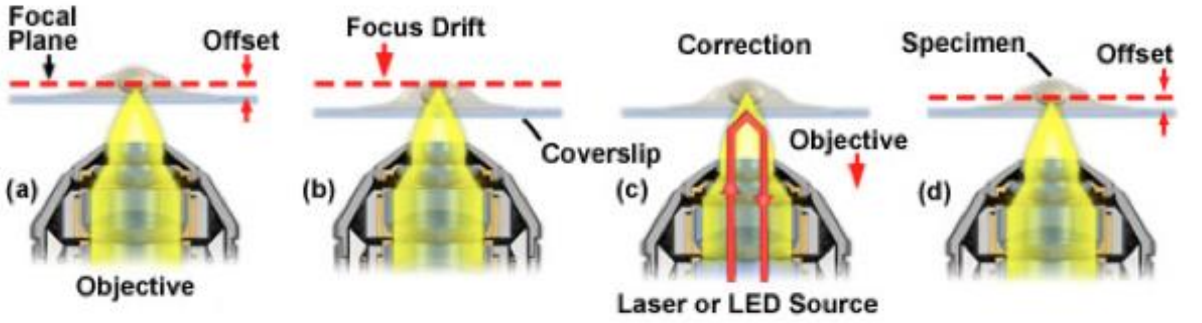

Figure 3: The focal plane is established by the user and the initial offset between the focal plane and coverslip is defined (3a). When focus drift occurs (3b), the LED signal changes (3c) and allows the system to return the microscope to original offset (3d) [41]**.**

Software-based approaches are often focused on imaging, but require some additional components. The microscope must be capable of differential interference contrast (DIC) and a digital camera is needed [39]. In these techniques, still images are continuously captured and analyzed in order to detect and compensate for focus drift, as shown in Figure 4. One method, which detects sharpness of edges of objects in the image, operates under the assumption that in-focus images will have better contrast and sharper edges than images that are out of focus [42].

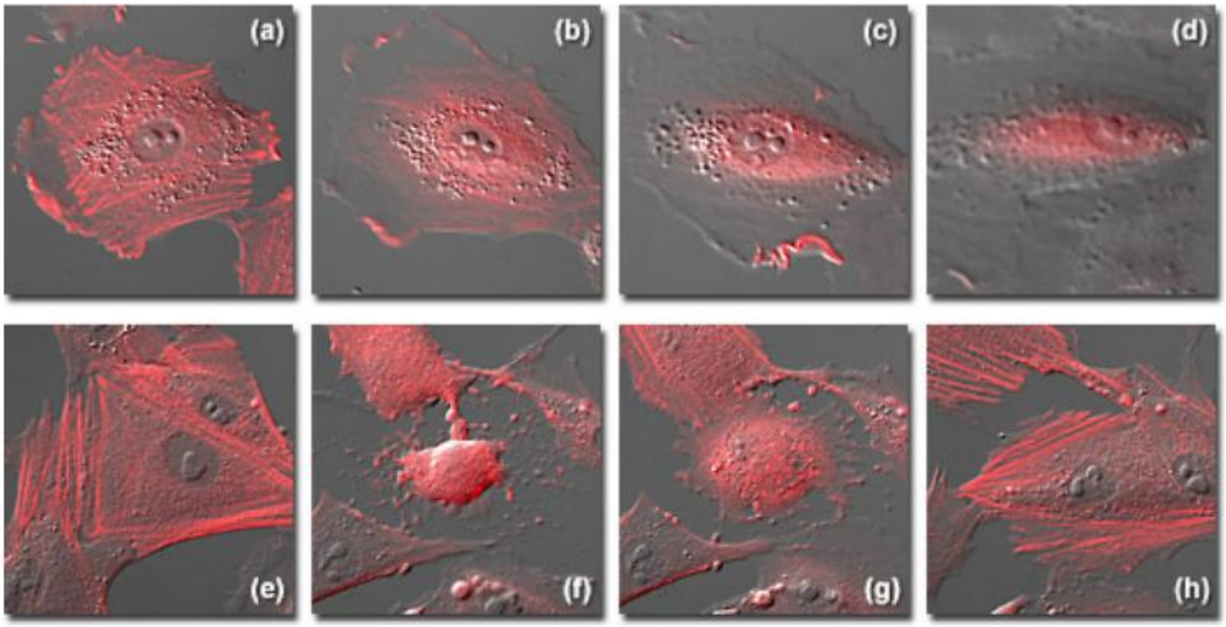

Figure 4: Figures 4 (a-d) depict a live-cell sample that is subject to focus drift over time. 4 (e-h) show a sample where the focus drift is automatically compensated [37].

DIC imaging is especially important in this case because of its ability to establish contrast without the need for any fluorescence [43]. The accuracy of this approach increases by decreasing the region of interest (ROI), but at the expense of precision due to lower pixel numbers. Using the Laplace operator, the software algorithm takes the derivative of the intensity values of adjacent pixels throughout the image and creates a contrast "score" [44]. When the image is in focus, edges are sharp and a high derivative value is indicative of an edge. However, when the image is out of focus, the well-defined edges become blurred and the derivative values decrease. Based on the set point score value defined by the user, this technique can detect moderate focus drift. This approach relies heavily on the memory and processing speed of the computer, as analyzing each image can take a significant amount of time. Other methods of image analysis have also been employed, such as analysis of standard deviation, total pixel intensity, and histogram analysis of pixel intensity [45]. After the loss of focus has been detected, both hardware and software-based compensation algorithms use various feedback loops to restore the microscope to its ideal focus.

1.11 PID Controllers

PID (proportional, integral, derivative) controllers are advanced feedback loop algorithms that utilize proportional, integral, and derivative components in order to keep a process variable at a given set point. The system analyzes the incoming signal by comparing the error between the current state of the process variable and the set point and is visualized in Figure 5. The error of this state is then used to calculate a manipulated variable, which is shown in Equation 1-7 and is composed of the proportional, integral, and derivative gains. The values of the gains help to determine the sensitivity and speed of the control system. One common method for determining the value of these gains is the Ziegler-Nichols method, in which an ultimate gain is found experimentally as the gain at with the system oscillates at a continual value. The values for proportional, integral, and derivative gains are then calculated from this ultimate gain [46].

$$\mathrm{u}(t) = \mathrm{MV}(t) = K_p e(t) + K_i \int_0^t e(\tau)\, d\tau + K_d \frac{d}{dt} e(t) \tag{1-7}$$

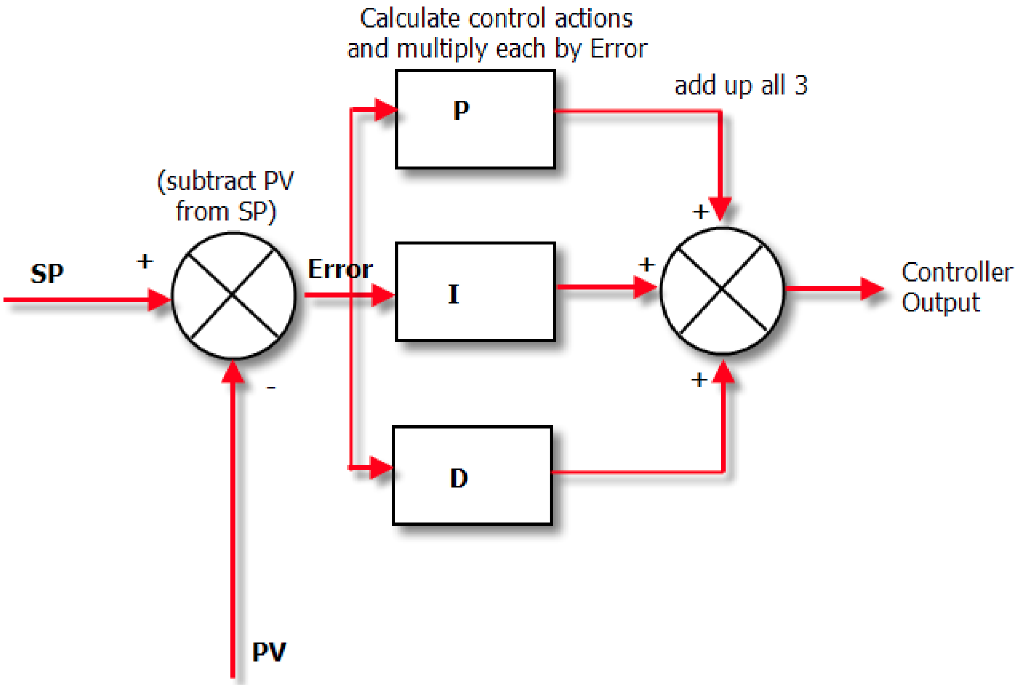

Figure 5: Standard PID control loop. [47]

In the methods and materials section, this thesis will present the optical trap calibration method, drift correction algorithm, and cell culture protocols. In addition, this section will provide the experimental details for both the variance-based and the escape force-based bead-cell adhesion assays. The results section will then present the verification of focus drift correction, as well as results from the both the variance-based and adhesion force-based bead-cell adhesion assay. In the discussion section, I will go explain the biological phenomena theorized to cause the observed results and frame the escape force-based assay with a computational study. Finally, in the conclusion I will outline some future experimental paths that could be pursued.

Chapter 2

METHODS AND MATERIALS

2.1 COMSOL Model

To develop a better understanding of the physics of the specific optical trap used in these experiments, a finite element analysis model was developed using the exact parameters found in the physical experiments. The goal of this model was to computationally derive the stiffness of the trap and the forces applied to the bead. A 2-D computational model of the optical trap was created using the Electromagnetic Waves, Frequency Domain module of COMSOL Multiphysics. The model created simulates the 830 nm, 5 mW fiber coupled laser used in optical trapping experiments. The laser light focuses on the subject through a highly focused 60X oil immersion objective with NA = 1.45. The electromagnetic waves module was used to generate a 2-dimensional background electric field focused on a 2 μm polystyrene bead submerged in water. The equation used to characterize the 2D Gaussian beam was

$$E(x,y) = E_0 \frac{w_0}{w(y)} e^{-\frac{x^2}{w(y)^2}} e^{\frac{ikx^2}{2R(y)}} e^{iky} e^{-\frac{1}{2} i tan^{-1}(\frac{y}{z_0})} \tag{2-1}$$

where E_0 is electric field at the origin, w_0 is the beam waist, z_0 is the Rayleigh range, k is the propagation constant,

$$w(y) = w_0 \sqrt{1 + \left(\frac{y}{z_0}\right)^2}$$

(2-2)

and

$$R(y) = y\left(1 + \left(\frac{z_0}{y}\right)^2\right)$$

(2-3)

where the beam waist, defined as the narrowest width of the beam, is calculated as $w_0=2\lambda/NA$ = 1036 nm [48]. Here, E_0 is defined as the magnitude of the electric field at the focus of the laser. This value is calculated as

$$E_0 = \sqrt{\frac{4P}{cn\pi\varepsilon_0 {w_0}^2}}$$

(2-4)

Where c is the speed of light, ε_0 is the vacuum permittivity, and P is the power of the laser, 50 mW in this case. The propagation constant k is calculated by $k=2\pi/\lambda$. The Rayleigh range, z_0, is defined as the distance from the beam waist where the distance from the beam $z_0= w_0/NA$.

The geometry used in the models was a rectangle of width 20 µm and height 40 µm with a 5 µm-thick perfectly matched layer surrounding the exterior. The rectangle was given the material properties of water (refractive index n=1.33). A 2 µm circle was fixed at the center of the rectangle to simulate the bead and given the material properties of polysilicon (n=1.6).

The study was conducted using an extremely fine mesh with maximum element size of 100 nm, maximum growth rate 1.3 and curvature factor 0.3 in the frequency domain. A parametric sweep was conducted for x component of the bead position. The position of the bead was varied from -2500 nm to 2500 nm at intervals of 250 nm. Variations of the 2-dimensional heat map plot for the electric field strength at each position can be found in Appendix A.

In postprocessing, the gradient force caused by the refraction of light was calculated across the arc length of the bead using the equation

$$F_g = -\pi {n_m}^2 \varepsilon_0 r^3 \left(\frac{m^2 - 1}{m^2 + 2}\right) \nabla E^2 \tag{2-5}$$

where $m=n_m/n_p$ and n_m is the refractive index of the medium while n_p is the refractive index of the bead. The radius of the bead, r, was 1 μm.

In order to calculate the total force acting on the bead in the x-direction, a line integration was performed over the circumference of the bead. This resulted in a total gradient force for each of the positions accounted for in the parametric sweep. This calculated gradient force was then plotted versus position of the bead relative to the trap. Because an optical trap acts as a spring, the linear relationship between bead position and gradient force in the center of the trap can be defined as the trap stiffness, or spring constant, in pN/μm, as shown in Figure 6.

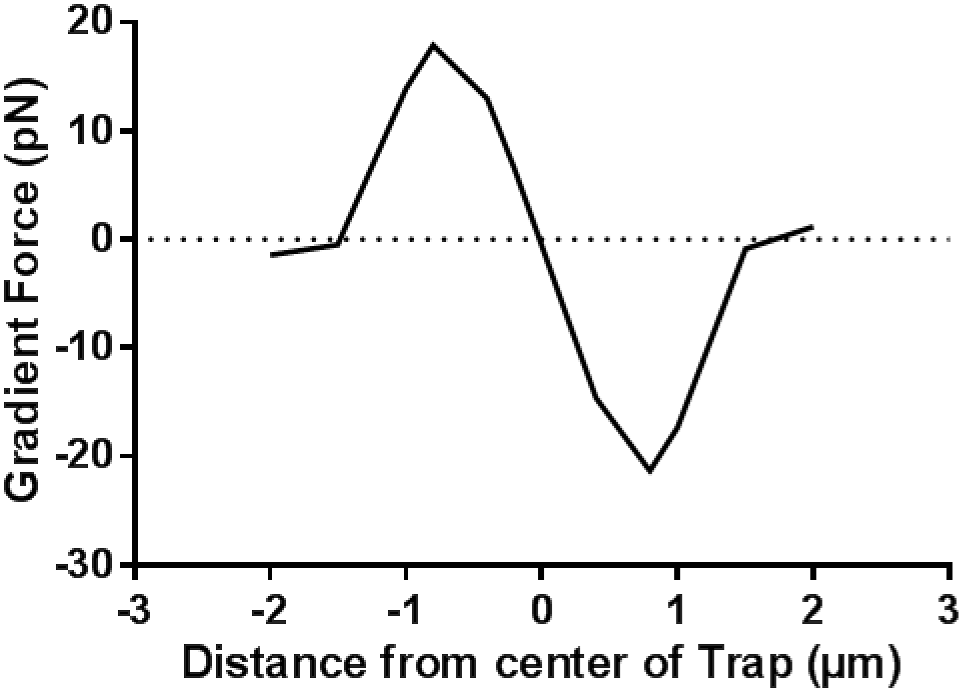

Figure 6: Gradient forces at each bead position were calculated. Bead position was defined in relation to the center of the trap.

2.2 Optical Trap Set Up

All optical trapping experiments were conducted on an inverted Olympus IX71 epifluorescence microscope mounted on a Newport 3’x5’ vibration isolation workstation equipped with high speed, low light Cooke Sensicam CCD camera and Mad City Labs Nanodrive piezoelectric computer controlled stage [49]. An Olympus 60x 1.45 NA objective was used in all trapping experiments in order to optimize the axial trap strength.

For calibration experiments, bead solutions were prepared in flow chambers made following an established standard operating procedure (SOP) in the Mechanobiology Lab. The beads used in calibration were 2 μm polystyrene beads diluted 1:1000 in double distilled water. A Corning 75 mm x 25 mm glass slide and a VWR 18 mm x 18 mm glass coverslip were washed with ethanol to avoid bead adhesion to the glass. Then, two strips of 3M double-sided tape were applied to the cover slip approximately 8 mm apart. The coverslip was placed on top of the strips of tape and excess tape was cut away with a razor. The 50 μL of 1:1000 bead solution was pipetted between the glass and coverslip and a tissue wipe was used to draw the fluid evenly throughout the chamber. Finally, the openings of the chamber was sealed with clear nail polish and allowed to dry. This SOP essentially creates a flow chamber with dimensions of 8 mm x 18 mm x 0.07 mm (thickness of double sided tape [50]).

The inverted microscope detailed in Figure 7 is then set up for differential interference contrast (DIC) microscopy in order to image the beads without the need for fluorescent beads. The laser used for optical trapping was either a Qioptiq 850 nm 50 mW or a QPhotonics 1064 nm with variable power fiber-coupled laser diode. Once the beads were visible using DIC, they were trapped by manually moving the stage in the x- and y-directions until a bead was trapped in the focal point of the optical tweezers. Once the bead was trapped, calibration experiments could be performed.

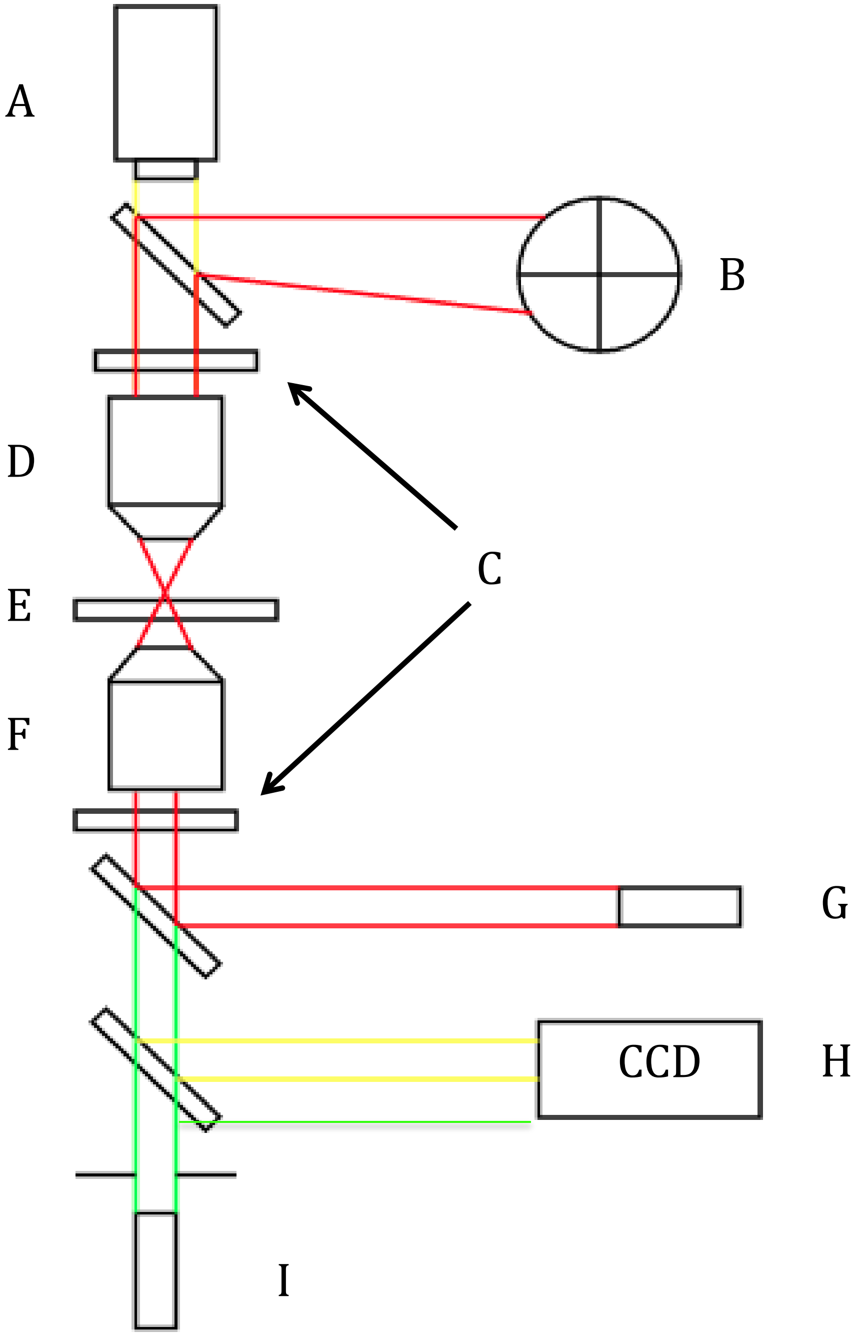

Figure 7: Microscope setup for the optical trap on an inverted Olympus IX71 microscope. A 100 W halogen lamp (7A) provided brightfield illumination. The microscope is set up using DIC imaging, which uses the Wollaston prisms (7C) to separate and integrate orthogonalities of light, creating a high-contrast picture imaged by the 12-bit CCD camera (7H). The laser source (7G) is an 850 nm mW fiber coupled Qioptiq laser diode model iFLEX-1000 in some experiments, and a QPhotonics 1064 nm fiber laser coupled diode with variable power settings in other experiments. Laser light is projected onto the Quadrant Photodiode (7B) to track the position of a trapped bead. The light was focused with a 60X 1.45 NA oil immersion objective (7F) and a 0.9 NA oil immersion condenser (7D). Another 75 W halogen lamp (7I) illuminates the epi pathway through a field-stop diaphragm, which reflects off of the temperature-controlled cell culture dish (7E) and collected by the CCD camera for focus drift correction.

2.3 Optical Trap Calibration

An optical trap can hold a micron-sized bead fixed in three directions, but the trap must first be calibrated in order to quantify the magnitudes of the forces at work. In these experiments, the optical trap was calibrated using the displacement method. The displacement method of calibration involves applying a known drag force to an optically trapped bead and measuring the bead's displacement relative to the applied force in order to calculate the stiffness, or spring constant, of the trap according to Hooke's Law defined in Equation 2-6:

$$F = kx \tag{2-6}$$

Once a bead is trapped, the NoahCorp quadrant photodiode (QPD) detects the amount of laser light that is transmitted through the sample. The QPD outputs three voltages: X, Y, and SUM [51]. The schematic of a QPD is presented in Figure 8.

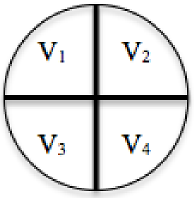

Figure 8: Depiction of the 4 quadrants in a quadrant photodiode.

The X voltage is defined as

$$X = (V_1 + V_3) - (V_2 + V_4) \tag{2-7}$$

the Y voltage is defined as

$$Y = (V_1 + V_2) - (V_3 + V_4)$$

(2-8)

and the SUM voltage is defined as

$$SUM = V_1 + V_2 + V_3 + V_4$$

(2-9)

The mirrors reflecting the laser light are adjusted until the laser is centered on the QPD (X and Y voltages read 0) while reaching as high a SUM as possible, thus indicating that the entire beam is projected onto the QPD. When external forces move the bead out of the center of the trap, laser light is reflected from the center of the QPD and changes the above readouts, allowing for precise monitoring of bead position without heavy image processing load.

After a bead was trapped, the stage was precisely moved as the location of the bead was monitored with both imaging and QPD. The stage position was controlled with a custom LABVIEW software program. In this process, the stage oscillates with a sinusoidal motion with amplitude 0.5 μm and frequency 5 cycles/sec, as shown in Equation 2-10.

$$x = 0.5sin(10\pi t)$$

(2-10)

Given this sinusoidal stage movement, the instantaneous velocity of the stage is defined in Equation 2-11 as the derivative of stage movement. This velocity is necessary in calculating the force applied to the bead.

$$v = 5\pi cos(10\pi t)$$

(2-11)

Oscillation of the stage causes the liquid media to apply a force on the trapped bead. This force can be calculated using a modified Stokes Law, shown in Equation 1-6. Because Stokes Law assumes laminar flow, the denominator in this equation uses the distance from the coverslip to account for any turbulence in the flow, caused by proximity of the flow to a wall or surface. In this case, the velocity used in this equation is the maximum velocity of the stage, which is 5π μm/s.

As the stage oscillates, the CCD camera images the location of the bead at 30.62 frames per second (fps). Particle tracking software was used to track the motion of the bead throughout the stage motion. This tracking software detects the centroid of the bead by comparing pixel intensities of each image to a reference image, given by Equation 2-12, where x_i is the pixel coordinate and I_{ij} is the intensity of that pixel [52]. The C_x value is the centroid of the position in the x direction. In this experiment, the particles were tracked using both the x and y coordinates of the centroid. These centroid values are stored as a set of coordinates that define the bead position over time.

$$C_x = \frac{\sum_{i=1}^{n} \sum_{j=1}^{m} (x_i \cdot I_{ij})}{\sum_{i=1}^{n} \sum_{j=1}^{m} (x_i \cdot I_{ij})}$$

(2-12)

This array of coordinates is processed using a LABVIEW tone measurement express VI. This VI analyzes the incoming data as a set of specific tones. These tones are generated by analyzing the data over a set of frequencies. The frequency at which the highest amplitude tone is observed is selected as the tone used to represent the signal. This amplitude is then used as the maximum displacement of the bead during oscillation.

According to Hooke’s Law in Equation 2-13, the trap stiffness can be calculated by dividing the position detected with imaging software by the force calculated from stage movement.

$$k = \frac{F}{x}$$

(2-13)

Additionally, this LABVIEW program calibrates the QPD through tone measurements similar to the image software algorithm. As the stage oscillates, the QPD samples the laser light at 30 kHz. The program then analyzes the voltage outputs provided by the QPD to find the tone with the highest amplitude. This amplitude represents the voltage that the QPD outputs when the bead is at maximum displacement. As a result, a measure of position/V_{QPD} can be obtained for use in future experiments. This single experiment provides both the spring constant of the trap and the nm/volt value necessary for more complex assays that use position measured by the QPD.

2.4 Optical Trap Characterization

The Qioptiq 850 nm 50 mW fiber coupled laser diode was tested for laser power using a digital voltmeter and found to output a power of 5 mW out of the objective. In order to find the best situation for optical trapping, the stiffness of the trap was evaluated at varying distances from a cover slip. The trap stiffness was calculated in both the x- and y-directions. The results from 5 μm beads are presented in Table 1 and Figure 9. It was found that a distance of 15 μm from the cover slip yields the strongest trap strength.

Table 1: Optical trap spring constants for 5 µm beads at varying distances from the cover slip. Data suggests that the trap is strongest at 15 µm (marked with asterisk) above the cover slip.

Distance (µm)	Mean X Stiffness (pN/ µm)	Mean Y Stiffness (pN/ µm)
5	2.69	2.97
10	2.87	3.30
15*	2.99*	3.44*
20	2.93	3.41
25	2.86	3.32
30	2.93	3.28
35	2.71	3.22
40	2.78	3.14
50	2.76	3.03
60	2.59	2.89

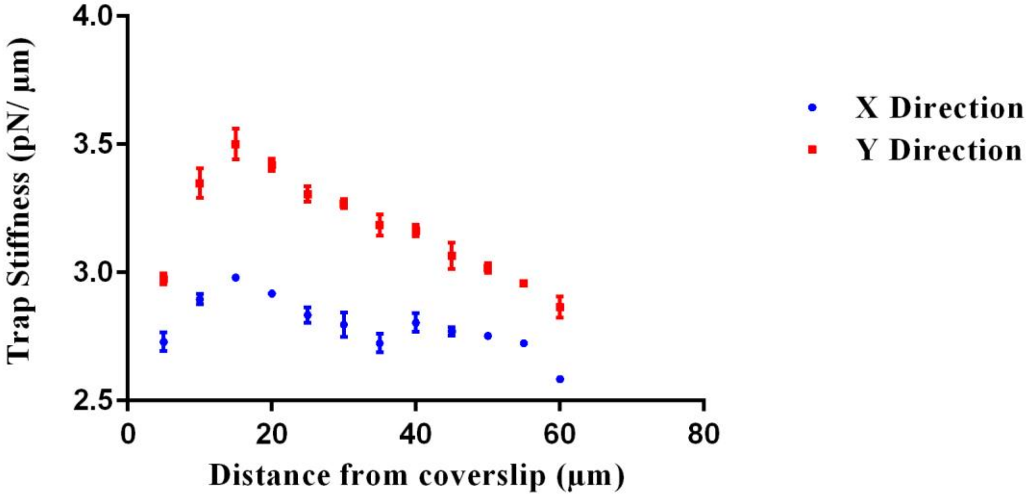

Figure 9: Optical trap spring constants for 5 µm beads at varying distances from the cover slip. Data suggests that the trap is strongest at 15 µm above the cover slip.

An additional laser, purchased for the Mechanobiology Lab late in the research timeline of this thesis, was a QPhotonics 1064 nm fiber laser coupled diode with variable power settings.

The laser diode controller uses an operating current to control the power of the laser. The laser powers were analyzed at various Iop values to determine the losses in the system. It was found that the laser power before the objective was significantly lower than the laser powers listed on the data sheet provided, as shown in Table 2 and Figure 10. These characterizations of the laser gave us a better idea of the energy losses caused by the microscope set up.

Table 2: Laser powers at varying operating currents, as controlled by the Arroyo Instruments laser diode controller. The laser power before the objective is significantly lower than the laser power listed in the data sheet. (Data collected by Seoyoung Son)

Iop (mA)	Data sheet Power (mW)	Out of Fiber (mW)	Before Objective (w/o prism; mW)	Before Objective (w/prism; mW)
150	40	22	14	14
200	70	53	31	24
250	100	80	47	36
300	130	107	63	49
350	160	133	79	60
400	190	158	94	72
450	220	183	109	84
500	250	208	125	96
550	280	232	139	107
600	310	256	154	118
650	340	279	169	130
700	370	302	183	141
750	400	324	197	152
800	430	346	212	163
850	460	367	226	173
900	490	389	240	184
950	520	410	254	195
1000	550	432	267	205

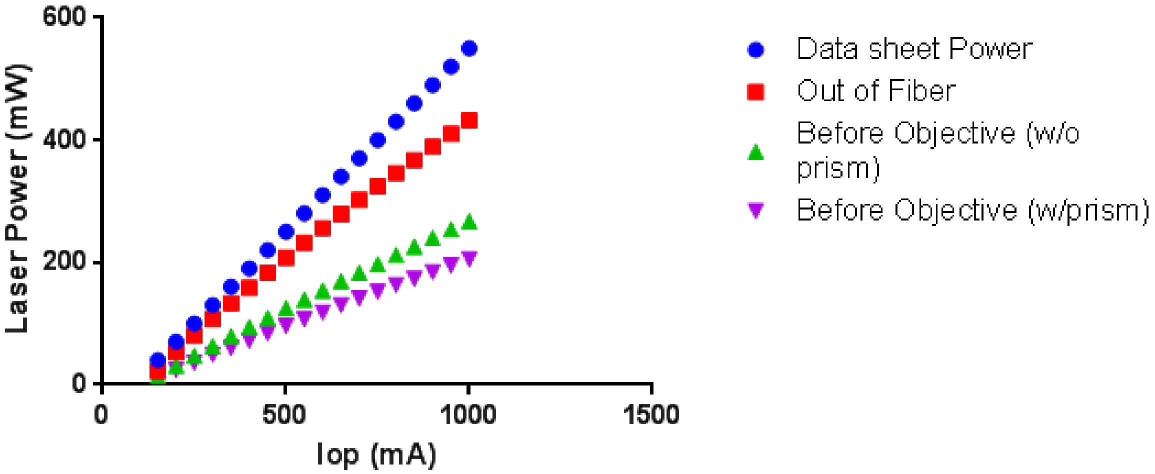

Figure 10: Laser powers at varying operating currents, as controlled by the Arroyo Instruments laser diode controller. The laser power before the objective is significantly lower than the laser power listed in the data sheet due to losses inherent in the microscope setup. (Data collected by Seoyoung Son)

2.5 Quantitative Measurement of Bead-Surface Contact

One of the major advantages of using the optical trap to study mechanotransduction is the ability to control and observe the exact time at which a force is applied. Because the research presented in this thesis involves measurements starting at the exact time of contact, the exact time of contact needed to be calibrated and defined. In the experiment, optically trapped beads are brought into contact by raising the stage position with a computer. Qualitatively, the operator can notice a change in the DIC image as soon as a bead touches a surface. The axial center of the trap is adjusted so that it is in the focal plane of the microscope, and the DIC imaging presents images with sharp detail and contrast. Therefore, as soon as a surface begins to push a bead out of the optical trap focal point and thus the focal point of the microscope, the bead changes appearance.

This change can be quantified through imaging, but in order to achieve the precision and speed necessary in adhesion experiments, the QPD SUM value was selected to measure contact point. The QPD SUM has been shown to correlate with axial bead position in the optical trap [53], but it must first be calibrated. The results of this calibration are shown in Figure 11.

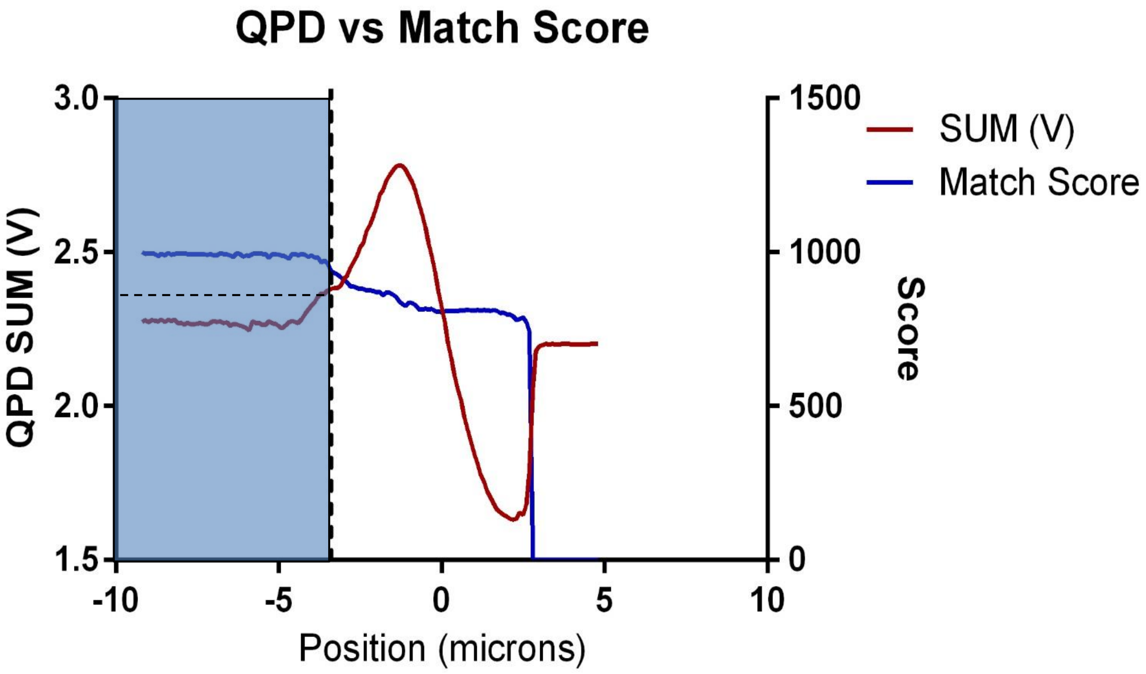

Figure 11: QPD SUM voltage vs. calculated Match Score. A 5 µm bead was trapped 10 µm above the surface of a glass slide. The slide was then raised in increments of 0.1 µm until the glass pushed the bead completely out of focus. QPD SUM voltage was recorded for each step, in addition to the LABVIEW IMAQ Match Score.

A 5 µm bead was trapped 10 µm above the surface of a glass slide. The slide was then raised in increments of 0.1 µm until the glass pushed the bead completely out of focus. QPD SUM voltage was recorded for each step. In order to quantify the changing appearance of the bead, the beads were tracked using a centroid-based particle tracking LABVIEW program that uses the Image Acquisition suite. This program uses cross-correlation particle tracking methods to locate the centroid of the bead and compare overall image likeness to the first image taken. A match score is produced for each image, in which 1000 means the given image is the exact same image as the reference and 0 means the given image is completely different from the reference image.

When the bead comes into contact with a surface, this match score begins to change. At this position, we recorded the QPD signal to use in further experiments. The normalized value was 1.05 times the reference value for the QPD. This value was used to determine bead contact points in all of the experiments described below.

2.6 Drift Correction Mechanism

The drift correction mechanism utilizes the epi path in the inverted Olympus microscope. In this path, light is emitted through a partially closed epi field path diaphragm and transmitted through the edge of the high NA objective in a similar manner to TIRF microscopy. This light reflects off of the coverslip and is collected again by the objective. A CCD camera is used to image the focal plane of the light. Using the reflected light provides a real measurement of distance between the cover slip and the objective. This distance can be quantified by analyzing the image of the field stop diaphragm with respect to changes in focus, as shown in Figure 32.

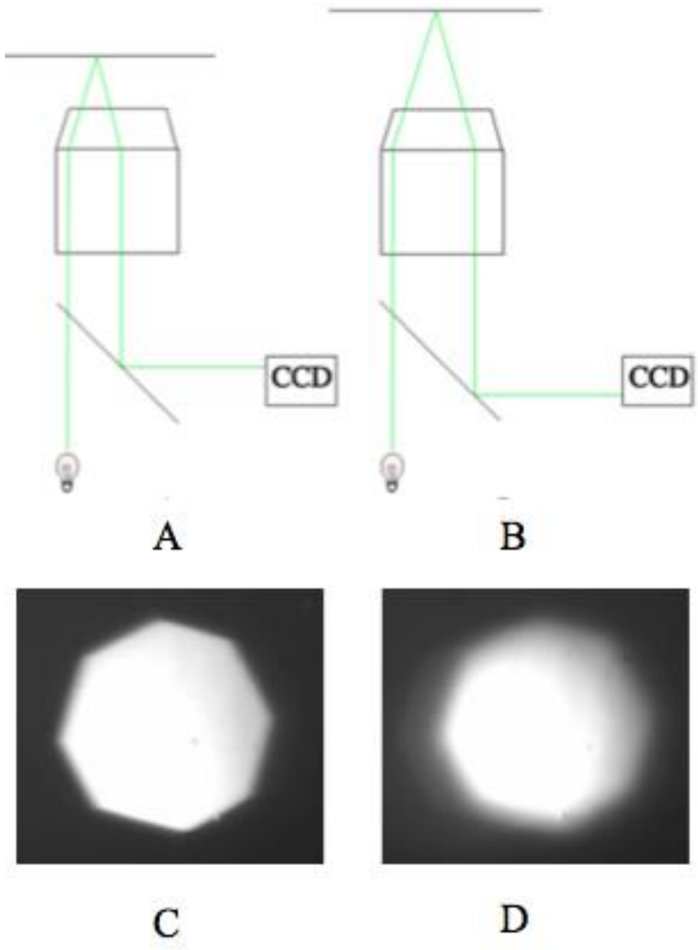

Figure 12: Monitoring of focal drift. Light from the epi pathway exits the edge of the objective and reflects off of the coverslip. A CCD camera is used to detect the deflection of the image plane. Focal drifts are ultimately detected image changes in the y-direction. 7A represents the light path of a focused microscope, with 7C depicting the image produced by the CCD camera. 7B represents the light path of a microscope undergoing focus drift, with 7D depicting the image produced by the CCD camera.

A LABVIEW program was developed to quantify this change and monitor the microscope focus drift over time. The image of the field stop diaphragm is processed as a total sum of intensities of all pixels in the image. The region of interest during autofocusing is a small region that contains the right edge of the diaphragm. When the stage moves further from the objective, the light is reflected such that the octagon image of the diaphragm shifts left, which results in a higher total intensity in the image. When the stage moves closer to the objective, the octagon image shifts right, which results in a lower total intensity in the image.

2.7 Cell Culture

All *in vitro* experiments were conducted using human aortic endothelial cells (HAECs) (Gibco Inc, Carlsbad, CA). The cells used in these experiments were cultured between 2nd and 8th passages in Falcon T25 flasks in human serum culture media. Cells were transferred to CO_2-independent media in Delta-T dishes (Bioptechs, Butler, PA) for experiments.

2.8 Cell Membrane Modifications

Benzyl alcohol was prepared by dissolving 168.6 μL of concentrated benzyl alcohol in 1 mL of ethanol. The benzyl alcohol was added to the cell culture dish after the addition of CO_2-independent media to create an environment of 10 mM benzyl alcohol and mixed via pipette mixing. The bead-cell adhesion assays were started immediately after the addition of benzyl alcohol.

2.9 Functionalization of Microbeads

Polystyrene beads were functionalized with fibronectin using the avidin-fibronectin binding complex, represented in Figure 13. The solution was prepared as 30 μL of streptavidin-coated 5 μm beads (Bangs Laboratories, Fishers, IN) of original concentration 10 mg/mL (1% solids w/v) were spun down and then washed three times with with 5% bovine serum albumin

(BSA) solution. The protein to be functionalized was prepared by washing 0.5 mg/mL of sterile fibronectin in dimethyl sulfoxide (DMSO).

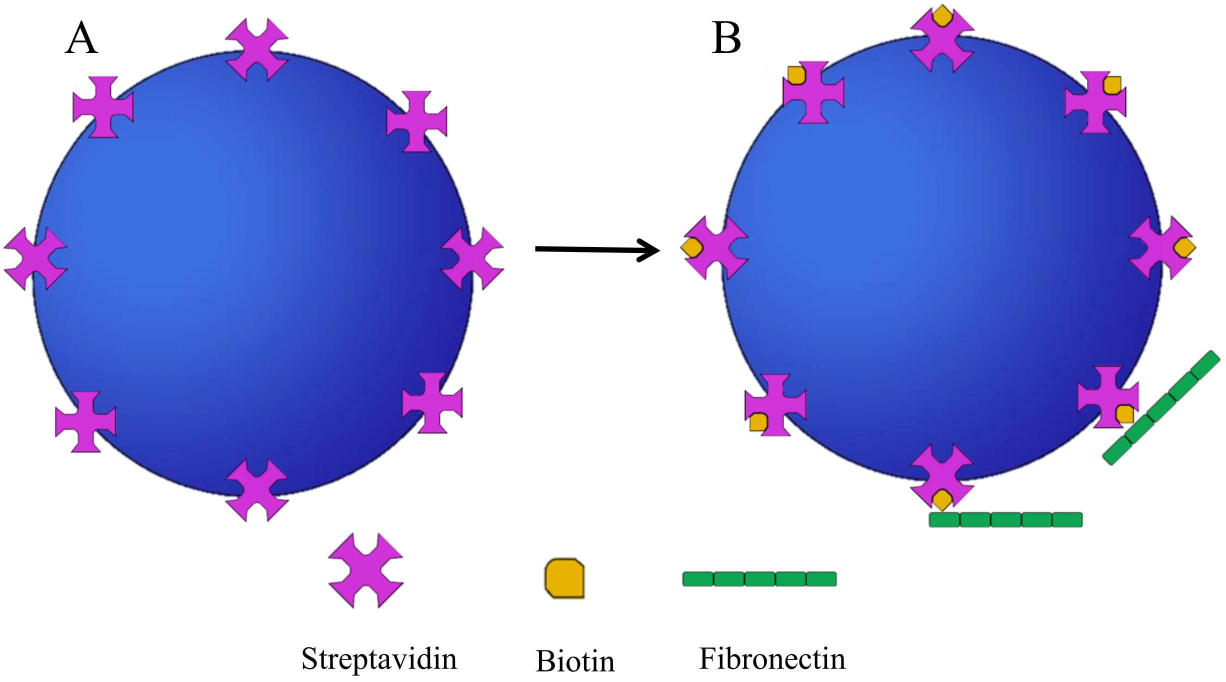

Figure 13: Functionalization of polystyrene beads. Streptavidin-coated beads (10A) were biotinilated and functionalized with fibronectin (10B).

Functionalization and biotinilation steps occurred in sterile conditions under a fume hood. The fibronectin was added to a solution of 10 mM of 0.5 mg/mL EZ-link NHS-LG-Biotin diluted in DMSO and incubated at 4 °C overnight. Excess unreacted biotin was removed through a microspin column (Harvard apparatus, G-25). The protein solution was then buffered with filtered PBS. The beads, diluted in BSA, were then added to the protein solution and incubated for 30 minutes with gentle mixing. The particles were then washed 3 times with PBS and re-suspended in the buffer and allowed to incubate overnight. An additional vial was prepared using

5 µL of particle solution and 5 µL of antibody solution. This vial was covered in foil and allowed to incubate overnight. Flow chamber slides of both fluorescent beads with antibodies and control beads without antibodies were analyzed to validate functionalization. After functionalization, beads were imaged to confirm fibronectin attachment. Figure 14 shows that fluorescence was observed in the antibody-labeled batch of functionalized beads, verifying the fibronectin binding.

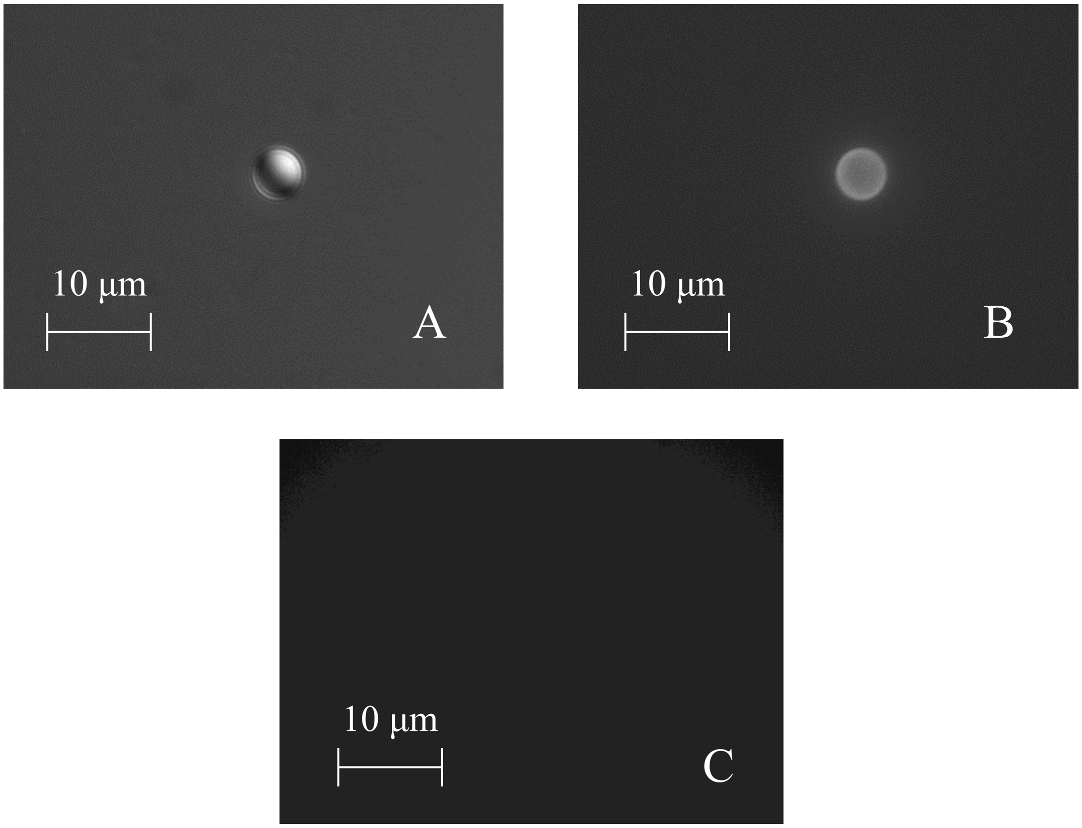

Figure 14: Images of functionalized beads. (A) A DIC image of FN-functionalized beads. (B) A FITC image of FN-functionalized beads with antibody. (C) A FITC image of FN-functionalized beads without antibody.

2.10 Variance-Based Bead-Cell Adhesion Assay Experimental Procedure

HAEC's suspended in 400 μL of CO_2-independent media were prepared in a cell culture dish and imaged with the inverted Olympus microscope. A Bioptechs Delta T stage heater and objective heater were both used to keep the cells at 37 °C. A custom culture dish cover was used to allow for oil immersion. Functionalized beads diluted 1:1000 in PBS were pipetted into the culture dish and DIC imaging was used to bring the membranes of the HAEC's into focus. The laser was then turned on and a bead was trapped. Calibration of the QPD and optical trap was conducted as described in Section 2.3.

A custom LABVIEW program was designed for precise movements and measurements during this experimental procedure. After the calibration steps were completed, the stage was manually controlled until a bead was about 10 μm above the cell membrane point of interest. Usually, this point of interest was a flat location on the cell membrane with no signs of established focal adhesions. The LABVIEW program recorded the X, Y, and SUM QPD signals at 500 Hz to monitor the location of the bead throughout the experiment. After an initial control measurement of 1 minute, the stage was gradually raised to bring the cells closer in contact with the bead. As the stage was raised in increments of 10 nm, the QPD signals were monitored. The approximate moment when the bead touched the cell was indicated by a 5% increase in the SUM QPD signal and the stage was programmed to stop moving. Live DIC imaging was used to endure that the bead stayed focused in the trap.

At this point, the drift correction mechanism was activated and all QPD signals were recorded. These measurements were recorded for 30-60 minutes at 500 Hz. Verification of binding occured after the experiment was conducted by manually raising or lowering the objective to attempt to lift the bead off of the cell. If the bead did not stay in the trap, binding was confirmed.

Control experiments for binding were conducted using non-functionalized beads using the same protocols. Binding was refuted if the beads stayed in the trap after the focal point of the laser was manually raised above the cell membrane.

2.11 Verification of Bead Tracking by QPD

Preliminary studies in the Mechanobiology Lab have suggested that the optical trap can be used to quantify time of adhesion by analyzing the variance or standard deviation of the beads at different states of contact. For example, it was shown that a free bead had a higher variance than a trapped bead, which in turn had a higher variance than an adhered bead. For these studies, centroid-based particle tracking was used to track the movement of the beads. However, this required large amounts of computer memory, which prevented experiments from running longer than 17 minutes [54].

In order to quantify the motion of beads for a longer amount of time and at a faster rate, the QPD X and Y signals were used to track the bead in this study. To ensure that the QPD measure was an accurate representation of bead position, the variance-based bead-cell adhesion assay was conducted with both the QPD and CCD camera recording the position of the bead. After the bead was brought into contact with the cell, the QPD data was recorded at 500 Hz. In addition, 500 images were taken every 5 minutes. These images were then tracked using the centroid-based LABVIEW particle tracking.

2.12 Data Processing

The bead was tracked in the x- and y-directions using the X and Y QPD signals. The signals were recorded for both a trapped bead and a bead in contact with the cell membrane. In order to correct for small-scale drifts and corrections, a running average of 3 points was used when calculating bead position. After that, a running standard deviation with a window of 10 points was calculated. This standard deviation measurement was plotted over time and used as an indicator to monitor changing bead states.

2.13 Escape Force-Based Bead-Cell Adhesion Assay Experimental Procedure

Another method, named the escape force-based bead-cell adhesion assay, was employed to analyze the temporal factors in early adhesion induction. In these experiments, a fibronectin-functionalized bead was brought into contact with the surface of a human aortic endothelial cell for a given amount of time and then pulled away from the cell. This process was repeated with increasingly longer contact times until the bead adhered to the cell.

HAEC’s suspended in 400 μL of CO_2-independent media were prepared in a cell culture dish and imaged with the inverted Olympus microscope. A Bioptechs Delta T stage heater and objective heater were both used to keep the cells at 37 °C. A custom culture dish cover was used to allow for oil immersion. Functionalized 5 μm beads diluted 4:1000 in PBS were pipetted into the culture dish and DIC imaging was used to bring the membranes of the HAEC’s into focus. The 1064 nm laser was then set to 50 mW and a bead was trapped. Calibration of the QPD and optical trap was conducted as described in Section 2.3.

Another custom LABVIEW program was developed to automate the experimental process, shown in Figure 15. The bead was manually positioned above either the leading edge or the trailing edge of a cell. The stage was then automatically raised until the bead was in contact with the cell, using the algorithm outlined in Section 2.6. Once the bead was in contact with the cell, it was held in contact for a given amount of time. Then, the stage was moved laterally at 5 μm/s to bring the bead out of contact with the cell. With this relatively slow loading rate, the expected rupture force is around 40 pN [55] .The direction of movement (backwards or forwards in the x- or y-direction) could be controlled for each individual bead trial. After movement away from the cell, the program waits 5 seconds until returning the bead to the original position above the cell, where the program waits for an additional 5 seconds. These wait times are implemented in order to allow for recruited integrins to diffuse out of the adhesion site [56]. This contact time began at 0 seconds and was increased by 1 second until the bead was adhered strongly enough to the cell that it was able to escape the trap.

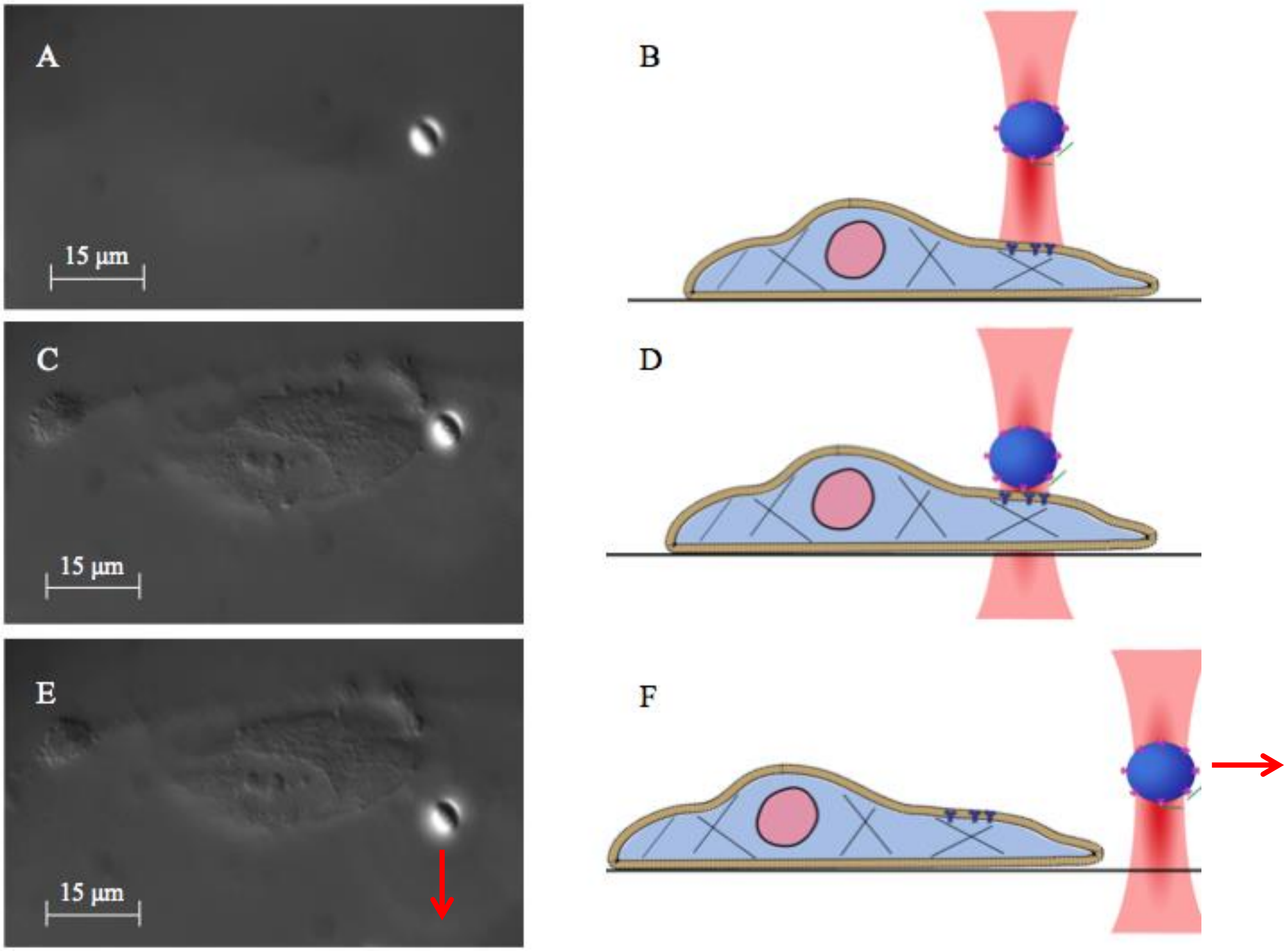

Figure 15: Experimental design of the time to adhesion-based bead-cell adhesion assay. Figures 15A, C, and E are images taken during an experiment with the top view, while Figures 15B, D, and F are side-view schematics.

For each iteration of this contact and movement technique, the QPD measured the location of the bead in relation to the center of the trap in order to calculate the escape forces of the bead, shown in Figures 16-18. The minimum escape force was defined as the maximum force recorded in the contact time that was 1 second shorter than the contact time of adhesion.

The force was calculated using the raw QPD ΔV data shown in Figure 17. Prior to each bead-cell trial, the force drag method described in Section 2.3 was employed to find values for

QPD voltage per nanometer, in addition to the optical trap stiffness, in pN/μm. The force was obtained from these values, as shown in Equation 2-14.

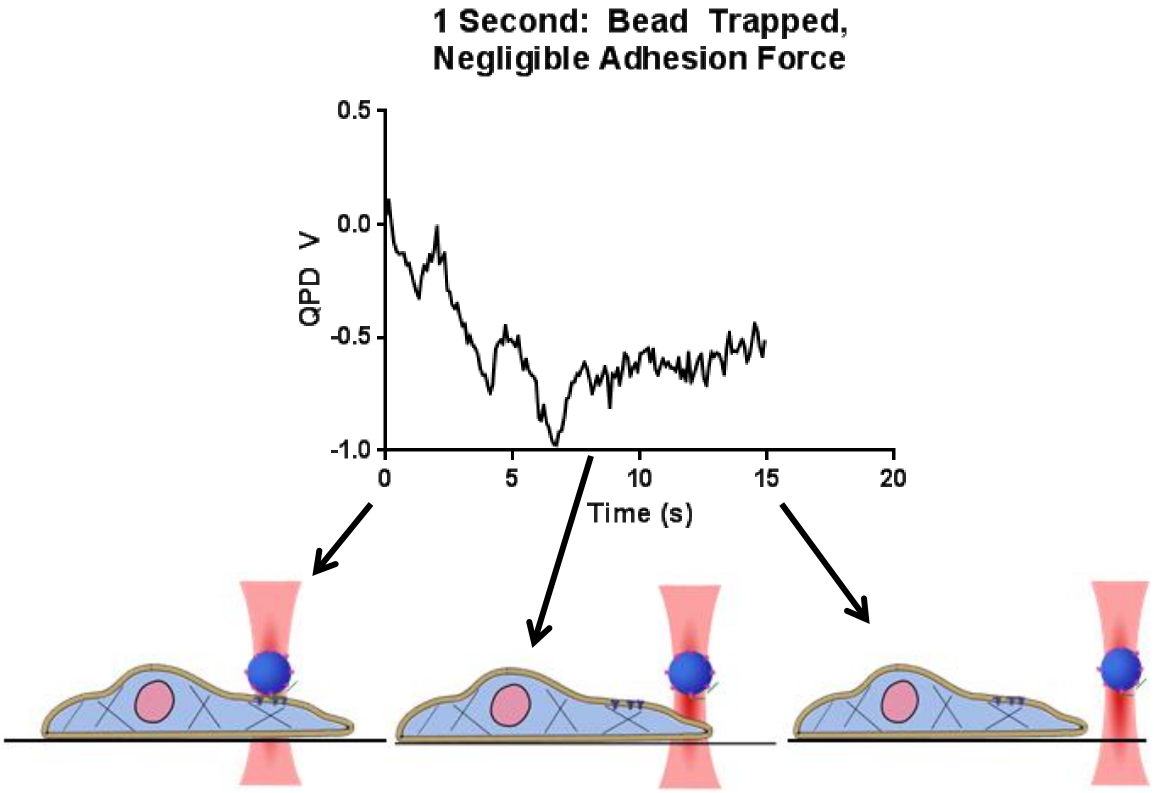

Figure 16: QPD voltage readout and system schematics of the adhesion force-based bead-cell adhesion assay for a 1 second adhesion time. This data was not used to calculate adhesion time, as there was negligible observed adhesion force.

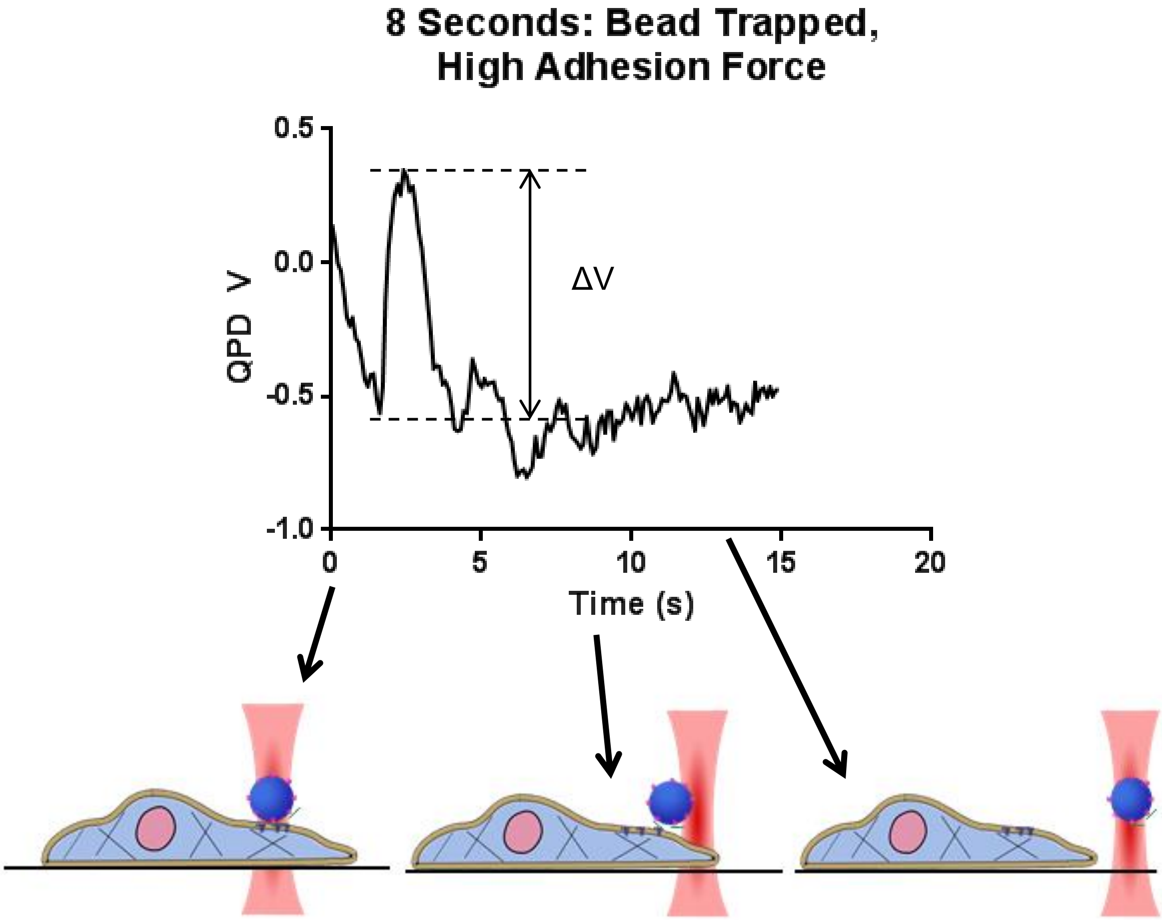

Figure 17: QPD voltage readout and system schematics of the adhesion force-based bead-cell adhesion assay for an 8 second adhesion time. This data was used to calculate adhesion time, as it was the time point before the bead escaped the trap. The amplitude of the spike in QPD voltage indicated by the distance between the dashed lines (ΔV) was used to calculate the adhesion force measure.

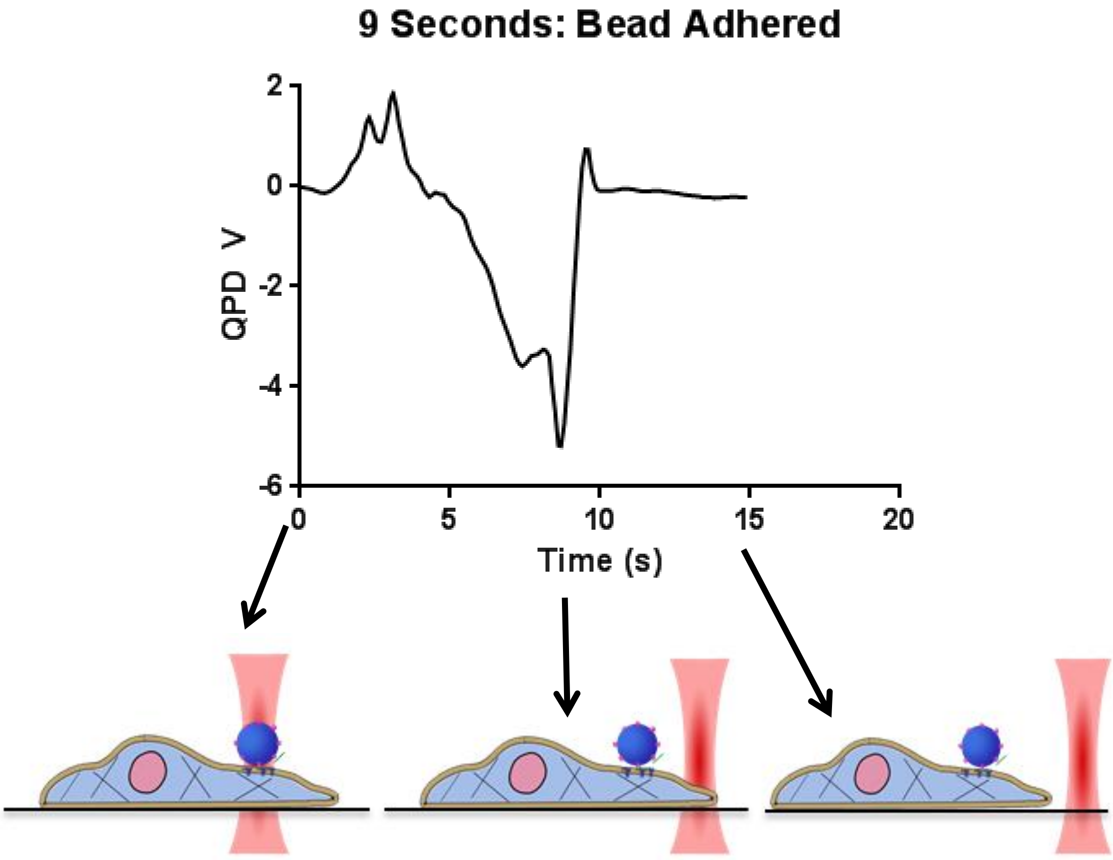

Figure 18: QPD voltage readout and assay schematics of the adhesion force-based bead-cell adhesion assay for a 9 second adhesion time. At this point, the bead was adhered to the cell and escaped the trap. The QPD data from this time point was not used to calculate adhesion force.

$$Force = \frac{QPD\ \ \Delta V * Trap\ Stiffness(\frac{pN}{\mu m}) * measured\ \frac{nm}{V}\ value}{1000}$$

(2-14)

When the QPD data was obtained after moving the bead away from the cell, the peaks can be analyzed to quantify the forces at work in the experiment. Generally, before a bead was completely adhered, bonds were formed between the fibronectin on the bead and the integrins in the cell membrane. As the trap moved away from the cell, if the trap force was greater than the force of adhesion, the bead would spring back into the center of the trap after some amount of resistance. When the trap force was less than the force of adhesion, the bead remained adhered as the trap moved away from the cell.

When the beads were able to escape the optical trap, the QPD signal presents a massive spike, representing the bead completely escaping the trap. However, the trap stiffness only correlates linearly with the QPD voltage up to 2 μm from the trap center. So, the QPD signal observed in the adhesion trial presents a “false spike” (see Figure 18) and does not represent actual force applied. Therefore, the force value measured in the trial before the bead was stuck (Figure 17) can be designated as the maximum force at which the bead stays trapped.

Chapter 3

RESULTS

3.1 Verification of Drift Correction

The drift correction mechanism was verified through comparative testing. First, studies were conducted in order to verify that the light intensity of the CCD image accurately measured the effective distance between the objective and the cover slip. In these experiments, the drift correction setup was performed as described earlier. Then, the intensity value was monitored as the stage z-position was automatically modified with a custom LABVIEW program. This process was conducted 7 times in a flow chamber regime and resulted in the calibration curves shown in Figure 19.

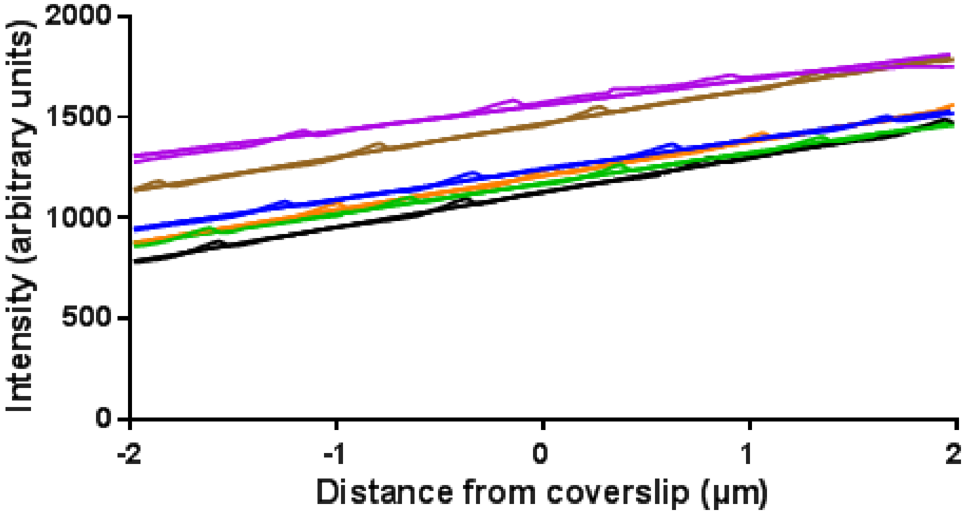

Figure 19: Drift correction individual calibration curves. For each trial (N=7), the stage was moved 4 microns in the z direction while measuring the light intensity value. The y axis represents an arbitrary intensity measure while the x axis represents microns moved in the z direction.

This calibration proved that there is a linear relation between intensity of the back focal plane image and distance between the objective and the coverslip. Multiple trials (N=7) were conducted and the average slope was found to be 155 +/- 2.864 intensity units per micron (0.155/nm), with an R^2 value of 99.64.

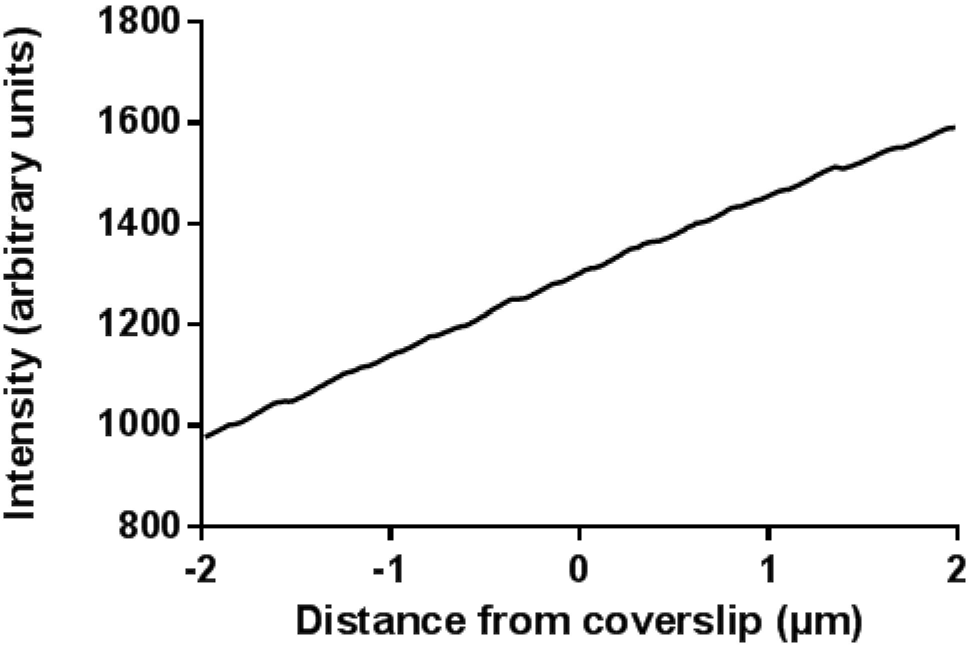

Figure 20: Average drift correction calibration curve. This figure represents the average of the calibration curves depicted in Figure 19. The slope was found to be 155 +/-2.8 units/micron.

After the intensity of the image in the back focal plane had been confirmed to measure focus drift in the microscope, experiments were conducted to compare the focus drift in drift correction state and in default state. First, the microscope was set up at 21 °C using the flow chamber regime. The intensity was monitored at 500 Hz for 8 minutes without drift correction, shown as the blue data points in Figure 21. The same procedure was then followed for the microscope with drift correction, which is represented as the red data points in Figure 21.

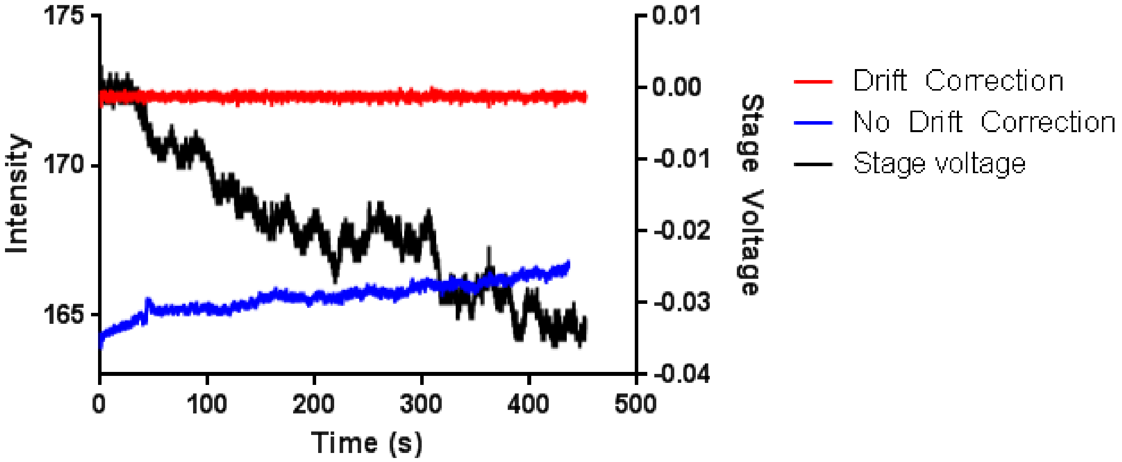

Figure 21: Intensity values for a microscope with and without drift correction. Drift correction using intensity-based PID control allows for long-term focus drift correction. Additionally, Total stage voltage correction accounts for less than 4 microns.

Figure 21 shows that in a non-drift correction microscope, the intensity measure drifts from 164.03 to 166.89. Using the calibration constant calculated in Figure 20, this drift is found to be 18.45 nm. In the drift correction trial, the average intensity signal remained constant for the 8 minutes of sampling. The amplitude of this signal was 0.46. Again, using the calibration constant calculated in Figure 19, the standard deviation was found to be 0.07 nm, with a peak-to-peak error value of 2.96 nm.

Similar results were observed under the temperature-controlled Delta T dish regime. However, due to temperature control, the inherent focus drift is much more pronounced. Due to the inefficiencies in the Delta T temperature controller, the temperature can fluctuate between 36.9 °C and 37 °C, in addition to longer-term drift. The data presented in Figure 22 suggest that the drift correction algorithm is able to combat long-term drifts and decrease the effect of temperature fluctuation-based drift. Using the calibration constant calculated in Figure 19, the standard deviation was found to be 178.97 nm, with a peak-to peak error value of 146.9 nm.

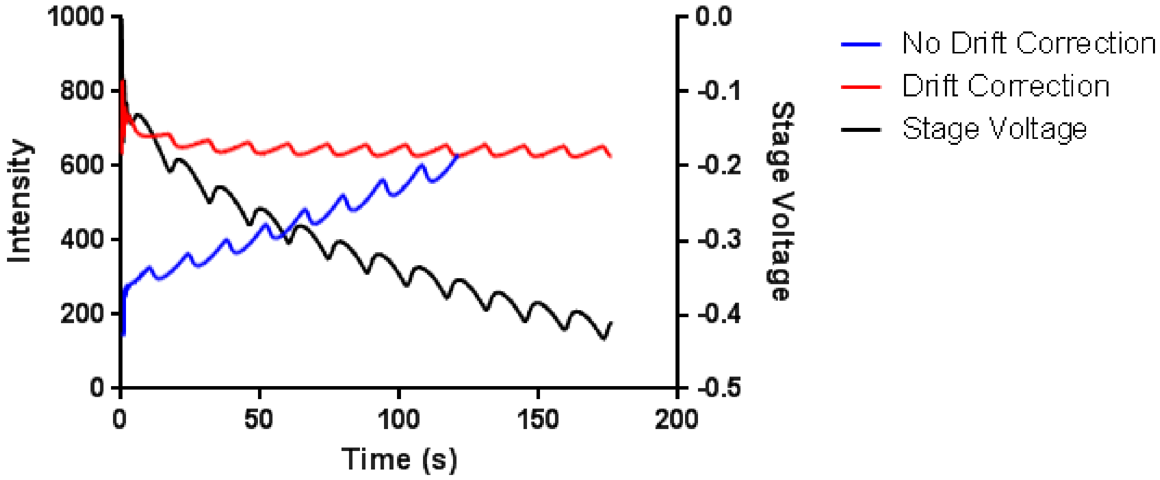

Figure 22: Intensity values for a microscope with and without drift correction in a temperature-controlled Delta T dish regime. The blue data indicate the microscope not in drift correction state, and suggests focal drift. The red data represent the microscope under drift correction. The green data indicate the change in stage voltage applied as part of the drift correction algorithm.

Although the focus drift correction algorithm in place is effective in combatting long-term drift, it is currently not fast enough to correct for smaller fluctuations due to temperature control. A faster, more sensitive method of collecting the reflected epi pathway light is necessary in order to achieve optimal focus drift correction.

3.2 Variance-Based Bead-Cell Adhesion Assay Experimental Results

In order to confirm that QPD bead detection was as accurate as centroid-based imaging detection used in previous studies, images were taken every 5 minutes in a variance-based bead-cell adhesion assay and analyzed for variance. These images were used to track the bead, resulting in a calculation of variance for every 5 minutes of the assay. These values were then compared to the running variance calculated using the QPD measurements in order to confirm that the QPD was an effective method of bead tracking. The data presented in Figure 23 show that the QPD and imaging variances are consistent.

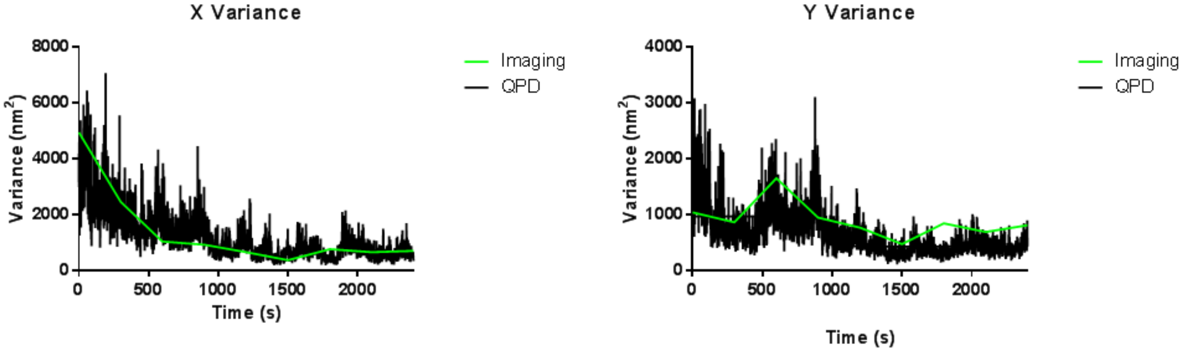

Figure 23: Comparison of Imaging-based and QPD-based variance calculation. For both the x-direction and the y-direction, the QPD signal matched the imaging.

Variance-based cell-bead adhesion assays were conducted using fibronectin-functionalized 2 μm beads and HAECs. These adhesion assays were carried out many times, with varying results.

The functionalized bead was brought into contact with a cell and the QPD signals were recorded at 250 Hz for over 23 minutes. In postprocessing, the QPD signal was multiplied by the calibration factor calculated in the experimental preparation steps in order to define an array of tracked bead positions in both the x- and y-directions. These calculated positions were then subtracted from a running average of 100 data points in order to normalize the position measurement. Then, the variance was calculated for every 250 points in the data set, resulting in one variance value for every second of the experiment.

A sigmoidal dose-response curve with varying slope was fit to the data to measure the characteristic time of adhesion of the bead to the cell. An effective half-maximal LogEC50 value is defined here as the time at which the variance is halfway between the higher variance state (trapped but not adhered) and the lower variance state (adhered to cell). The equation for this sigmoidal fit is described in Equation 3-1.

$$Y = Bottom + \frac{(Top - Bottom)}{1 + 10^{(LogEC50 - X) * HillSlope}}$$

(3-1)

In the most successful trial, presented in Figure 24, the characteristic time of adhesion according to the variance in the x-direction was 1060 seconds, or 17.67 minutes. The variance of the bead as it was trapped but not adhered was 7970 nm^2, and the variance in the adhered state was 2858 nm^2.

In the y-direction variance, the characteristic time of adhesion was 968 seconds, or 16.13 minutes. The variance of the bead as it was trapped but not adhered was 5850 nm^2, and the variance in the adhered state was 376.6 nm^2.

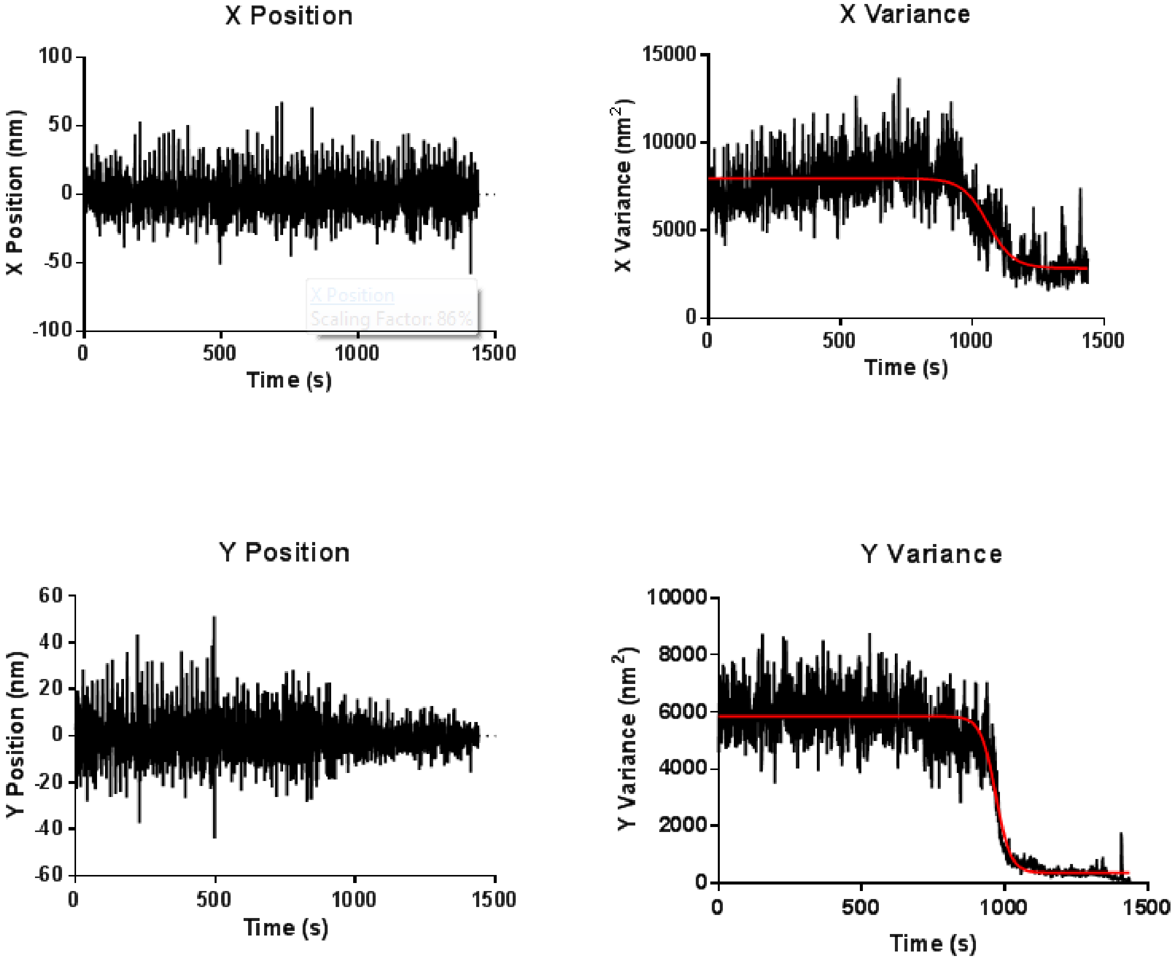

Figure 24: Characteristic time of adhesion of a fibronectin-functionalized 2 μm bead to a human aortic endothelial cell. A sigmoidal dose-response curve with variable fit was applied to the variance data to define the time of adhesion. In the x-direction, the characteristic time of adhesion was found to be 17.67 minutes with an R^2 value of 0.7144. In the y-direction, the characteristic time of adhesion was found to be 16.13 minutes with an R^2 value of 0.9157.

However, many trials of the variance-based bead-cell adhesion assay did not produce results that allowed for calculation of characteristic adhesion time. In many trials, the variance did not decrease over time, the sigmoidal fit was not able to converge, and so no evidence of adhesion was observed. Data collected from these trials can be found in Appendix C.

In an effort to improve the efficiency and quality of the variance-based assay, the experiment was conducted using 5 μm beads and the focus drift correction mechanism described earlier. In this trial, represented by Figure 25, the X,Y, and SUM readouts of the QPD were recorded, with the SUM used to represent the z-direction. However, only the variance curve in the y-direction was able to converge when fit with a sigmoidal does-response variable slope curve. The characteristic time of adhesion was found to be 976 seconds, or 16.27 minutes. The variance of the bead as it was trapped but not adhered was 963.4 nm^2, and the variance in the adhered state was 428.9 nm^2. The characteristic time observed is close to what was observed with 2 μm beads. The differences in variance are most likely due to the size and thermal motion of the beads.

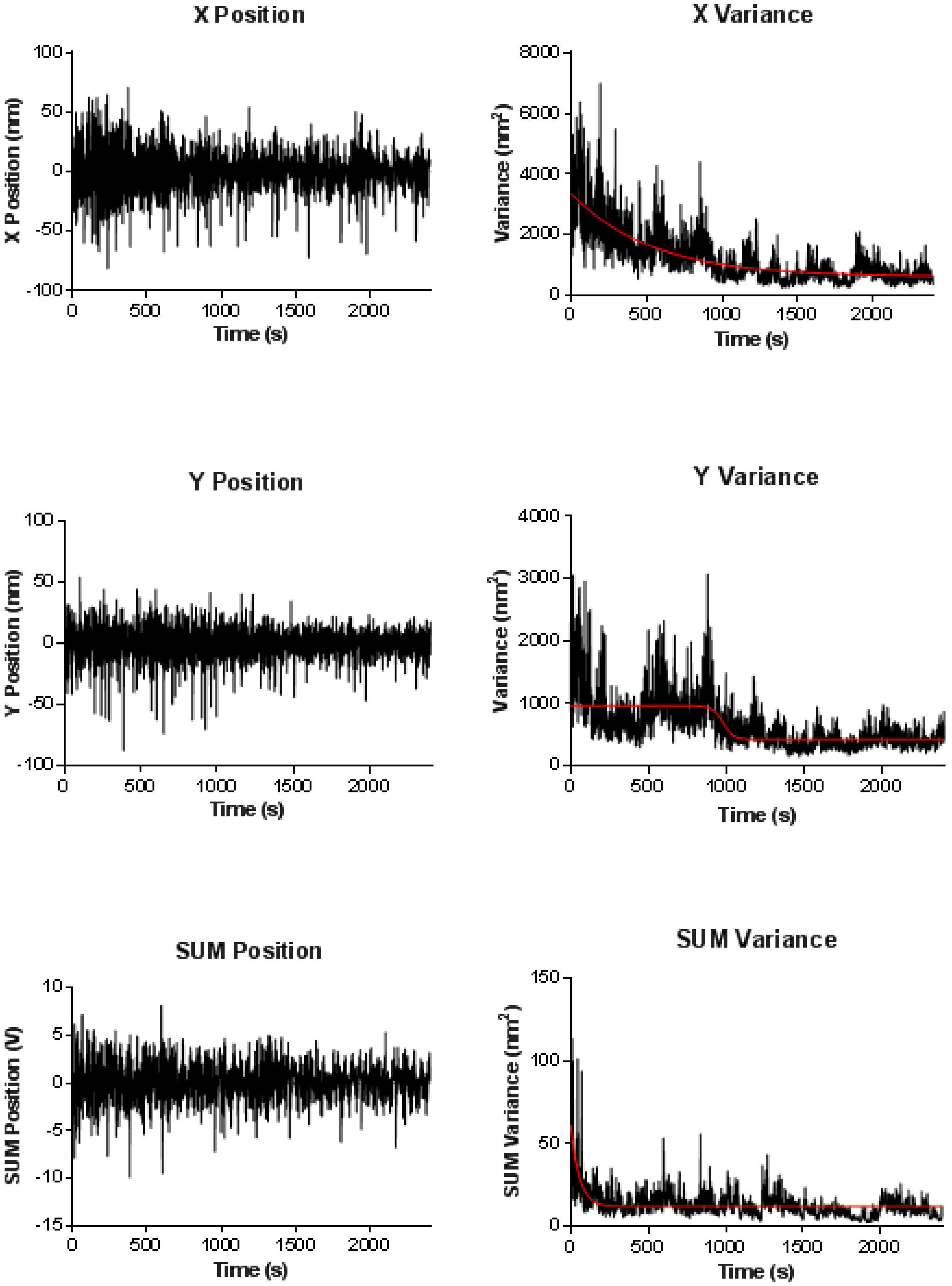

Figure 25: Characteristic time of adhesion of a fibronectin-functionalized 5 µm bead to a human aortic endothelial cell. A sigmoidal dose-response curve with variable fit was applied to the variance data to define the time of adhesion. In the y-direction, the characteristic time of adhesion was found to be 16.27 minutes with an R^2 value of 0.4198. The variance in the x- and z-directions were unable to converge.

3.3 Escape Force-Based Bead-Cell Adhesion Assay Experimental Results

The escape force-based bead-cell adhesion assay was conducted for three conditions: fibronectin-functionalized bead in contact with an unaltered cell membrane, fibronectin-functionalized bead in contact with a cell membrane altered with benzyl alcohol, and a control experiment with a non-functionalized bead in contact with an unaltered cell membrane. Additionally, this assay investigated a difference in adhesion dynamics between the leading edge and trailing edge of a human aortic endothelial cell. The key experimental targets in these assays were time to adhesion and adhesion force.

In the control experiment, the assay was conducted with non-functionalized 5 μm beads and endothelial cells with unaltered cell membranes. This experiment observed very long times to adhesion. In some trials, the bead did not stick to the cell after 60 seconds of adhesion, at which time it was assumed that the bead would not adhere. These data points are represented by "N/A" in Table 3 and Table 4, as no time to adhesion nor adhesion force could be measured.

Table 3: Time to adhesion and adhesion force for the control non-functionalized beads in contact with the leading edge of unaltered cell membranes. Each trial represents a unique bead and unique cell.

Leading Edge	
Time to Adhesion (s)	Adhesion Force (pN)
21	2.865
N/A	N/A
23	0.946
17	0.393
N/A	N/A

Table 4: Time to adhesion and adhesion force for the control non-functionalized beads in contact with the trailing edge of unaltered cell membranes. Each trial represents a unique bead and unique cell.

Trailing Edge	
Time to Adhesion (s)	Adhesion Force (pN)
36	1.442
27	0.509
N/A	N/A
32	2.169
18	1.678

After disqualifying the trials in which the bead did not adhere, the leading edges and trailing edges of the cells were not found to be significantly different, either in terms of escape time (P=0.1617) and in escape force (P=0.9515), as shown in Figure 26.

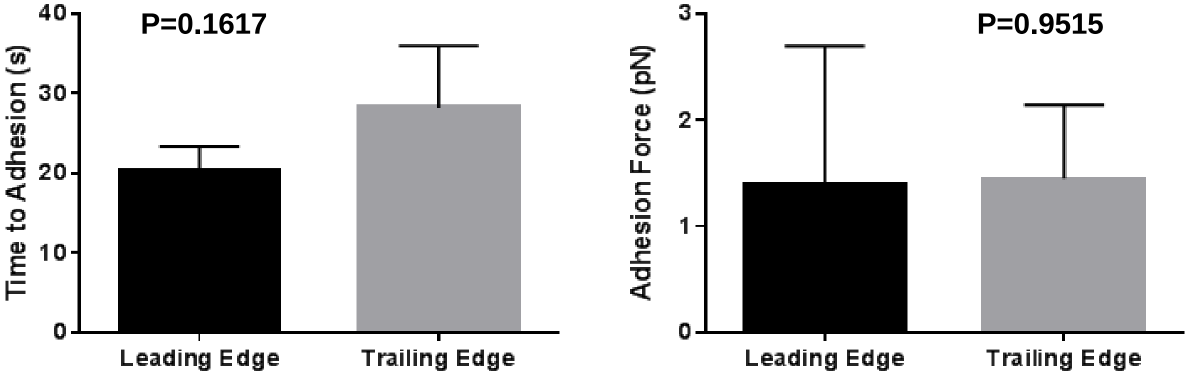

Figure 26: The leading edge and trailing edge of cells in contact with non-functionalized beads are not significantly different, both in terms of time to adhesion (P=0.1617) and in adhesion force (P=0.9515).

The assays conducted with fibronectin-functionalized beads and endothelial cells with unaltered membranes (no benzyl alcohol added) are represented by Tables 5 and 6 and Figure 27. These experiments observed increased escape force and decreased escape time in the leading edge of cells. Unpaired t tests showed that the adhesion force was significantly different

(P=0.0159) between leading and trailing edge, while escape time was not (P=0.2698). Both the leading and trailing edges of the cells suggested a relatively strong linear relationship between time to adhesion and adhesion force. The leading edge and trailing edge had R^2 values of 0.6239 and 0.4253, and slopes of 0.78 and 0.58 pN/s, respectively.

Table 5: Time to adhesion and adhesion force for FN-functionalized beads in contact with the leading edge of unaltered cell membranes. Each trial represents a unique bead and unique cell.

Leading Edge	
Time to Adhesion (s)	Adhesion Force (pN)
11	17.939
14	22.95
6	13.055
8	17.46
9	14.194
12	16.3
15	8.362

Table 6: Time to adhesion and adhesion force for FN-functionalized beads in contact with the trailing edge of unaltered cell membranes. Each trial represents a unique bead and unique cell.

Trailing Edge	
Time to Adhesion (s)	Adhesion Force (pN)
14	13.789
9	5.097
17	7.884
20	12.832
13	9.36
8	6.246
9	8.362
9	4.02

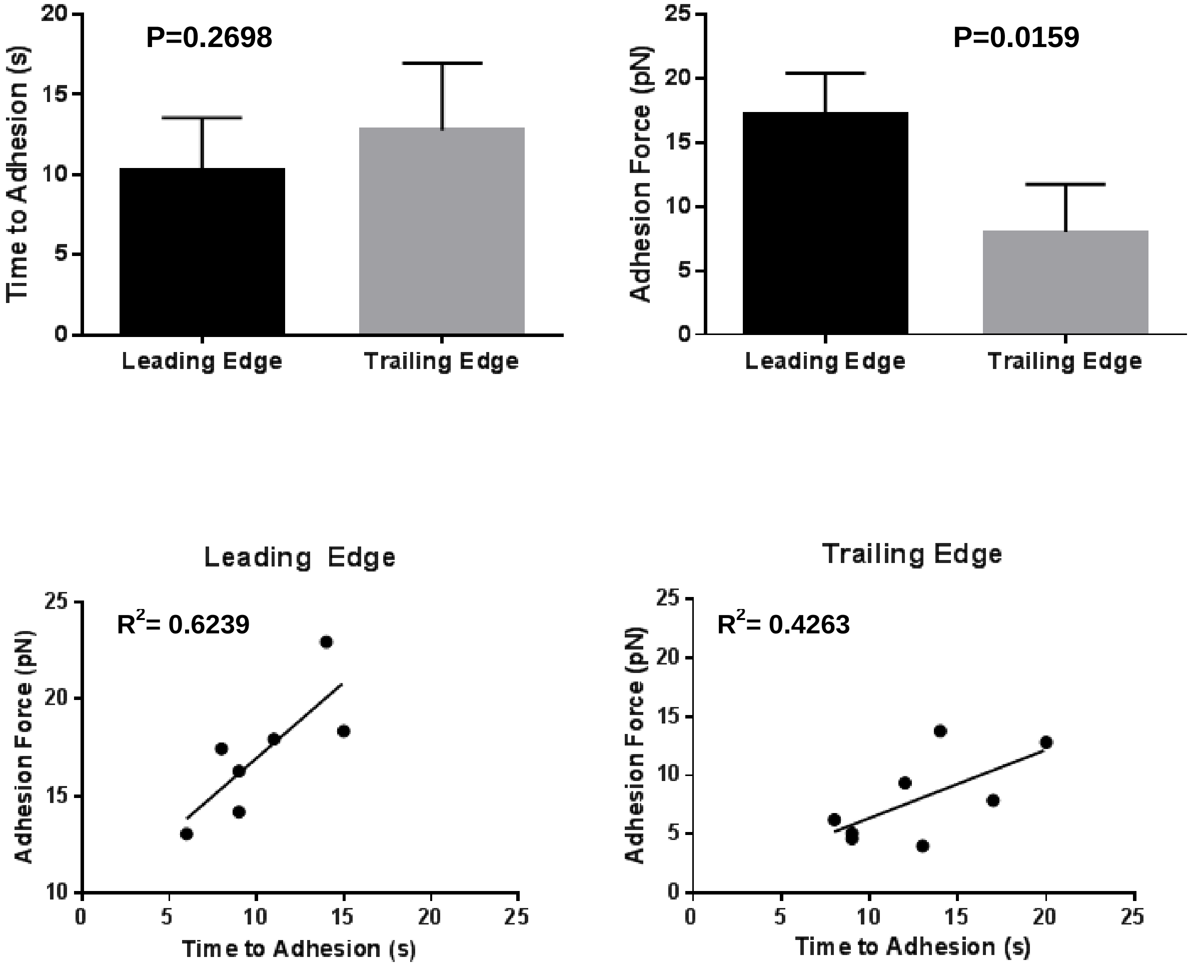

Figure 27: The leading edge and trailing edge of cells in contact with FN-functionalized beads are not significantly different time to adhesion (P=0.2698) but are significantly different in terms of adhesion force (P=0.0159). In addition, both the leading and trailing edges showed relatively strong linear correlations.

Assays conducted with endothelial cells treated with benzyl alcohol (BA) in contact with fibronectin-functionalized beads are represented by Tables 7 and 8, and Figure 28. These experiments did not exhibit any difference in time to adhesion or adhesion force. Unpaired t tests showed that neither the time to adhesion (P=0.3581) nor the adhesion force (P=0.7851) showed significant difference between the leading and trailing edge of the cell. Both the leading and trailing edges of the BA-treated cells suggested a relatively strong linear relationship between time to adhesion and adhesion force. The leading edge and trailing edge had R^2 values of 0.1887 and 0.6844, and slopes of 1.41 and 0.95 pN/s, respectively.

Table 7: Time to adhesion and adhesion force for the FN-functionalized beads in contact with the leading edge of cell membranes treated with benzyl alcohol. Each trial represents a unique bead and unique cell.

Leading Edge	
Time to Adhesion (s)	Adhesion Force (pN)
4	9.456
6	7.36
7	25.502
8	9.168
2	6.786

Table 7: Time to adhesion and adhesion force for the FN-functionalized beads in contact with the trailing edge of cell membranes treated with benzyl alcohol. Each trial represents a unique bead and unique cell.

Trailing Edge	
Time to Adhesion (s)	Adhesion Force (pN)
7	9.296
3	10.811
11	13.438
13	21.16
4	9.172

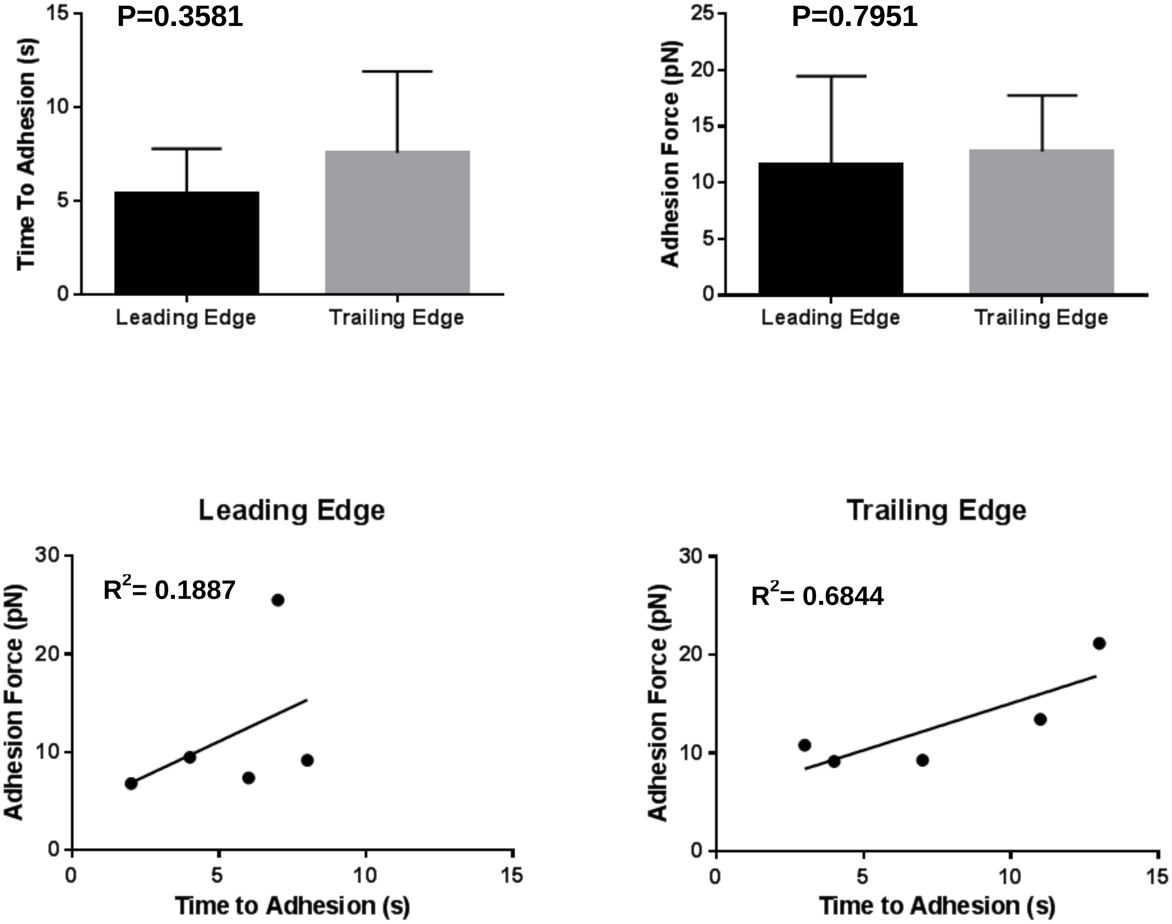

Figure 28 The leading edge and trailing edge of cells treated with benzyl alcohol in contact with FN-functionalized beads are not significantly different time to adhesion (P= 0.3581) or t in terms of adhesion force (P=0.7951). Both the leading and trailing edges show a relatively linear relationship between time to adhesion and adhesion force.

In general, the addition of benzyl alcohol resulted in both lower time to adhesion and lower minimum escape force, as shown in Figure 29. The observed time to adhesion was 36.20 +/-20.5 seconds for the control, 6.5 +/- 3.0 seconds for benzyl alcohol, and 11.60 +/- 4.5 seconds for no benzyl alcohol. The observed minimum escape force was 1.429 +/- 0.8 pN for the control, 12.21 +/- 6.2 pN for benzyl alcohol, and 13.14 +/- 5.5 pN for no benzyl alcohol. The time to adhesions for cells treated with benzyl alcohol was significantly different from cells without benzyl alcohol was found to be significantly different, with a P value of 0.021. The escape forces, however, were not found to be significantly different, with a P value of 0.8798.

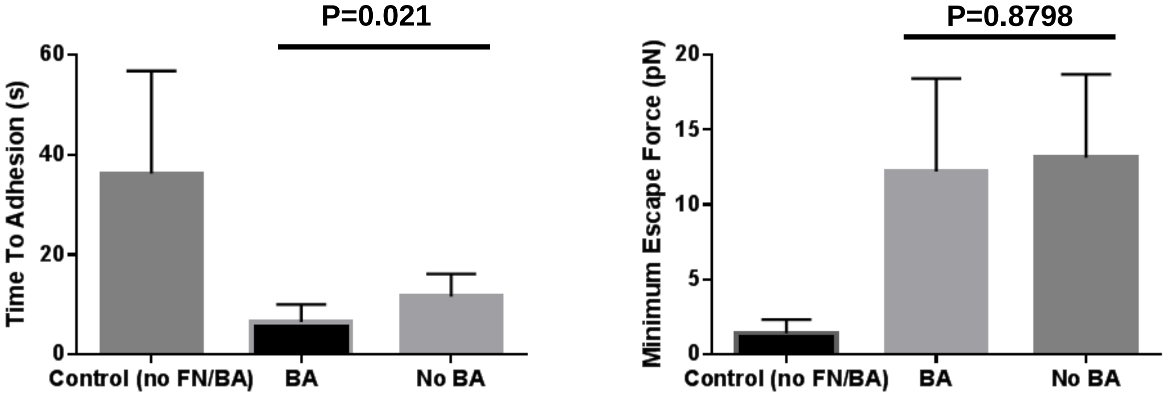

Figure 29: Comparison of all samples, both leading and trailing edge, in the three experimental states tested in the escape force-based bead-cell adhesion assay. The observed time to adhesion was 36.20 +/-20.58 seconds for the control, 6.5 +/- 3.04 seconds for benzyl alcohol, and 11.60 +/- 4.502 seconds for no benzyl alcohol. The observed minimum escape force was 1.429 +/- 0.897 pN for the control, 12.21 +/- 6.216 pN for benzyl alcohol, and 13.14 +/- 5.572 pN for no benzyl alcohol.

Chapter 4

DISCUSSION

The results have shown that the optical trap is an effective tool for measuring early adhesion events through investigation of cellular forces acting on a trapped bead.

4.1 Variance-Based Bead-Cell Adhesion Discussion

Although the variance-based bead-cell adhesion assays did not exhibit results consistent with the preliminary data observed in previous Mechanobiology Lab studies, the experimental procedure still has potential to precisely characterize membrane adhesion events in the future. Preliminary studies had shown discrete adhesion times marked by large, constant changes in standard deviation [54]. Additionally, it was hypothesized that small changes in variance would be much more easily discerned, with the hope of being able to identify individual integrin-fibronectin bonds forming.

Though these preliminary results were generally unable to be replicated, significant steps were taken to fine-tune the hardware, data processing, and experimental procedure in order to provide accurate results in the future. Most of the assays used 2 μm beads with the ultimate goal of relating membrane bending to early adhesion dynamics. It is hypothesized that a bead with a smaller diameter will cause greater membrane bending when in contact with the cell. However, previous studies have shown that a bead must have at least a 5 μm diameter in order to provide enough force to induce a focal adhesion without added applied force [57]. The goal of this study was to apply minimal force to the membrane in order to study how the membrane reacts in response to the smallest of stimuli. Additionally, the 5 mW, 830 nm laser used in the majority of this thesis did not posess an axial stifness capable of applying the necessary force. Therefore, it is difficult to assume that a 2 μm bead with no force applied is alone capable of inducing focal adhesions. Using 5 μm beads allows for a greater level of confidence that focal adhesion dynamics are occuring in response to the contact with the optically trapped bead. However, the 5 μm bead essentially acts as a flat surface to the cell, causing minimal membrane bending. This trade-off between effective focal adhesion induction and membrane bending must be more strongly considered in future experiments.

Another major improvement made towards this assay was the introduction of the drift-correction algorithm. Focal drift has been an issue with the system for a few years and has prevented the lab from obtaining truly reliable data on a nanometer-level scale. By collecting and dynamically analyzing the reflected light from the epi pathway at the edge of the objective, fast and precise drift correction can occur with minimal hardware additions and essentially no added cost. However, this drift correction algorithm can only be used when fluorescence is not used in the experiment – otherwise, photobleaching is extremely likely. This provides limitations of the scope of the drift correction, but it remains an effective method when using the optical trap QPD outputs as the main experimental result. Additionally, the drift correction can be improved by removing the need for LABVIEW data processing. Currently, the LABVIEW program records the intensity of each pixel in the region of interest of the CCD image specified by the user and outputs the total average intensity as the process variable of the PID controller loop. This process slows the drift correction system down to the point where it runs at a maximum of 100 Hz and is greatly dependent on processing power. This inefficiancy can be resolved using a minimally "invasive" photodiode inserted into the focal plane where the reflected light is currently collected by the CCD camera. A simple 1 mm x 1 mm photodiode can be placed on the Wollaston prism with minimal blocking of the field of view of the microscope. This photodiode could directly measure the light intensity and allow the drift correction system to operate at 500 kHz, greatly improving response to focus drift.

Finally, postprocessing improvements were made to accommodate for the greater amount of data collected by QPD-based tracking in comparison to image-based tracking. A higher sampling rate allows for a better idea of how the bead is dynamically interacting with the cell. Custom LABVIEW programs developed for this assay allow for analysis of both precise timepoints and time-averaged general trends.

Ultimately, the improvements made to this system resulted in relatively promising data as shown in Figure 22. Significant steps have been made to ensure that the variance-based bead-cell adhesion assay can be consistently reliable in the future.

4.2 Escape Force-Based Bead-Cell Adhesion Assay Discussion

The escape force-based bead-cell adhesion assay provides a more definitive outcome than the variance-based assay with regards to characterization of early adhesion membrane activity. In addition, this assay allows for the relative quantification of the forces at work in this early stage of mechanotransduction.

The underlying factor behind the determination of time to adhesion and escape force is the relationship between integrin and fibronectin. Two integrin-fibronectin binding motifs representing the time to adhesion are hypothesized. First, the measured time may represent how long it takes for the integrins in the membrane to diffuse toward the point of adhesion, with high avidity and affinity to the fibronectin at the adhesion point, essentially instantaneously binding once the integrins reach the location. Second, the time to adhesion measurement may not depend on the diffusion of proteins to the adhesion location. The thermal motion of the bead causes the ligand, the fibronectin, to constantly be in motion. Likewise, the integrins at the adhesion site are constantly diffusing, and once a fibronectin-integrin bond is formed, it can reversibly dissociate. Thus, a reaction kinetics-based rationale can be applied to the adhesion time, as detailed in the literature [58],[59].

The time to adhesion measurement is defined as the time point at which the bind strengths between the bead and the cell membrane are greater than the forces applied by the laser light to keep the bead trapped. However, the QPD bead tracking is only linear to the trap force of the laser for about 3 microns from the center of the trap. Once a bead is adhered, the bead-cell bonds pull the cell out of the optical trap, resulting in meaningless data. Therefore, the time point before that adhesion time is analyzed for maximum bead displacement from the optical trap. This value represents the maximum force at which the trap strength is greater than the bond strength. So, it can be assumed that the bond strengths observed at the time of adhesion are greater than this measured force, giving a general idea of the forces at work in membrane adhesion.

Here, we observed that the addition of benzyl alcohol, which is a known membrane fluidizer, decreases time to adhesion of the fibronectin-functionalized bead to the integrins in the endothelial cell membrane. This was expected, as a more fluid membrane allows for faster diffusion of proteins and lipids throughout the membrane. Additionally, we observed that the addition of benzyl alcohol did not noticeably affect the force of adhesion. This can be reasonably assumed that same number of integrins would need to bind to the bead in order to apply enough force to remove the bead from the trap. Therefore, the time to diffusion does not affect the force of adhesion with regards to these bead-cell assays.

The control experiments, in which non-functionalized beads were brought into contact with unaltered endothelial cell membranes, resulted in extremely high times to adhesion and low escape forces. In many cases, the beads did not adhere after 60 seconds, which was the maximal time allotted for these experiments. The low adhesion forces can be explained in terms of non-specific binding. The method for calculating the minimum escape force assumes a steady increase of integrin-fibronectin bonds that is proportional to the binding force. Then, once the minimum escape force threshold is reached, the bead is displaced from the trap. However, the control experiments seemed to adhere at random times; there was no steady increase in force leading up to the adhesion time. Therefore, it can be assumed that nonspecific binding is responsible for the bead adhesion in the control experiments.

We also observed that adhesion sites at the leading edge of cells had shorter time to adhesion and greater adhesion force in comparison to the trailing edge. These results suggest that integrin is more available in the membranes in the leading edge of cells, as shown previously [60].

These results can be presented in the framework of a computational model developed by Hammer *et al* to study integrin adhesion and clustering in response to mechanical membrane bending, as caused by the ECM [61]. The developed model combines the distance-dependent adhesion dynamics between integrins and their ECM ligands and the forces applied by the glycocalyx, which is the network of polysaccharides and proteins that line some epithelial cells, to repel the membrane and the ECM. This model showed that membrane bending had a significant affect on the rate of integrin adhesion and integrin clustering. Essentially, as integrins bind to the ECM, causing the membrane to deform, more integrins are moved closer to the binding site, allowing for faster rate of adhesion. The model found that integrin clustering and integrin-ligand interactions depended strongly on the mechanical properties of both the cell and the glycocalyx. Additionally, the study found that integrin binding can be approximated with a sigmoidal curve, as shown in Figure 30. Essentially, this model shows that although initial integrin binding may take tens of seconds, once an integrin is bound, it is able to recruit more integrins at a more rapid rate. This phenomenon can be described by membrane bending: as an integrin binds to fibronectin, the membrane bends, causing more free integrins to become closer in proximity to fibronectin ligands, increasing the effective association constant of the binding reaction.

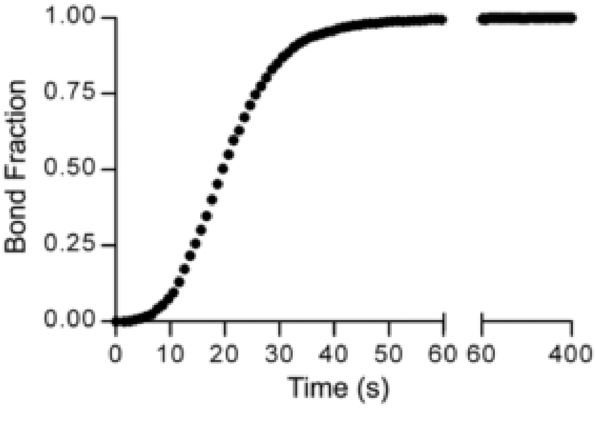

Figure 30: Plot showing the integrin binding dynamics in the computational model developed by Hammer *et al* [61].

The escape force-based bead-cell adhesion assay developed could potentially validate these assertions made by Hammer *et al*. Integrin clustering and adhesion can be measured by the adhesion force assay detailed in this thesis. Because the adhesion force is proportional to the number of integrin-fibronectin bonds, the binding kinetics can be measured. Fluorescently-labeled integrins could allow for tracking of integrin clustering and density. Studying the effect of membrane stiffness (and thus membrane bending) on integrin function and clustering would help to further understand the role of the membrane in focal adhesion formation.

Chapter 5

CONCLUSIONS AND FUTURE DIRECTIONS

The results presented in this thesis have demonstrated the efficacy of using an optical trap to study the membrane forces in early focal adhesion induction. The variance-based bead-cell adhesion assay was improved through automation by the development of a number of LABVIEW programs, increasing the accuracy and consistency of data collected. Additionally, the escape force-based bead-cell was developed to provide a more definitive approach to quantifying the early adhesion dynamics. Preliminary results suggest that the addition of benzyl alcohol to cell membranes causes a decrease in time of adhesion, but no change in adhesion force. Also, these results suggest that the assays conducted on the leading edge of cells show a shorter time of adhesion and a greater adhesion force in comparison to the trailing edge.

Future studies with the escape force-based bead-cell adhesion assay can be employed to further investigate the binding processes that affect the time to adhesion. For example, the assay can be combined with analysis of fluorescent-labeled focal adhesion proteins such as focal adhesion kinase (FAK) or talin in order confirm the evidence of integrin clustering and binding that is suggested by the adhesion force measurements. Then, a relationship between time to adhesion/adhesion force and focal adhesion size/focal adhesion formation rate can be attained. Additionally, more membrane modifying agents can be applied to study the relationship between membrane fluidity and focal adhesion activity, such as Vitamin E or cholesterol. Finally, the focus drift correction algorithm can be improved by adding a small photodiode to collect the reflected light instead of the CCD camera. This photodiode would cut down on processing time required, increasing the speed of the drift correction algorithm to allow for more precise data collection.

Appendix A

COMSOL Images

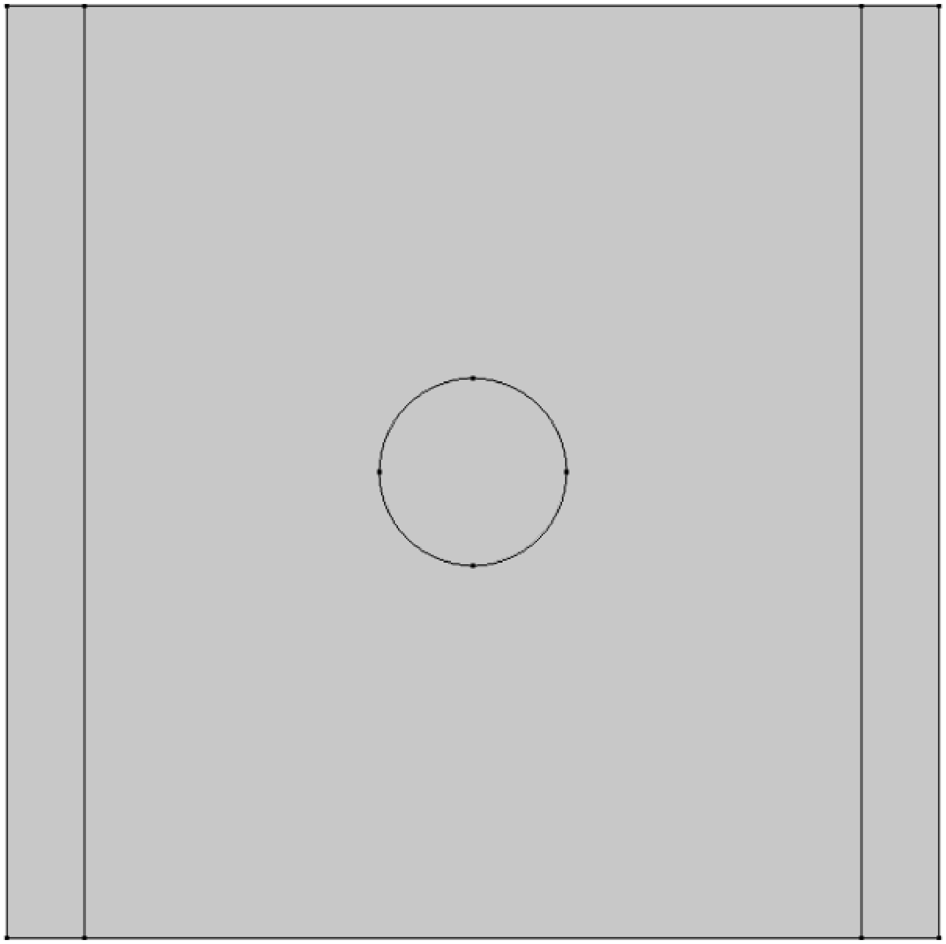

Figure 31: The geometry used in the models was a rectangle of width 20 µm and height 40 µm with a 5 µm-thick perfectly matched layer surrounding the exterior. The rectangle was given the material properties of water (refractive index n=1.33). A 1 µm circle was created at the center of the rectangle to simulate the bead and given the material properties of polysilicon (n=1.6).

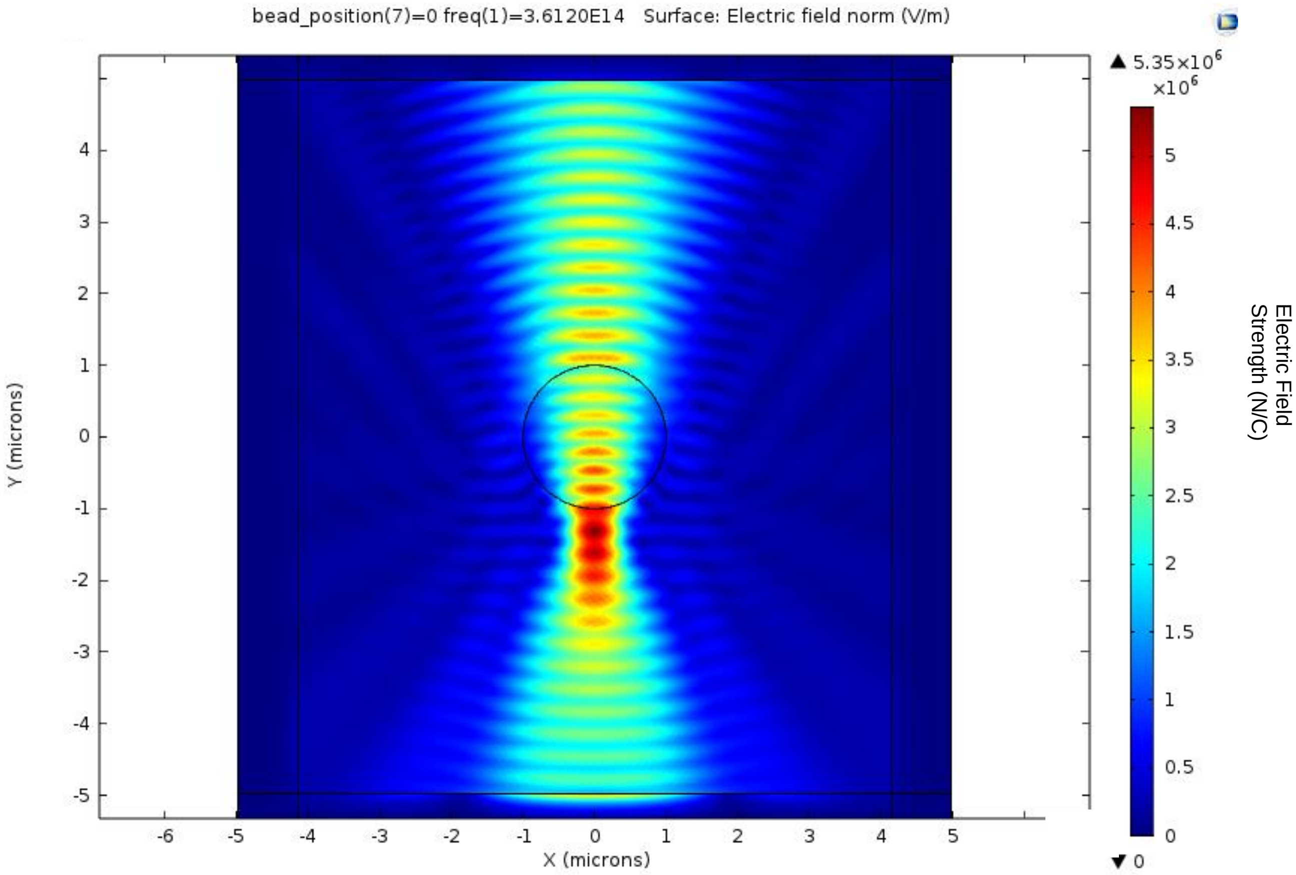

Figure 32: The electromagnetic waves module was used to generate a 2-dimensional background electric field focused on a 2 µm polystyrene bead submerged in water.

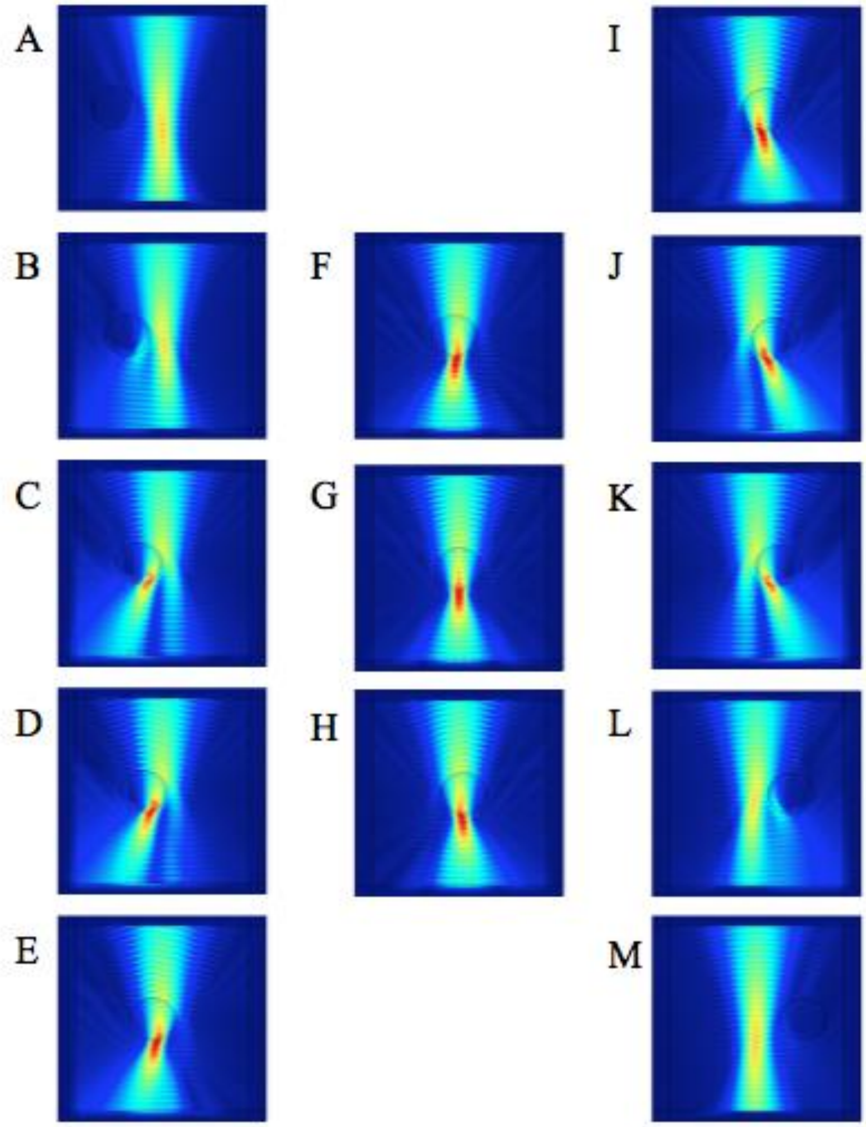

Figure 33: Electric field strength of the optical trap at varying bead (D = 2 µm) positions. The heat map color scale ranges from 1 (blue) to 10 (red). The red arrows indicate the magnitude of the restoring force applied on the bead by the laser. The bead positions from the center of the trap are (A) -1.2 µm, (B) -1 µm, (C) -8 µm, (D) -0.6 µm, (E) -0.4 µm, (F) -0.2 µm, (G) 0 µm, (H) 0.2 µm, (I) 0.4 µm, (J) 0.6 µm, (K) 0.8 µm, (L) 1 µm, and (M) 1.2 µm.

Appendix B

LABVIEW Programs

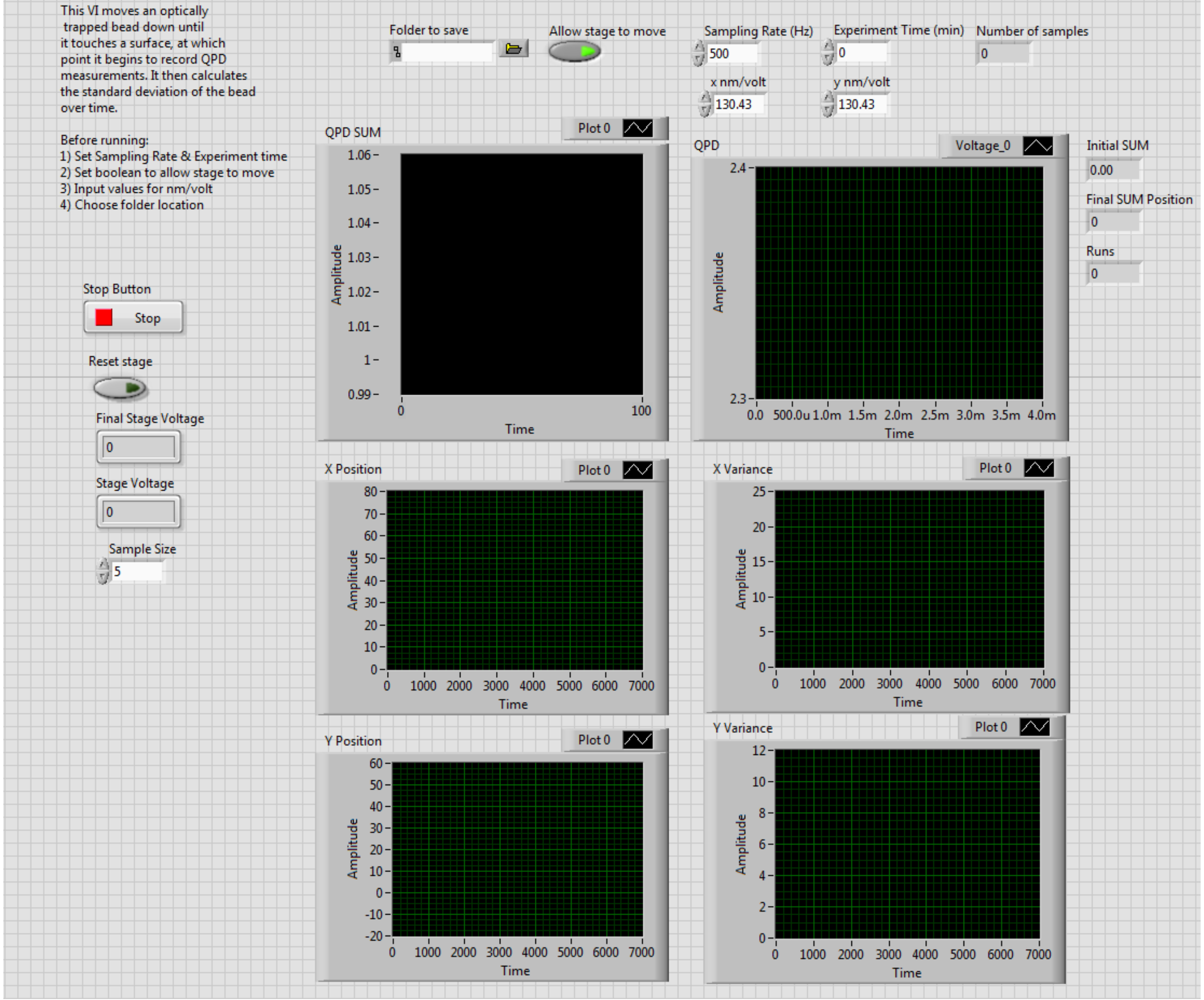

This VI moves an optically trapped bead down until it touches a surface, at which point it begins to record QPD measurements. It then calculates the standard deviation of the bead over time.

Before running:
1) Set Sampling Rate & Experiment time
2) Set boolean to allow stage to move
3) Input values for nm/volt
4) Choose folder location

Folder to save:
Sampling Rate (Hz): 500
Experiment Time (min): 0
Number of samples: 0
x nm/volt: 130.43
y nm/volt: 130.43
Initial SUM: 0.00
Final SUM Position: 0
Runs: 0
Final Stage Voltage: 0
Stage Voltage: 0
Sample Size: 5

Figure 34: LABVIEW front panel for the program developed to automate the Variance-Based Bead-Cell Adhesion Assay. The user inputs sampling rate, experiment time, and nanometer/volt calibration factors. QPD data is recorded as the bead is in contact with the cell. The data is then converted to normalized position and variance measures.

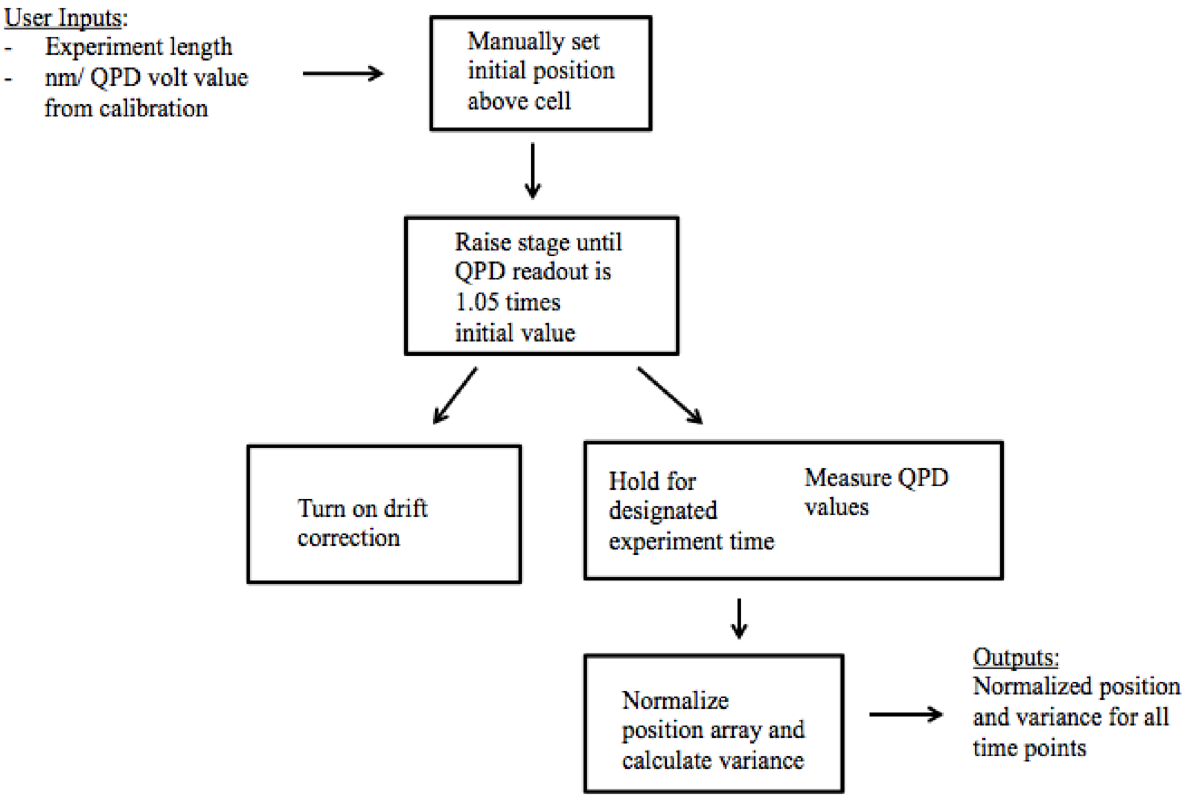

Figure 35: Flow chart representing the LABVIEW for the program developed to automate the Variance-Based Bead-Cell Adhesion Assay. The user inputs sampling rate, experiment time, and nanometer/volt calibration factors. QPD data is recorded as the bead is in contact with the cell. The data is then converted to normalized position and variance measures.

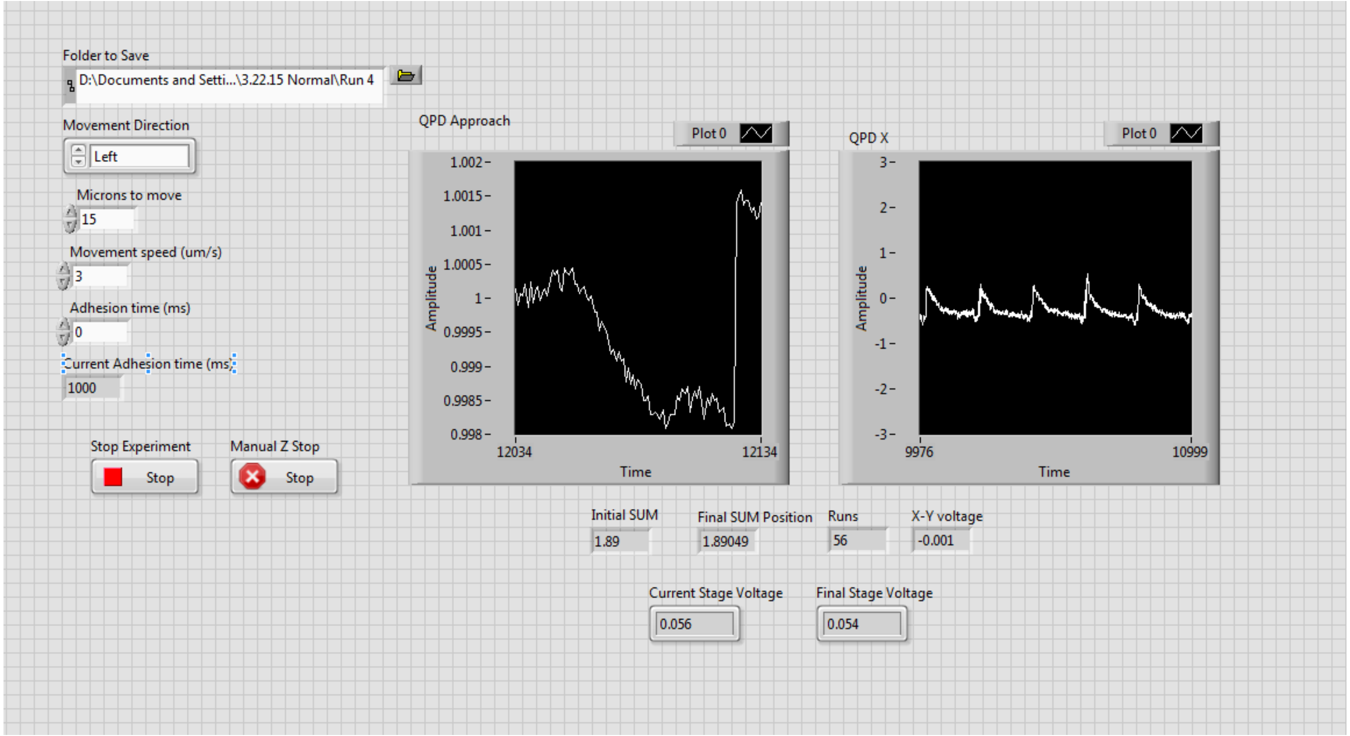

Folder to Save: D:\Documents and Setti...\3.22.15 Normal\Run 4

Movement Direction: Left

Microns to move: 15

Movement speed (um/s): 3

Adhesion time (ms): 0

Current Adhesion time (ms): 1000

Initial SUM: 1.89

Final SUM Position: 1.89049

Runs: 56

X-Y voltage: -0.001

Current Stage Voltage: 0.056

Final Stage Voltage: 0.054

Figure 36: LABVIEW front panel for the program developed to automate the Escape Force-Based Bead-Cell Adhesion Assay. The user inputs movement direction, movement speed, and initial adhesion time. The program outputs QPD data for each run as a bead is pulled away from the cell. The program is manually stopped by the user when a bead has adhered.

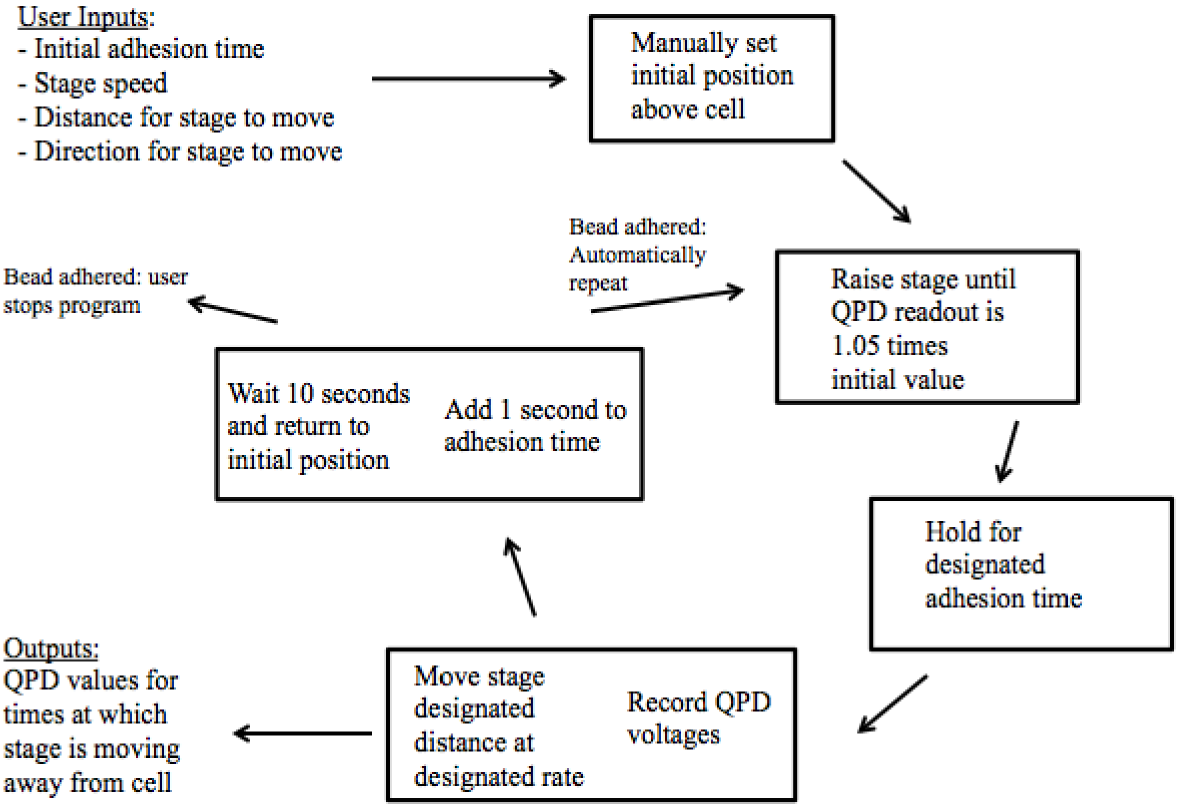

Figure 37: Flow chart representing the LABVIEW program developed to automate the Escape Force-Based Bead-Cell Adhesion Assay. The user inputs movement direction, movement speed, and initial adhesion time. The program outputs QPD data for each run as a bead is pulled away from the cell. The program is manually stopped by the user when a bead has adhered.

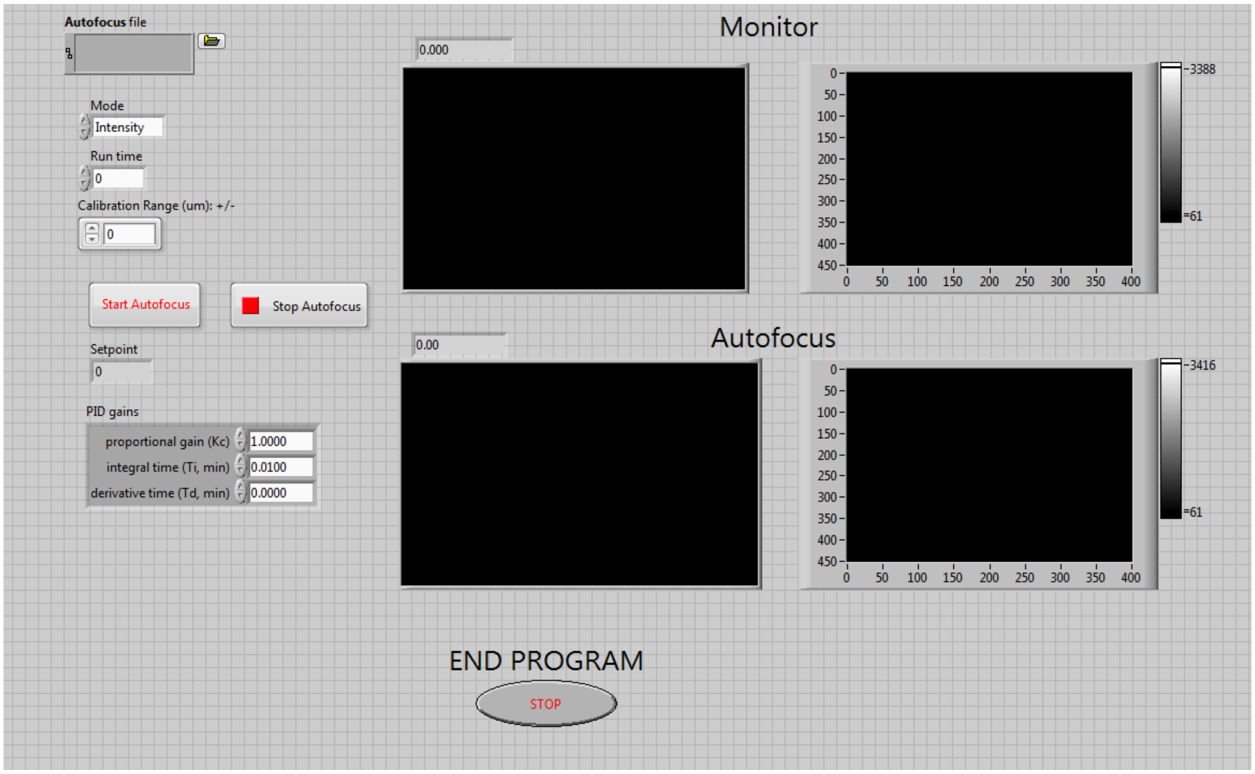

Mode: Intensity

Run time: 0

Calibration Range (um): +/- 0

Setpoint: 0

PID gains

proportional gain (Kc) 1.0000

integral time (Ti, min) 0.0100

derivative time (Td, min) 0.0000

0.000

0.00

Figure 38: LABVIEW front panel for the program developed to correct for thermal focus drift. The user inputs PID gains and the region of interest of the CCD camera.

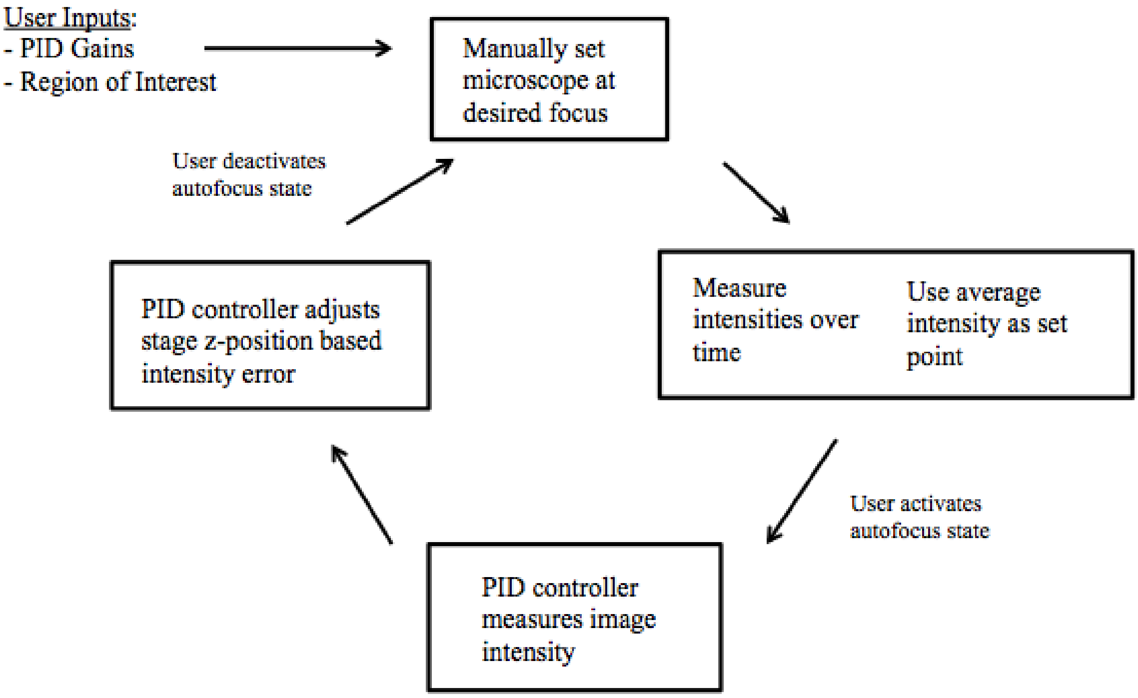

Figure 39: LABVIEW front panel for the program developed to correct for thermal focus drift. The user inputs PID gains and the region of interest of the CCD camera.

Appendix C

Supplementary Variance-Based Bead-Cell Adhesion Assay Results

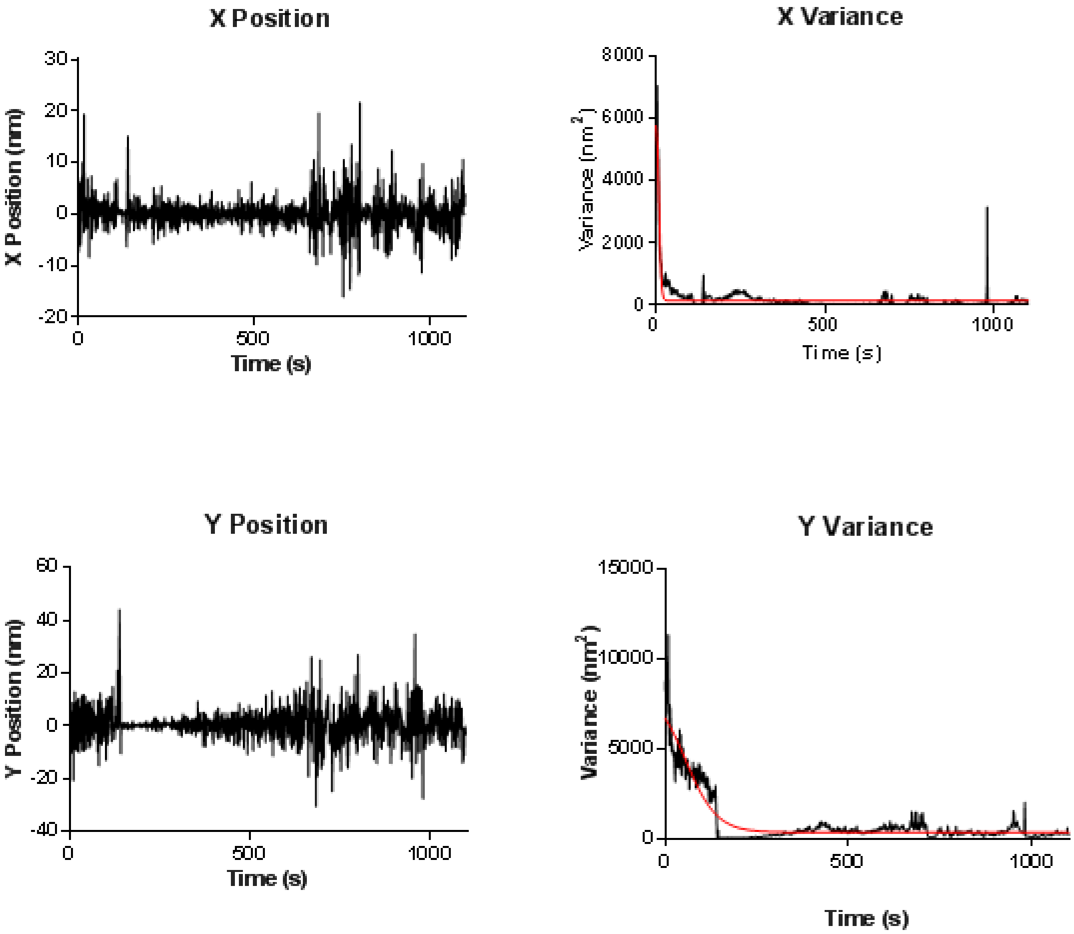

Figure 40: Characteristic time of adhesion of a fibronectin-functionalized 2 µm bead to a human aortic endothelial cell. A sigmoidal dose-response curve with variable fit was applied to the variance data to define the time of adhesion. Neither the x- nor y-direction variance converged when fit with the curve.

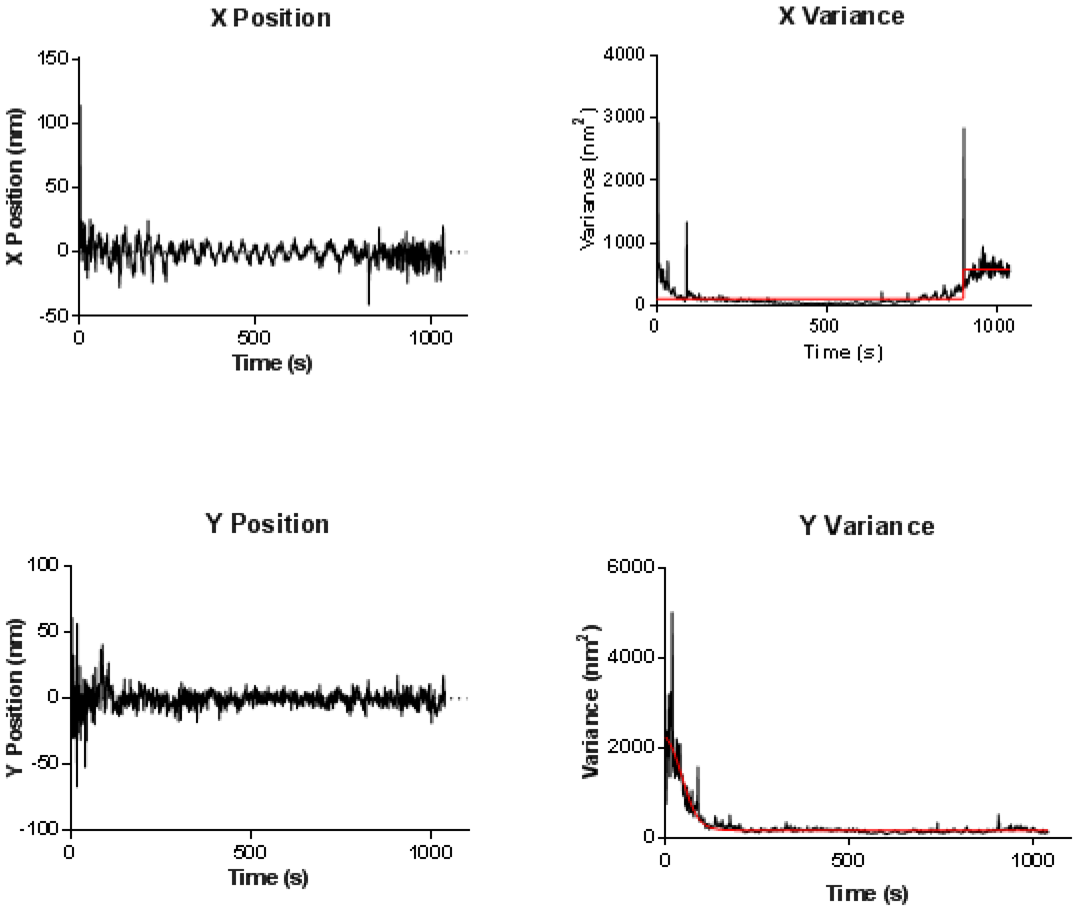

Figure 41: Characteristic time of adhesion of a fibronectin-functionalized 2 µm bead to a human aortic endothelial cell. A sigmoidal dose-response curve with variable fit was applied to the variance data to define the time of adhesion. Neither the x- nor y-direction variance converged when fit with the curve.

Appendix D

Statistics for Adhesion Force-Based Bead-Cell Assays

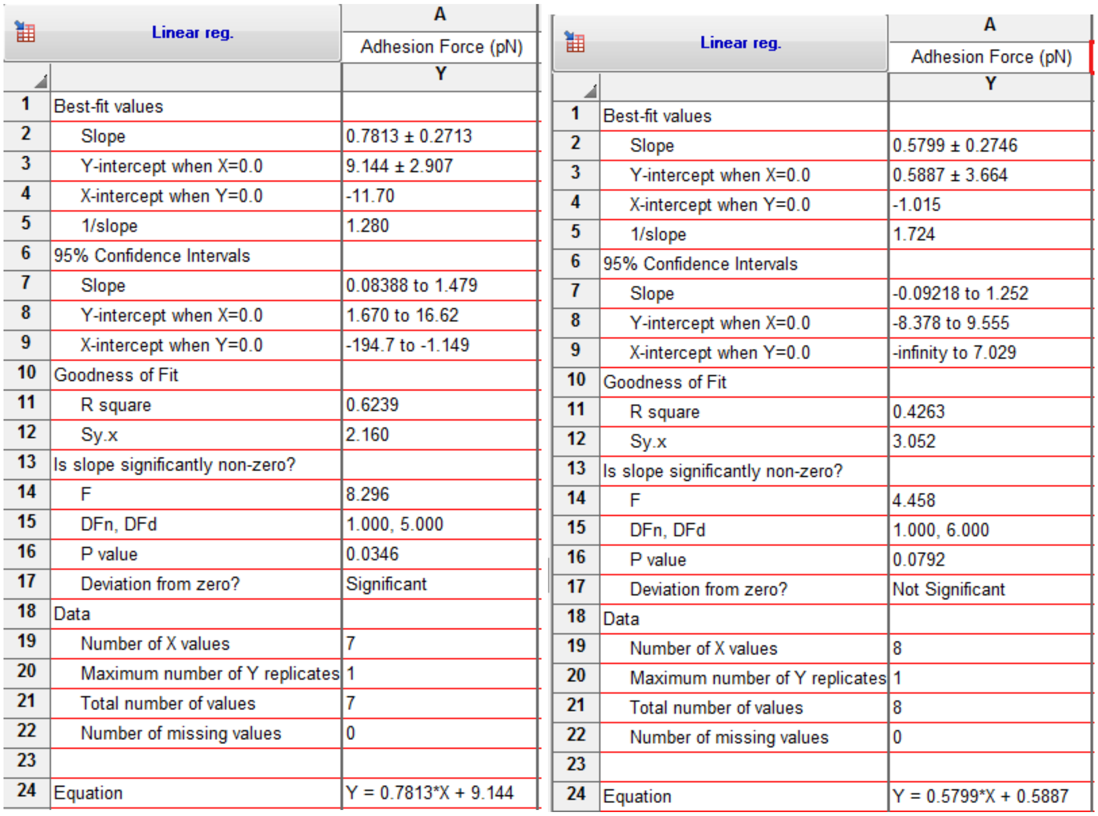

	Linear reg.	A Adhesion Force (pN) Y
1	Best-fit values	
2	Slope	0.7813 ± 0.2713
3	Y-intercept when X=0.0	9.144 ± 2.907
4	X-intercept when Y=0.0	-11.70
5	1/slope	1.280
6	95% Confidence Intervals	
7	Slope	0.08388 to 1.479
8	Y-intercept when X=0.0	1.670 to 16.62
9	X-intercept when Y=0.0	-194.7 to -1.149
10	Goodness of Fit	
11	R square	0.6239
12	Sy.x	2.160
13	Is slope significantly non-zero?	
14	F	8.296
15	DFn, DFd	1.000, 5.000
16	P value	0.0346
17	Deviation from zero?	Significant
18	Data	
19	Number of X values	7
20	Maximum number of Y replicates	1
21	Total number of values	7
22	Number of missing values	0
23		
24	Equation	Y = 0.7813*X + 9.144

	Linear reg.	A Adhesion Force (pN) Y
1	Best-fit values	
2	Slope	0.5799 ± 0.2746
3	Y-intercept when X=0.0	0.5887 ± 3.664
4	X-intercept when Y=0.0	-1.015
5	1/slope	1.724
6	95% Confidence Intervals	
7	Slope	-0.09218 to 1.252
8	Y-intercept when X=0.0	-8.378 to 9.555
9	X-intercept when Y=0.0	-infinity to 7.029
10	Goodness of Fit	
11	R square	0.4263
12	Sy.x	3.052
13	Is slope significantly non-zero?	
14	F	4.458
15	DFn, DFd	1.000, 6.000
16	P value	0.0792
17	Deviation from zero?	Not Significant
18	Data	
19	Number of X values	8
20	Maximum number of Y replicates	1
21	Total number of values	8
22	Number of missing values	0
23		
24	Equation	Y = 0.5799*X + 0.5887

Figure 42: Linear regression for adhesion force vs. time to adhesion for the leading and trailing edges of endothelial cells with unaltered membranes.

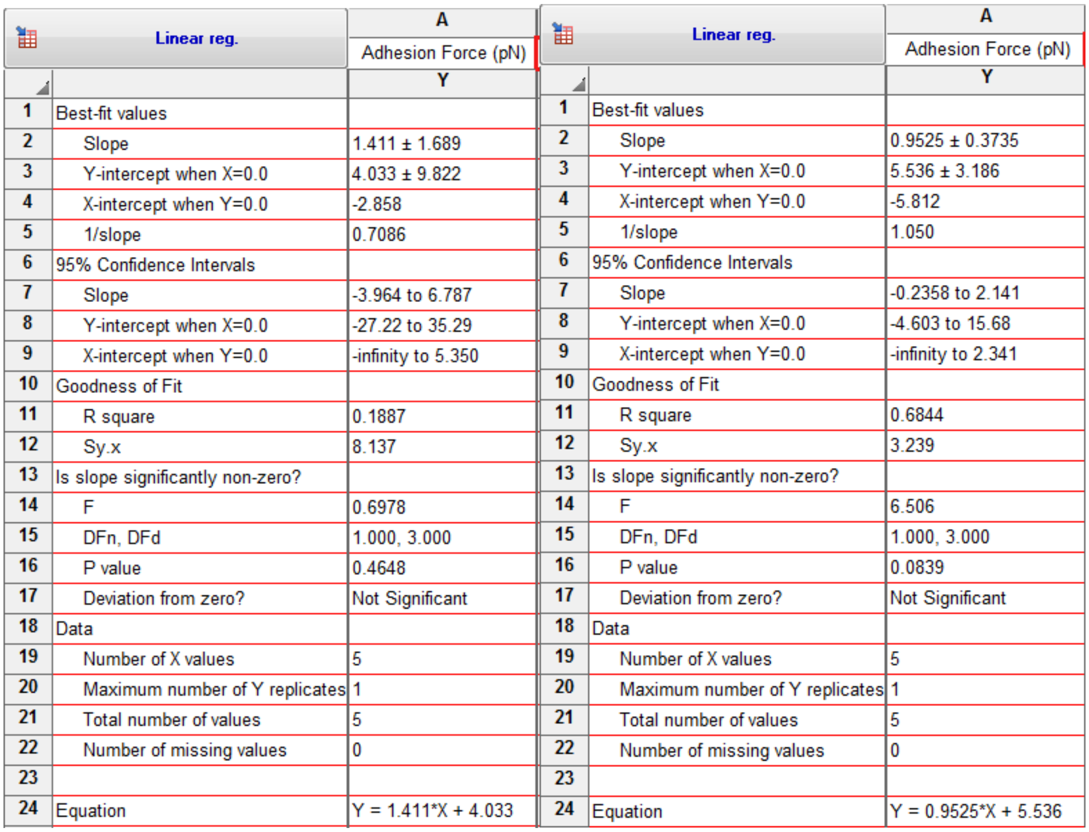

	Linear reg.	A Adhesion Force (pN)
		Y
1	Best-fit values	
2	Slope	1.411 ± 1.689
3	Y-intercept when X=0.0	4.033 ± 9.822
4	X-intercept when Y=0.0	-2.858
5	1/slope	0.7086
6	95% Confidence Intervals	
7	Slope	-3.964 to 6.787
8	Y-intercept when X=0.0	-27.22 to 35.29
9	X-intercept when Y=0.0	-infinity to 5.350
10	Goodness of Fit	
11	R square	0.1887
12	Sy.x	8.137
13	Is slope significantly non-zero?	
14	F	0.6978
15	DFn, DFd	1.000, 3.000
16	P value	0.4648
17	Deviation from zero?	Not Significant
18	Data	
19	Number of X values	5
20	Maximum number of Y replicates	1
21	Total number of values	5
22	Number of missing values	0
23		
24	Equation	Y = 1.411*X + 4.033

	Linear reg.	A Adhesion Force (pN)
		Y
1	Best-fit values	
2	Slope	0.9525 ± 0.3735
3	Y-intercept when X=0.0	5.536 ± 3.186
4	X-intercept when Y=0.0	-5.812
5	1/slope	1.050
6	95% Confidence Intervals	
7	Slope	-0.2358 to 2.141
8	Y-intercept when X=0.0	-4.603 to 15.68
9	X-intercept when Y=0.0	-infinity to 2.341
10	Goodness of Fit	
11	R square	0.6844
12	Sy.x	3.239
13	Is slope significantly non-zero?	
14	F	6.506
15	DFn, DFd	1.000, 3.000
16	P value	0.0839
17	Deviation from zero?	Not Significant
18	Data	
19	Number of X values	5
20	Maximum number of Y replicates	1
21	Total number of values	5
22	Number of missing values	0
23		
24	Equation	Y = 0.9525*X + 5.536

Figure 43: Linear regression for adhesion force vs. time to adhesion for the leading and trailing edges of BA-treated endothelial cells.

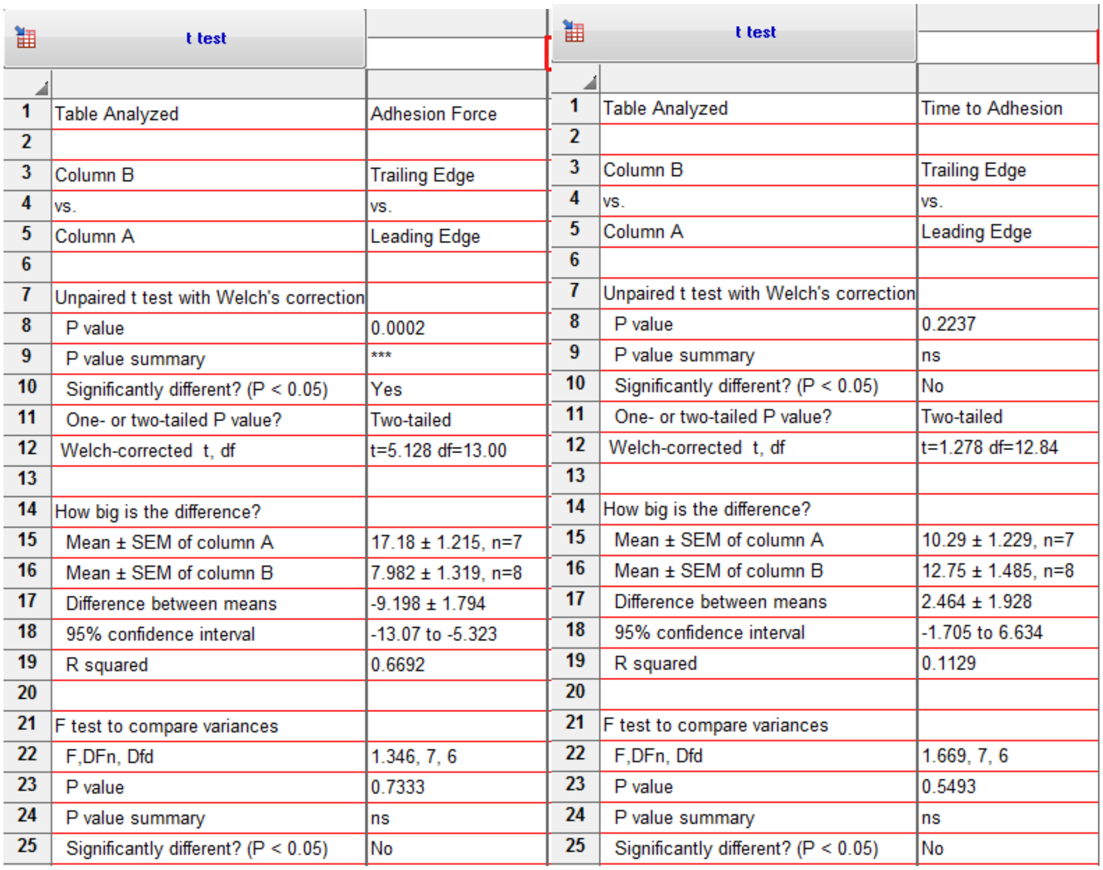

	t test	
1	Table Analyzed	Adhesion Force
2		
3	Column B	Trailing Edge
4	vs.	vs.
5	Column A	Leading Edge
6		
7	Unpaired t test with Welch's correction	
8	P value	0.0002
9	P value summary	***
10	Significantly different? (P < 0.05)	Yes
11	One- or two-tailed P value?	Two-tailed
12	Welch-corrected t, df	t=5.128 df=13.00
13		
14	How big is the difference?	
15	Mean ± SEM of column A	17.18 ± 1.215, n=7
16	Mean ± SEM of column B	7.982 ± 1.319, n=8
17	Difference between means	-9.198 ± 1.794
18	95% confidence interval	-13.07 to -5.323
19	R squared	0.6692
20		
21	F test to compare variances	
22	F,DFn, Dfd	1.346, 7, 6
23	P value	0.7333
24	P value summary	ns
25	Significantly different? (P < 0.05)	No

	t test	
1	Table Analyzed	Time to Adhesion
2		
3	Column B	Trailing Edge
4	vs.	vs.
5	Column A	Leading Edge
6		
7	Unpaired t test with Welch's correction	
8	P value	0.2237
9	P value summary	ns
10	Significantly different? (P < 0.05)	No
11	One- or two-tailed P value?	Two-tailed
12	Welch-corrected t, df	t=1.278 df=12.84
13		
14	How big is the difference?	
15	Mean ± SEM of column A	10.29 ± 1.229, n=7
16	Mean ± SEM of column B	12.75 ± 1.485, n=8
17	Difference between means	2.464 ± 1.928
18	95% confidence interval	-1.705 to 6.634
19	R squared	0.1129
20		
21	F test to compare variances	
22	F,DFn, Dfd	1.669, 7, 6
23	P value	0.5493
24	P value summary	ns
25	Significantly different? (P < 0.05)	No

Figure 44: Unpaired t-test for adhesion force and time to adhesion for endothelial cells with unaltered cell membranes.

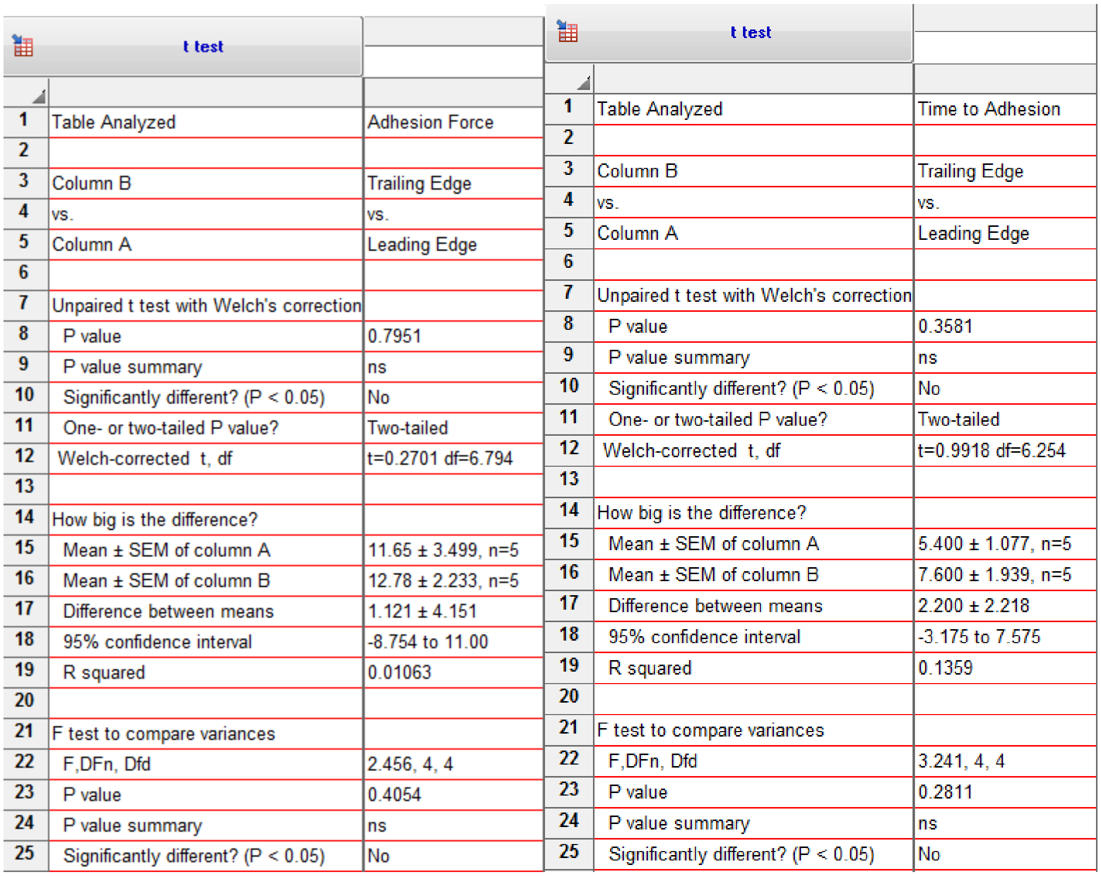

	t test	
1	Table Analyzed	Adhesion Force
2		
3	Column B	Trailing Edge
4	vs.	vs.
5	Column A	Leading Edge
6		
7	Unpaired t test with Welch's correction	
8	P value	0.7951
9	P value summary	ns
10	Significantly different? (P < 0.05)	No
11	One- or two-tailed P value?	Two-tailed
12	Welch-corrected t, df	t=0.2701 df=6.794
13		
14	How big is the difference?	
15	Mean ± SEM of column A	11.65 ± 3.499, n=5
16	Mean ± SEM of column B	12.78 ± 2.233, n=5
17	Difference between means	1.121 ± 4.151
18	95% confidence interval	-8.754 to 11.00
19	R squared	0.01063
20		
21	F test to compare variances	
22	F,DFn, Dfd	2.456, 4, 4
23	P value	0.4054
24	P value summary	ns
25	Significantly different? (P < 0.05)	No

	t test	
1	Table Analyzed	Time to Adhesion
2		
3	Column B	Trailing Edge
4	vs.	vs.
5	Column A	Leading Edge
6		
7	Unpaired t test with Welch's correction	
8	P value	0.3581
9	P value summary	ns
10	Significantly different? (P < 0.05)	No
11	One- or two-tailed P value?	Two-tailed
12	Welch-corrected t, df	t=0.9918 df=6.254
13		
14	How big is the difference?	
15	Mean ± SEM of column A	5.400 ± 1.077, n=5
16	Mean ± SEM of column B	7.600 ± 1.939, n=5
17	Difference between means	2.200 ± 2.218
18	95% confidence interval	-3.175 to 7.575
19	R squared	0.1359
20		
21	F test to compare variances	
22	F,DFn, Dfd	3.241, 4, 4
23	P value	0.2811
24	P value summary	ns
25	Significantly different? (P < 0.05)	No

Figure 45: Unpaired t-test for adhesion force and time to adhesion for endothelial cells treated with benzyl alcohol.

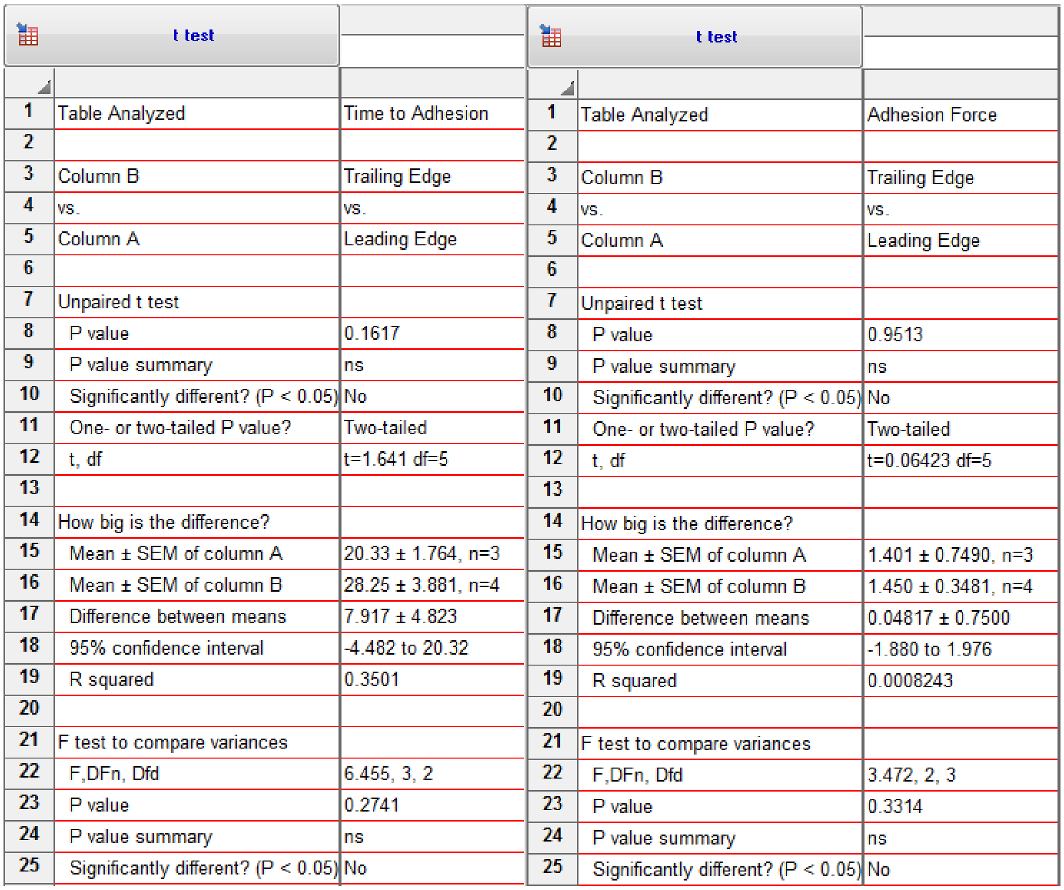

	t test	
1	Table Analyzed	Time to Adhesion
2		
3	Column B	Trailing Edge
4	vs.	vs.
5	Column A	Leading Edge
6		
7	Unpaired t test	
8	P value	0.1617
9	P value summary	ns
10	Significantly different? (P < 0.05)	No
11	One- or two-tailed P value?	Two-tailed
12	t, df	t=1.641 df=5
13		
14	How big is the difference?	
15	Mean ± SEM of column A	20.33 ± 1.764, n=3
16	Mean ± SEM of column B	28.25 ± 3.881, n=4
17	Difference between means	7.917 ± 4.823
18	95% confidence interval	-4.482 to 20.32
19	R squared	0.3501
20		
21	F test to compare variances	
22	F,DFn, Dfd	6.455, 3, 2
23	P value	0.2741
24	P value summary	ns
25	Significantly different? (P < 0.05)	No

	t test	
1	Table Analyzed	Adhesion Force
2		
3	Column B	Trailing Edge
4	vs.	vs.
5	Column A	Leading Edge
6		
7	Unpaired t test	
8	P value	0.9513
9	P value summary	ns
10	Significantly different? (P < 0.05)	No
11	One- or two-tailed P value?	Two-tailed
12	t, df	t=0.06423 df=5
13		
14	How big is the difference?	
15	Mean ± SEM of column A	1.401 ± 0.7490, n=3
16	Mean ± SEM of column B	1.450 ± 0.3481, n=4
17	Difference between means	0.04817 ± 0.7500
18	95% confidence interval	-1.880 to 1.976
19	R squared	0.0008243
20		
21	F test to compare variances	
22	F,DFn, Dfd	3.472, 2, 3
23	P value	0.3314
24	P value summary	ns
25	Significantly different? (P < 0.05)	No

Figure 46: Unpaired t-test for adhesion force and time to adhesion for control endothelial cells with non-functionalized beads.

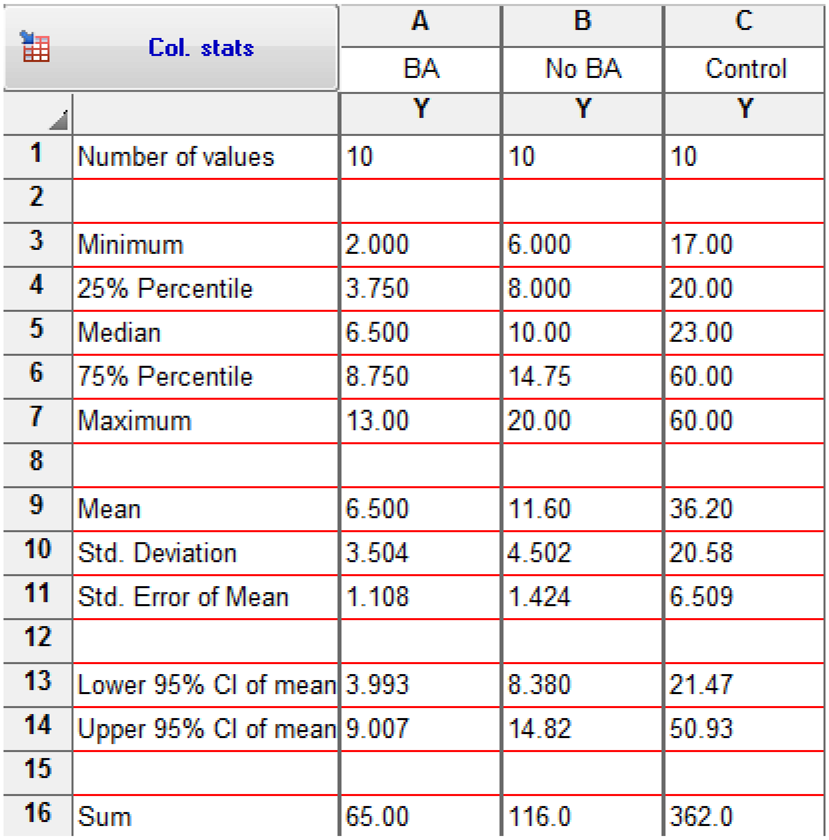

	Col. stats	A	B	C
		BA	No BA	Control
		Y	Y	Y
1	Number of values	10	10	10
2				
3	Minimum	2.000	6.000	17.00
4	25% Percentile	3.750	8.000	20.00
5	Median	6.500	10.00	23.00
6	75% Percentile	8.750	14.75	60.00
7	Maximum	13.00	20.00	60.00
8				
9	Mean	6.500	11.60	36.20
10	Std. Deviation	3.504	4.502	20.58
11	Std. Error of Mean	1.108	1.424	6.509
12				
13	Lower 95% CI of mean	3.993	8.380	21.47
14	Upper 95% CI of mean	9.007	14.82	50.93
15				
16	Sum	65.00	116.0	362.0

Figure 47: Column statistics for all values for time to adhesion.

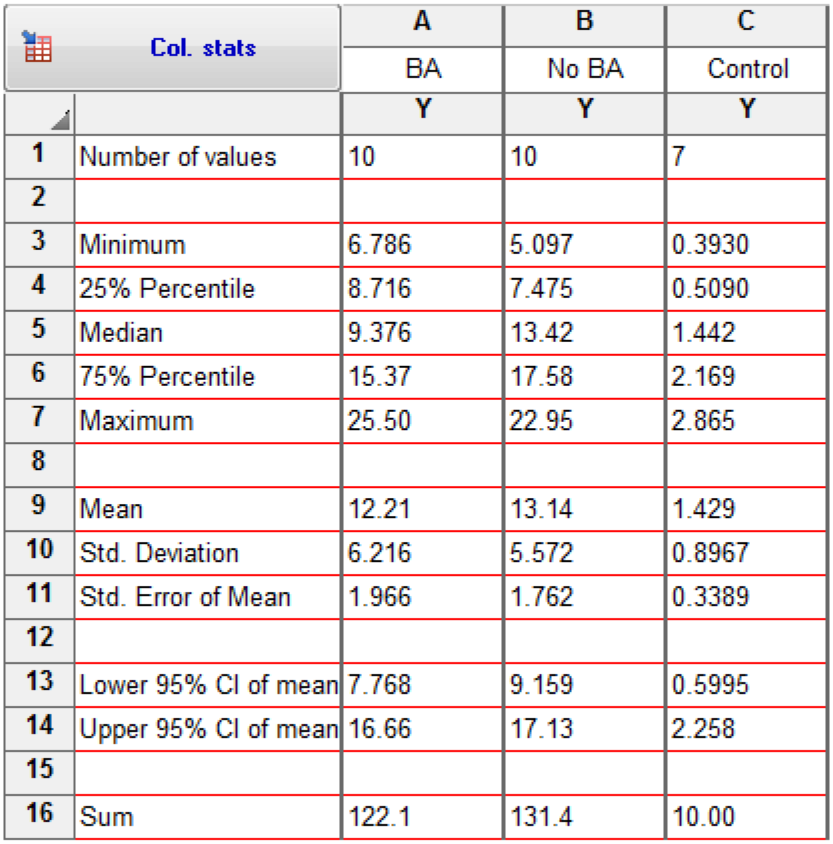

Col. stats		A	B	C
		BA	No BA	Control
		Y	Y	Y
1	Number of values	10	10	7
2				
3	Minimum	6.786	5.097	0.3930
4	25% Percentile	8.716	7.475	0.5090
5	Median	9.376	13.42	1.442
6	75% Percentile	15.37	17.58	2.169
7	Maximum	25.50	22.95	2.865
8				
9	Mean	12.21	13.14	1.429
10	Std. Deviation	6.216	5.572	0.8967
11	Std. Error of Mean	1.966	1.762	0.3389
12				
13	Lower 95% CI of mean	7.768	9.159	0.5995
14	Upper 95% CI of mean	16.66	17.13	2.258
15				
16	Sum	122.1	131.4	10.00

Figure 48: Column statistics for all values for adhesion force.

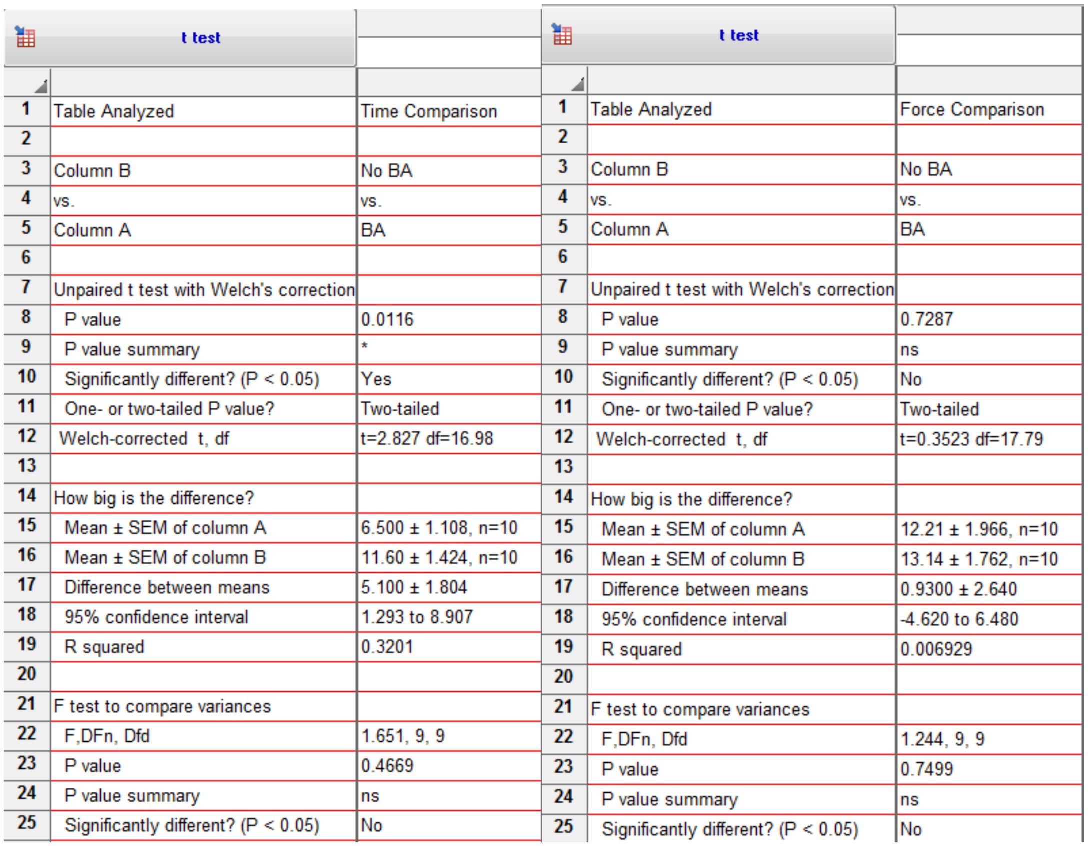

	t test	
1	Table Analyzed	Time Comparison
2		
3	Column B	No BA
4	vs.	vs.
5	Column A	BA
6		
7	Unpaired t test with Welch's correction	
8	P value	0.0116
9	P value summary	*
10	Significantly different? (P < 0.05)	Yes
11	One- or two-tailed P value?	Two-tailed
12	Welch-corrected t, df	t=2.827 df=16.98
13		
14	How big is the difference?	
15	Mean ± SEM of column A	6.500 ± 1.108, n=10
16	Mean ± SEM of column B	11.60 ± 1.424, n=10
17	Difference between means	5.100 ± 1.804
18	95% confidence interval	1.293 to 8.907
19	R squared	0.3201
20		
21	F test to compare variances	
22	F,DFn, Dfd	1.651, 9, 9
23	P value	0.4669
24	P value summary	ns
25	Significantly different? (P < 0.05)	No

	t test	
1	Table Analyzed	Force Comparison
2		
3	Column B	No BA
4	vs.	vs.
5	Column A	BA
6		
7	Unpaired t test with Welch's correction	
8	P value	0.7287
9	P value summary	ns
10	Significantly different? (P < 0.05)	No
11	One- or two-tailed P value?	Two-tailed
12	Welch-corrected t, df	t=0.3523 df=17.79
13		
14	How big is the difference?	
15	Mean ± SEM of column A	12.21 ± 1.966, n=10
16	Mean ± SEM of column B	13.14 ± 1.762, n=10
17	Difference between means	0.9300 ± 2.640
18	95% confidence interval	-4.620 to 6.480
19	R squared	0.006929
20		
21	F test to compare variances	
22	F,DFn, Dfd	1.244, 9, 9
23	P value	0.7499
24	P value summary	ns
25	Significantly different? (P < 0.05)	No

Figure 49: Unpaired t-test for adhesion force and time to adhesion for BA-treated cells vs non-treated cells.

BIBLIOGRAPHY

[1] J. Deanfield, A. Donald, C. Ferri, C. Giannattasio, J. Halcox, S. Halligan, A. Lerman, G. Mancia, J. J. Oliver, A. C. Pessina, D. Rizzoni, G. P. Rossi, A. Salvetti, E. L. Schiffrin, S. Taddei, and D. J. Webb, "Endothelial function and dysfunction. Part I: Methodological issues for assessment in the different vascular beds: a statement by the Working Group on Endothelin and Endothelial Factors of the European Society of Hypertension," *J. Hypertens.*, vol. 23, no. 1, pp. 7–17, Jan. 2005.

[2] S. Jalali and M. del Pozo, "Integrin-mediated mechanotransduction requires its dynamic interaction with specific extracellular matrix (ECM) ligands," *Proc. Natl. Acad. Sci.*, vol. 98, no. 25, 2001.

[3] M. D. Frame, R. J. Rivers, O. Altland, and S. Cameron, "Mechanisms initiating integrin-stimulated flow recruitment in arteriolar networks," vol. 8181, pp. 2279–2287, 2007.

[4] Y. Zhou and J. F. Hancock, "Ras nanoclusters: Versatile lipid-based signaling platforms," *Biochim. Biophys. Acta - Mol. Cell Res.*, vol. 1853, no. 4, pp. 841–849, 2015.

[5] Z. Li, B. Anvari, M. Takashima, P. Brecht, J. H. Torres, and W. E. Brownell, "Membrane tether formation from outer hair cells with optical tweezers.," *Biophys. J.*, vol. 82, no. 3, pp. 1386–95, Mar. 2002.

[6] S. Weinbaum, X. Zhang, Y. Han, H. Vink, and S. C. Cowin, "Mechanotransduction and flow across the endothelial glycocalyx," *Proc. Natl. Acad. Sci. U. S. A.*, vol. 100, no. 13, pp. 7988–95, Jun. 2003.

[7] F. J. Alenghat and D. E. Ingber, "Mechanotransduction: all signals point to cytoskeleton, matrix, and integrins," *Sci. STKE*, vol. 2002, no. 119, p. pe6, Feb. 2002.

[8] S. Huang, C. S. Chen, and D. E. Ingber, "Control of cyclin D1, p27(Kip1), and cell cycle progression in human capillary endothelial cells by cell shape and cytoskeletal tension," *Mol. Biol. Cell*, vol. 9, no. 11, pp. 3179–93, Nov. 1998.

[9] N. J. Anthis, K. L. Wegener, F. Ye, C. Kim, B. T. Goult, E. D. Lowe, I. Vakonakis, N. Bate, D. R. Critchley, M. H. Ginsberg, and I. D. Campbell, "The structure of an integrin/talin complex reveals the basis of inside-out signal transduction," *EMBO J.*, vol. 28, no. 22, pp. 3623–32, Nov. 2009.

[10] O. Rossier, V. Octeau, J.-B. Sibarita, C. Leduc, B. Tessier, D. Nair, V. Gatterdam, O. Destaing, C. Albigès-Rizo, R. Tampé, L. Cognet, D. Choquet, B. Lounis, and G. Giannone, "Integrins β1 and β3 exhibit distinct dynamic nanoscale organizations inside focal adhesions.," *Nat. Cell Biol.*, vol. 14, no. 10, pp. 1057–67, Oct. 2012.

[11] J. Ivaska, “Unanchoring integrins in focal adhesions,” *Nat. Cell Biol.*, vol. 14, no. 10, pp. 981–3, Oct. 2012.

[12] S. Jalali, M. a del Pozo, K. Chen, H. Miao, Y. Li, M. a Schwartz, J. Y. Shyy, and S. Chien, “Integrin-mediated mechanotransduction requires its dynamic interaction with specific extracellular matrix (ECM) ligands.,” *Proc. Natl. Acad. Sci. U. S. A.*, vol. 98, no. 3, pp. 1042–6, Jan. 2001.

[13] M. Millard, S. Odde, and N. Neamati, “Integrin Targeted Therapeutics,” *Theranostics*, pp. 154–188, 2011.

[14] D. Mainali and E. a Smith, “Select cytoplasmic and membrane proteins increase the percentage of immobile integrins but do not affect the average diffusion coefficient of mobile integrins.,” *Anal. Bioanal. Chem.*, vol. 405, no. 26, pp. 8561–8, Oct. 2013.

[15] J. a Askari, C. J. Tynan, S. E. D. Webb, M. L. Martin-Fernandez, C. Ballestrem, and M. J. Humphries, “Focal adhesions are sites of integrin extension.,” *J. Cell Biol.*, vol. 188, no. 6, pp. 891–903, Mar. 2010.

[16] P. G. Saffman, “Brownian motion in thin sheets of viscous fluid.” 1975.

[17] K. J. Seu, L. R. Cambrea, R. M. Everly, and J. S. Hovis, “Influence of lipid chemistry on membrane fluidity: tail and headgroup interactions.,” *Biophys. J.*, vol. 91, no. 10, pp. 3727–35, Nov. 2006.

[18] Z. Chen, R. P. Rand, B. Sciences, S. Catharines, and O. Ls, “The Influence of Cholesterol Bending Elasticity Phospholipid Membrane Curvature and,” vol. 73, no. July, 1997.

[19] D. Dibya, N. Arora, and E. a Smith, “Noninvasive measurements of integrin microclustering under altered membrane cholesterol levels,” *Biophys. J.*, vol. 99, no. 3, pp. 853–61, Aug. 2010.

[20] R. O. Hynes, “Integrins: Bidirectional, allosteric signaling machines,” *Cell*, vol. 110, no. Table 1, pp. 673–687, 2002.

[21] D. R. Critchley, “Two-piconewton slip bond between fibronectin and the cytoskeleton depends on talin,” vol. 424, no. July, 2003.

[22] A. Fuhrmann, J. Li, S. Chien, and A. J. Engler, “Cation Type Specific Cell Remodeling Regulates Attachment Strength,” vol. 9, no. 7, 2014.

[23] I. D. Campbell and M. J. Humphries, “Integrin structure, activation, and interactions,” *Cold Spring Harb. Perspect. Biol.*, vol. 3, pp. 1–14, 2011.

[24] G. Binnig, “Atomic Force Microsdcope,” vol. 56, no. 9, 1986.

[25] R. H. Eibl and V. T. Moy, “Atomic Force Microscopy Measurements of Protein – Ligand Interactions on Living Cells,” vol. 305, no. 1.

[26] M. Rief, F. Oesterhelt, B. Heymann, and H. Gaub, “Single Molecule Force Spectroscopy on Polysaccharides by Atomic Force Microscopy,” *Science*, vol. 275, no. 5304, pp. 1295–7, Feb. 1997.

[27] Y. Seol and K. C. Neuman, “Single Molecule Analysis,” vol. 783, pp. 265–293, 2011.

[28] D. E. Fuentes, C. Bae, and P. J. Butler, “Focal Adhesion Induction at the Tip of a Functionalized Nanoelectrode.,” *Cell. Mol. Bioeng.*, vol. 4, no. 4, pp. 616–626, Dec. 2011.

[29] K. Dholakia, P. Reece, and M. Gu, “Optical micromanipulation,” *Chem. Soc. Rev.*, vol. 37, no. 1, pp. 42–55, Jan. 2008.

[30] F. Bordeleau, J. Bessard, N. Marceau, and Y. Sheng, “Measuring integrated cellular mechanical stress response at focal adhesions by optical tweezers.,” *J. Biomed. Opt.*, vol. 16, no. 9, p. 095005, Sep. 2011.

[31] C. G. Galbraith, K. M. Yamada, and M. P. Sheetz, “The relationship between force and focal complex development.,” *J. Cell Biol.*, vol. 159, no. 4, pp. 695–705, Nov. 2002.

[32] J. W. Shaevitz, “A Practical Guide to Optical Trapping,” *Unknown*, pp. 1–19, 2006.

[33] A. van der Horst and N. R. Forde, “Power spectral analysis for optical trap stiffness calibration from high-speed camera position detection with limited bandwidth.,” *Opt. Express*, vol. 18, no. 8, pp. 7670–7677, 2010.

[34] S. F. Tolić-Nørrelykke, E. Schäffer, J. Howard, F. S. Pavone, F. Jülicher, and H. Flyvbjerg, “Calibration of optical tweezers with positional detection in the back focal plane,” *Rev. Sci. Instrum.*, vol. 77, no. 10, p. 103101, 2006.

[35] H. Hogan, “Focusing on the Experiment,” *Biophotonics International*, pp. 48–51, 2006.

[36] J. H. Price and D. a Gough, “Comparison of phase-contrast and fluorescence digital autofocus for scanning microscopy.,” *Cytometry*, vol. 16, no. 4, pp. 283–97, Aug. 1994.

[37] R. M. Zucker, “Quality Assessment of Confocal Microscopy Slide-Based Systems : Instability,” vol. 690, no. June, pp. 677–690, 2006.

[38] D. C. Mason and D. K. Green, “Automatic Focusing of a Computer-Controlled Microscope,” *IEEE Trans. Biomed. Eng.*, vol. BME-22, no. 4, pp. 312–317, Jul. 1975.

[39] F. Shen, L. Hodgson, and K. Hahn, “Digital autofocus methods for automated microscopy.,” *Methods Enzymol.*, vol. 414, no. 06, pp. 620–32, Jan. 2006.

[40] I. Nikon, “Perfect Focus.”

[41] J. S. Silfies, E. G. Lieser, S. A. Schwartz, and M. W. Davidson, “Correcting Focus Drift in Live Cell Microscopy,” 2013. [Online]. Available: http://www.microscopyu.com/articles/livecellimaging/focusdrift.html.

[42] A. Micro, “Dynamic evaluation of autofocusing for automated microscopic analysis of blood smear and pap smear,” vol. 227, no. January, pp. 15–23, 2007.

[43] K. Spring, *Video microscopy: the fundamentals*. Springer, 1997.

[44] X. Wang, “Laplacian operator-based edge detectors,” *IEEE Trans. Pattern Anal. Mach. Intell.*, vol. 29, no. 5, pp. 886–890, 2007.

[45] F. C. a Groen, I. T. Young, and G. Ligthart, “A Comparison of Different Focus Functions for Use in Autofocus Algorithms,” vol. 91, 1985.

[46] J. G. Ziegler and N. B. Nichols, “Optimum Sttings for Automatic Controllers,” *Transacction of the A.S.M.E*, vol. 64, pp. 759–768, 1942.

[47] S. Bennett, “A brief history of automatic control,” *Control Syst. IEEE*, vol. 16, no. June 1996, pp. 17–25, 1996.

[48] a Ashkin, J. M. Dziedzic, J. E. Bjorkholm, and S. Chu, “Observation of a single-beam gradient force optical trap for dielectric particles.,” *Opt. Lett.*, vol. 11, no. 5, p. 288, 1986.

[49] P. J. Butler, “Penn State University Mechanobiology Laboratory,” 2007. [Online]. Available: http://www.bioe.psu.edu/mechlab/facilities.html. [Accessed: 02-Feb-2015].

[50] 3M, “Double-Sided Tapes,” 2010.

[51] NoahCorp, “Quadrant Photodetector Module.”

[52] M. K. Cheezum, W. F. Walker, and W. H. Guilford, “Quantitative comparison of algorithms for tracking single fluorescent particles.,” *Biophys. J.*, vol. 81, no. October, pp. 2378–2388, 2001.

[53] A. Le Gall, K. Perronet, D. Dulin, A. Villing, P. Bouyer, K. Visscher, and N. Westbrook, “Simultaneous calibration of optical tweezers spring constant and position detector response.,” *Opt. Express*, vol. 18, pp. 26469–26474, 2010.

[54] D. E. Fuentes, “Dynamics of Molecules and Membranes During the Early Stages of Focal Adhesion Formation,” 2012.

[55] F. Li, S. D. Redick, H. P. Erickson, and V. T. Moy, “Force measurements of the alpha5beta1 integrin-fibronectin interaction.,” *Biophys. J.*, vol. 84, no. 2 Pt 1, pp. 1252–1262, 2003.

[56] P. W. Wiseman, C. M. Brown, D. J. Webb, B. Hebert, N. L. Johnson, J. a Squier, M. H. Ellisman, and a F. Horwitz, “Spatial mapping of integrin interactions and dynamics during cell migration by image correlation microscopy.,” *J. Cell Sci.*, vol. 117, pp. 5521–5534, 2004.

[57] C. G. Galbraith, K. M. Yamada, and M. P. Sheetz, “The relationship between force and focal complex development.,” *J. Cell Biol.*, vol. 159, no. 4, pp. 695–705, Nov. 2002.

[58] E. Cretel, A. Pierres, A.-M. Benoliel, and P. Bongrand, “How Cells feel their environment: a focus on early dynamic events.,” *Cell. Mol. Bioeng.*, vol. 1, no. 1, pp. 5–14, Mar. 2008.

[59] P. Robert, A.-M. Benoliel, A. Pierres, and P. Bongrand, “What is the biological relevance of the specific bond properties revealed by single-molecule studies?,” *J. Mol. Recognit.*, vol. 19, no. August, pp. 299–304, 2007.

[60] L. Lamalice, F. Le Boeuf, and J. Huot, “Endothelial cell migration during angiogenesis,” *Circ. Res.*, vol. 100, pp. 782–794, 2007.

[61] M. J. Paszek, D. Boettiger, V. M. Weaver, and D. a. Hammer, “Integrin clustering is driven by mechanical resistance from the glycocalyx and the substrate,” *PLoS Comput. Biol.*, vol. 5, no. 12, 2009.